Field Evaluation of Hybrid-Composite Girder Bridges in Missouri

Prepared by
John J. Myers, Ph.D., PE (Project Principal Investigator)
Mohamed A. Aboelseoud
C. Renee Earley
Glenn Washer, Ph.D., PE (Project Co-Principal Investigator)
Justin Schmidt
Missouri University of Science and Technology, Rolla and University of Missouri-Columbia

Final Report Prepared for Missouri Department of Transportation
2014 August Project TRyy1124 Report cmr15-002

FINAL Report

TRyy1124

Field Evaluation of Hybrid-Composite Girder Bridges in Missouri

Prepared for
Missouri Department of Transportation
Organizational Results

By

Dr. John J. Myers (Project Principal Investigator)
Mohamed A. Aboelseoud
C. Renee Earley

Dr. Glenn Washer (Project Co-Principal Investigator)
Justin Schmidt

Missouri University of Science and Technology, Rolla, Missouri
University of Missouri - Columbia

June 2014

TECHNICAL REPORT DOCUMENTATION PAGE

1. Report No. cmr 15-002 2.	Government Accession No. 3.	Recipient's Catalog No.
4. Title and Subtitle Field Evaluation of Hybrid-Composite Girder Bridges in Missouri		5. Report Date June 30, 2014 6. Performing Organization Code
7. Author(s) Dr. John J. Myers, P.E., Mohamed A. Aboelseoud, C. Renee Earley, Dr. Glenn Washer, Justin Schmidt		8. Performing Organization Report No.
9. Performing Organization Name and Address Missouri Department of Transportation Research, Development and Technology P. O. Box 270-Jefferson City, MO 65102		10. Work Unit No. 11. Contract or Grant No. TRyy1124
12. Sponsoring Agency Name and Address Missouri Department of Transportation Research, Development and Technology P. O. Box 270-Jefferson City, MO 65102		13. Type of Report and Period Covered Final Report 14. Sponsoring Agency Code
15. Supplementary Notes The investigation was conducted in cooperation with the U. S. Department of Transportation, Federal Highway Administration.		

16. Abstract

Three hybrid composite beam (HCB) bridges were recently constructed in Missouri, USA. HCB is an innovative idea that incorporates traditional construction materials (steel and concrete) with fiber reinforced polymer (FRP) composites in such a manner to optimize the performance of the beam constituents. The HCB consists of self-consolidating concrete (SCC) poured in classical arch shape and tied at the ends by conventional prestressing strands. The concrete and steel are tucked inside durable fiberglass shell and the voids are filled with polyiso foam. An integrated study was implemented on the three bridges to investigate the HCB in-service behavior. The study included quality control / quality assurance (QC/QA) testing program. As a part of this research study, an innovative infrared (IR) thermal imaging approach was developed to detect the voids in the concrete arch section during its casting. The approach is found to be an ideal solution for QC/QA of the concrete arch concrete placement. A series of load tests on the bridges together with meticulous theoretical and numerical analyses were executed. The first finite element analysis (FEA) for a HCB bridge superstructure was accomplished. The analysis was used to provide better understanding for the girder behavior and to emphasize the areas that need more examination. Based on the FEA results the existing flexural design methodology and assumptions were tested. The methodology was found unable to detect the maximum compressive stress in the concrete arch, and the strain compatibility assumption was found invalid. However, the experimental measurements along with the mathematical calculations indicate that the HCB owns abundant nominal bending and shear strength to withstand the expected loads during its lifetime. A modified methodology that is based on the same assumptions as the existing one was produced. The methodology was found to achieve significant enhancement in predicting the stresses under the service loads. The durability of the HCB was tested through subjecting the composite shell to different aging regimes. The testing results indicate that the HCB possesses excellent durability in relation to the expected weathering exposure in Missouri. Longer exposure regimes are under implementation to assure these results.

17. Key Words Bridge Load testing, Composite materials, Durability behavior, Finite element modeling, Hybrid-structures, Material characterization, NDT/NDE.	18. Distribution Statement No restrictions. This document is available to the public through National Technical Information Center, Springfield, Virginia 22161

19. Security Classification (of this report) Unclassified	20. Security Classification (of this page) Unclassified	21. No. of Pages 153	22. Price

Form DOT F 1700.7 (06/98)

EXECUTIVE SUMMARY

In this study entitled, ***Field Evaluation of Hybrid-Composite Girder Bridges in Missouri,*** a new type of the HCBs was recently used to construct three bridges (B0439, B0410, and B0478) in MO, USA. The HCB consists of a self-consolidating concrete (SCC) arch that is tied at the ends using high-strength galvanized steel strands. The concrete and steel, which represent the compression and tension reinforcement respectively, are encased inside a durable fiberglass composite shell. Due to this unique configuration, the fiberglass box protects the steel and concrete from the environmental effects and serves as the formwork for the concrete arch, while the strength and stiffness are provided by an efficient use of the steel in purely axial tension, and the concrete in purely axial compression. In addition to the optimization of load carrying behavior offered by this configuration, it results in a lightweight member that can be transported easily and erected rapidly making this technology well suited to Accelerated Bridge Construction (ABC).

Because of the novelty of the HCB and its vague structural behavior, an exploratory program to the Missouri University of Science and Technology (MS&T) in cooperation with University of Missouri-Columbia (UMC) was undertaken to evaluate the in-service beam behavior. The program consisted of four main phases which includes Phase 1: Quality control/Quality assurance Testing; Phase 2: Finite Element Modeling of HCB bridge superstructure; Phase 3: Investigation of the HCB's Flexural Behavior; and Phase 4: Assessment of HCB Durability Performance.

The results of the experimental investigations accompanied by the mathematical analyses for the HCB bridges led to the following conclusions:

- Without proper concrete rheology, the concrete arch is susceptible to the formation of voids during concrete placement. The proposed Infrared thermal imaging technique presented herein is an ideal solution for detecting such voids and for QC/QA of the arch concrete placement. It can also be applied as a QC/QA tool to assess the workmanship of the composite construction.
- HCB owns abundant nominal bending and shear strength to withstand the expected loads during its lifetime.
- The unique configuration of the HCB optimizes the load carrying behavior and maintains the gross section properties under the service loads.
- The FEMs of B0439 suggest that the single-web HCB may suffer lateral and rotational deformations under vertical loads, indicating that the single-web girder may have weak lateral and torsional rigidity.
- The shell webs are the most critical elements in shell. Attentiveness needs to be paid to their elastic buckling and shear stresses during the design process.
- The polyisocyanurate foam and the cross-ties contribute to the lateral stability of the FRP webs. However, the shell webs of B0410 HCBs suffered outward deformation during the arch pour. This indicates that the cross-ties might be overstressed similar to what was observed by (Snape & Lindyberg, 2009).
- The linear FEA is accurate in predicting the static behavior of HCB under the service loads.
- The existing flexural design methodology overestimates the stresses in the FRP shell and strands, and is unable to predict the maximum compressive stress in the concrete arch.
- The polyiso foam works as flexible shear connection and achieves partial composite action between the different elements of the HCB resulting in differential displacement between them. Consequently, the different components at the same level have different strains.
- The results of this work suggest that the HCB does not yield perfect beam behavior. The tied arch and the relative movements between its elements affect its behavior.
- The proposed flexural methodology presented in this study achieve significant enhancement in estimating the normal strains in the HCB elements under the service loads. The methodology suggests that it may be acceptable to assume strain compatibility between the girder elements during the design process.
- The durability testing results clarify that the GFRP shell, and subsequently the HCB as a whole, has excellent durability in relation to the expected weathering exposures in Missouri. Longer exposure regimes are under implementation to assure these results.

ABSTRACT

The hybrid composite beam (HCB) is an innovative idea that incorporates traditional construction materials (steel and concrete) with fiber reinforced polymer (FRP) composites to optimize the beam performance. Each HCB consists of self-consolidating concrete (SCC) poured in a classical arch shape and tied at the ends by conventional prestressing strands. The concrete and steel are tucked inside a durable fiberglass shell, and the voids are filled with polyiso foam. An integrated study was implemented on three bridges in Missouri to better understand an HCB's in-service behavior. The study included quality control / quality assurance (QC/QA) testing program. As a part of this research study, an innovative infrared (IR) thermal imaging approach was developed to detect possible voids in the concrete arch section during its casting. The approach is found to be an ideal solution for QC/QA of the concrete arch concrete placement. A series of load tests on the bridges, together with meticulous theoretical and numerical analyses, were executed. The first finite element analysis (FEA) conducted on an HCB bridge superstructure was accomplished. The analysis was used to provide a better understanding of the girder's behavior. It was also used to identify those areas needing further examination. The FEA results were used to test the existing flexural design methodology and its assumptions. The methodology was unable to detect the maximum compressive stress in the concrete arch, and the strain compatibility assumption was invalid. However, the experimental measurements, along with the mathematical calculations, indicated that the HCB contains abundant nominal bending and shear strength to withstand the loads expected during its lifetime. A modified methodology that is based on the same assumptions as the existing one was produced. This methodology significantly improved the ability to predict the stresses experienced under service loads. The HCB's durability was tested when the composite shell was subjected to different aging regimes. These results indicated that the HCB possessed excellent durability in relation to the

expected weathering exposure in Missouri. Longer exposure regimes are currently being examined to verify these results.

ACKNOWLEDGMENTS

The authors would like to acknowledge the Missouri Department of Transportation (MoDOT) and the National University Transportation Center (NUTC) at Missouri S&T for sponsoring this research study. The staff support from the Dept. of Civil, Architectural & Environmental Engineering, and Center for Infrastructure Engineering Studies (CIES) at Missouri S&T are also greatly appreciated.

TABLE OF CONTENTS

Page

LIST OF ILLUSTRATIONS

LIST OF TABLES

1. INTRODUCTION

1.1. BACKGROUND

The transportation infrastructure in the United States can be considered the backbone of America due to its effect on nation's economy as well as citizens' lifestyle. Bridges are considered to be a vital part of the infrastructure system. However, the number of deficient bridges continues to increase. According to the National Bridge Inventory (2012), 11% of America's bridges (67000 out of 607000 bridges) are deficient. That means these bridges are not unsafe, but must be closely monitored and inspected or repaired. The spans in these bridges are vital to motorists, who take 210 million trips daily across them. The need for innovative construction materials that can significantly prolong a bridge's lifetime has led to the development and use of fiber reinforced polymer (FRP) composites in bridge applications. These composites possess extraordinary properties (e.g. high strength-to-weight ratio, corrosion resistance, dimensional stability, excellent durability, transparency to electromagnetic radiation, and low to moderate tooling costs) making them ideal alternatives for resolving a number of problems, particularly corrosion and deterioration problems. However, fully composite FRP structural members fail to be cost competitive when compared to traditional concrete and steel members in civil engineering applications. The increased initial cost can be traced directly to the FRP composites' raw material costs and low stiffness. The most effective use of the FRP (as main load carrying members) is in the form of hybrid systems that use both FRP and traditional construction materials (Mirmiran, 2001).

Hillman introduced a new hybrid composite beam (HCB) in 1996 that was used for the first time commercially in 2008 (Earley et al., 2013). The HCB is comprised of three main sub-components: a composite shell, compression reinforcement, and tension reinforcement. The shell is comprised of a glass fiber reinforced polymer (GFRP) box beam. The compression reinforcement consists of self-consolidating concrete (SCC) that is poured in a classical arch shape. The tension reinforcement consists of galvanized high strength (HS) steel tendons anchored at each end within the end blocks. The concrete and steel are tucked inside the durable fiberglass shell, and the voids are filled with a polyisocyanurate (polyiso) foam.

This new HCB can be constructed rapidly and possesses increased durability. Three recently constructed bridges in Missouri incorporated HCBs in conjunction with traditional reinforced concrete deck systems. HCB is, however, quite novel. Thus, its structural behavior

needs comprehensive experimental investigation, along with thorough, theoretical and numerical analyses.

1.2. RESEARCH OBJECTIVES

This research was conducted by a research team at Missouri University of Science and Technology (MS&T), in cooperation with a research team from the University of Missouri-Columbia (UMC). The research consisted of following four phases:

Phase 1: Quality control/quality assurance testing (UMC - MS&T)

The goals of this phase consisted of the following:

a. Conduct an analysis of the potential damage modes that could affect the HCB (UMC).
b. Develop and apply non-destructive evaluation (NDE) technique to evaluate the quality of the SCC arch and any and maintenance challenges (UMC).
c. Use standard quality control assurance testing (i.e. compressive strength of concrete, tensile strength of the composite shell, cure temperature monitoring, etc.) and so forth to characterize the construction materials chosen (MS&T).
d. Evaluate the mature and early-age behavior of the SCC via monitoring its cure temperature in the wake of the cast (MS&T).

Phase 2: The finite element modeling of an HCB bridge superstructure (MS&T)

The finite element modeling of an HCB bridge superstructure was conducted in an attempt to achieve the following goals:

a. Examine the accuracy of finite element analysis for predicting the static behavior of HCBs under service loads.
b. Evaluate the accuracy of the existing design methodology in estimating deflection along HCBs under static load cases.
c. Establish a methodology for applying computer modeling to HCBs.
d. Provide a better understanding of HCBs' structural behavior.
e. Highlight areas that need further research and investigation.

Phase 3: An investigation of HCB's flexural behavior (MS&T)

This phase was conducted to achieve the following goals:

a. Analyze the flexural behavior of in-service HCBs under service loads.
b. Evaluate the existing design methodology and assumptions.
c. Propose a modified flexural design methodology that can predict the stresses in the different HCB elements with acceptable accuracy.

Phase 4: An assessment of HCB's Durability Performance (MS&T)

The durability of the HCB was tested by subjecting specimens taken from HCB shell to the following aging regimes:

a. Salt fog exposure regime for 3072 hours (128 days).
b. Sustained stress, along with 350 different thermal cycles in a computer-controlled environmental chamber (75 days).
c. UV-irradiation exposure for 3072 hr. followed by 6000 hr. of salt fog exposure (378 days). (*under long-term implementation outside the scope of this report*)
d. Sustained stress along with: indoor ambient controlled weathering, and outdoor natural weathering (225 days). (*under long-term implementation outside the scope of this report*)

2. LITERATURE REVIEW

2.1. LOAD TESTING

The bridge load testing was performed by measuring the static deflection induced by a loaded tandem axle dump truck placed in locations to induce maximum moment and shear reactions. There are two different types of load testing, diagnostic, and proof testing. Diagnostic load testing examines the response of the structure. The results can be compared to future load tests and theoretical models to evaluate the elasticity of the structure, the load distribution, and the accuracy of design assumptions. Proof testing results are used in determining a safe loading capacity by loading the structure within the elastic range (Merkle, 2004).

2.2. AASHTO LOAD FACTORS

To accommodate the large number of highway bridges required, the AASHTO Bridge Specifications allow for a beam-line analysis in the transverse direction of a bridge so long as the structure meets a set of parameters. This analysis uses AASHTO specified live load distribution factors based on bridge materials and geometry. If these parameters are not met, a more in-depth analysis of the structure is required (AASHTO-LRFD, 2012).

2.3. FIBER REINFORCED POLYMER COMPOSITES

Over the last decade, there has been significant growth in the use of fiber-reinforced polymer (FRP) composite materials as construction materials in structural engineering (Bank, 2006). FRP composites have apparent advantages over the traditional construction materials such as concrete and steel. Their high strength-to-weight ratio, corrosion resistance, dimensional stability, excellent durability, high dielectric strength, and low to moderate tooling costs make them promising and valuable materials for use in new construction and for upgrading existing infrastructures.

Although FRP composites are ideal alternatives materials for resolving a number of problems that face highway bridges, especially corrosion and deterioration problems, their initial cost is relatively expensive in comparison to the classical materials used in civil engineering applications. This is greatly due to current design approaches that use them in common linear shapes, such as I-sections and rods, which do not take advantage of the inherent in-plane stiffness and strength of laminated composites (Keller, 2002). One way to reduce initial costs is to combine FRP with conventional construction materials in structural

members. The advantages of the hybrid structural systems include the cost-effectiveness and the ability to optimize the structure based on constituent material properties.

The hybrid FRP-concrete design concept has been applied to flexural members by several researchers. The concept of using concrete with the common glass fiber-reinforced polymer (GFRP) composite sections, such as shown in Figure 2-1, emerged to overcome some shortcomings of using these sections independently as flexural members. These shortcomings include:

1. The compressive flange is considerably weaker than the tensile flange. This is attributed to the local buckling phenomena and to low compressive strength of GFRP relative to its tensile strength.
2. The catastrophic failure nature of GFRP sections, due to the fact that GFRP is linear elastic up to failure
3. The low stiffness of GFRP sections, results in the use of obviously larger sections to satisfy the design codes serviceability requirements.

To solve the aforementioned problems, researchers have replaced the upper GFRP flange with a layer of concrete, utilizing the high compressive concrete strength in resisting the compression zone stresses. Moreover, the high stiffness of the concrete contributes to the overall stiffness of the member. Some researchers also added a thin layer of externally bonded carbon-fiber reinforced polymer (CFRP) to the section's tension zone, because CFRP ultimate strain is less than that of GFRP. Consequently, the CFRP layer will be the first element to fail, giving some warning of an imminent collapse. The high stiffness, excellent creep behavior, and excellent fatigue resistance of CFRP also increase the rigidity of the member and enhance its resistance to sustained and fatigue stresses. Finally, to minimize the fabrication cost, part of the cross section is used as formwork for the wet concrete. An illustration of a hybrid FRP-concrete cross section is shown in Figure 2-2.

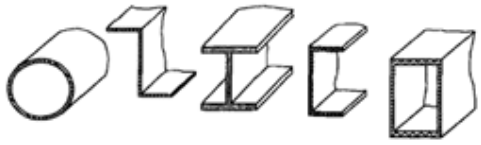

Figure 2-1 Typical Pultruded Composite Cross Sections

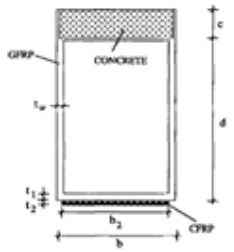

Figure 2-2 Hybrid FRP-Concrete Cross Section

Deskovic et al. (1995) investigated a hybrid FRP-concrete beam that consisted of filament-wound GFRP box section combined with a layer of concrete and a CFRP laminate in the compression and tension zone respectively. They concluded that their proposed design concept results in cost-effective hybrid members that possess many desirable mechanical behavior characteristics, such as pseudo-ductility and high strength and stiffness, while maintaining a low weight. Van Erp et al. (2002) proposed a hybrid FRP-concrete beam similar to the design proposed by Deskovic et al. Their beam consisted of GFRP box section, a layer of concrete, which was bonded on the GFRP box section by a high quality epoxy adhesive, and a fiber reinforcement that was added to the tensile flange of the box section. The weight of the hybrid beam was claimed to be about one-third of that of a reinforced concrete beam. Aref. et al. (2005) applied the concept of the hybrid FRP-concrete structural system to a bridge superstructure. The one-lane superstructure was formed by bonding Three trapezoidal glass fiber reinforced polymer (GFRP) box sections, then a layer of concrete was poured in the compression zone of those sections. A further review on the hybrid structures can be found in the paper by Mirmiran (2001).

The current work studies a new type of HCBs recently used to construct three bridges in Missouri. The underlying concept of the HCB was conceived by Hillman in 1996, and the first commercial use was in June 2008. The advantages, composition, fabrication, and installation of the HCB are discussed in the following sections.

2.4. SELF-CONSOLIDATING CONCRETE

Self-consolidating concrete**,** (SCC) is a new category of high-performance concrete**,** which can flow easily into tight and constricted spaces with minimum or no vibration needed to remove trapped air or allowing coarse aggregate to separate from the cement paste. Due to the improved homogeneity of this highly flowable concrete, it develops the required bond

with the reinforcing bars, achieves adequate structural performance and proper durability (Khayat, 1999). The SCC mix design utilizes a high-range water reducing (HRWR) admixture, to achieve the increased flow compared to normal **concrete.** The HRWR is a polycarbonate super-plasticizer chemical admixture. The addition of the HRWR to the concrete mix aims to increases the flow and workability of the concrete without increasing the water/cement (W/C) ratio. The advancements in HRWR's over the last several years have allowed for SCC to be produced and maintain the flow and stability needed to achieve the benefits of SCC.

The main use of the SCC is in the concrete elements, that are heavily reinforced with steel or have configurations that complicate the placement and consolidation of normal concrete. Recently, SCC has been used in precast and prestressed concrete elements due to its ability to reach all areas of the formed element and eliminate personnel typically needed to provide consolidation efforts, and because of the restricted reinforced areas. Moreover, the early strength gain achieved by SCC allows the reuse of the formwork in a timely manner, which is desirable for the precast elements. The use of SCC in high volume concrete elements also increases the pump and placement rate and eliminates consolidation time. Increasing concrete pump ability also can make concrete placement by pump for high rise concrete buildings a possibility that was not available just a few years ago. The emergence of the SCC can make the concrete more economical option compared to steel during the construction of high-rise building. This is incarnated by the use of SCC in the construction of the current world's tallest building (Burj Dubai) in Dubai, United Arab Nations.

On the other hand, the most concerns about SCC are primarily the aggregate segregation and the ability to produce concrete in a consistent manner. Minor changes in aggregate degradations, aggregate moisture control, or material specific gravities may result in aggregate segregation. Consequently, close attention needs to be given during mix design and production of the SCC.

2.5. OVERVIEW OF HYBRID-COMPOSITE BEAM

2.5.1. Background

The hybrid composite beam (HCB) consists of self-consolidating concrete (SCC) that is poured in classical arch shape and anchored at ends by high strength conventional prestressing tendons. Both the SCC and the high strength tendons are tucked inside durable, fiberglass composite shell. The unique configuration of the HCB aims to subject the concrete to pure compressive stresses and the steel to pure tensile stresses and exploit the durability of

the GFRP to produce a structural member that can last more than one hundred years. The orientation of these sub-components is further evident as demonstrated graphically by Figure 2-3.

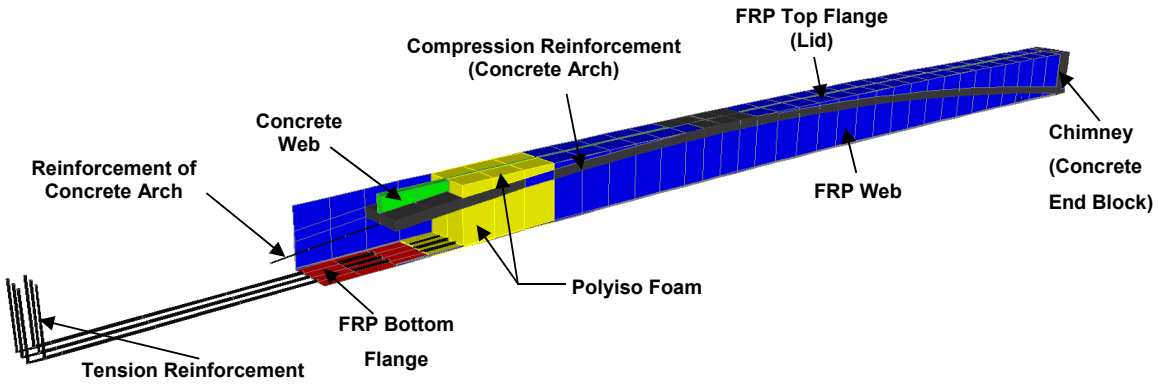

Figure 2-3 Fragmentary Perspective of Hybrid-Composite Beam

In addition to the optimization of load carrying behavior offered by HCB, it has further advantages that allow this new technology to be a better alternative to prestressed and steel beams in many bridge applications. The potentially long service life and low maintenance requirements of the HCB may reduce the frequency and duration of roadway and lane closure, minimizing the impact to traffic and thus reducing the potential for work zone accidents. An equivalent HCB uses only 10% of the concrete of a prestressed concrete beam. Since amount of greenhouse gases released during the production of concrete and the fabrication of steel is significant, there is a noticeable difference in the gases produced. For most typical applications, the weight of the HCB during transportation and erection is approximately one fifth of the weight of a conventional steel beam and one tenth of the weight of a precast prestressed concrete beam required for the same span. In most cases, the beams can be safely set with 30-50 ton cranes instead of 150-300 ton cranes. In addition, 4 to 8 HCBs can be placed on a single truck as opposed to a single beam for a precast concrete box beam. The lightweight combined with the corrosion resistant nature of the FRP materials make this technology well suited to Accelerated Bridge Construction (ABC) and result in bridges with service lives that could exceed one hundred years.

2.5.2. HCB Composition

The different elements of the HCB and their functions are briefly discussed in the following sections:

Compression Reinforcement: The compression reinforcement consists of concrete poured into classical arch shape. As indicated by the name, the selection of the arch shape aims to subject the concrete to pure compressive stresses under the service loads, hence optimizing the usage of the concrete. The concrete arch ends with two concrete shafts (chimneys). The main function of the chimney is to transfer the horizontal forces from the HCB to the cast-in-place (CIP) diaphragms. Another function of the chimney is to enable the tension reinforcement to tie the arch without the need for an anchorage device. Due to the constricted and inaccessible cavity provided for the compression reinforcement, the use of highly flowable concrete is substantial. Subsequently, self-consolidating concrete (SCC) was used to form the HCB arches of the three constructed bridges.

Tension Reinforcement: The function of the tension reinforcement is to tie the concrete arch and contribute to the flexural stiffness of the HCB. The tension and compression reinforcing are the primary load carrying elements of the HCB. They also provide the greatest contribution to the beam stiffness. During the design process, the amount of the tension reinforcement is increased until the deflection limit is satisfied. Therefore, the material selected for this component must have very high tensile strength and very high modulus of elasticity. Based on these requirements, the conventional prestressing tendon seems to be the most convenient element to serve as tensile reinforcement of the HCB. In the current project, prestressing strands (Grade 270) were used to tie the HCBs arches.

FRP Shell: The main goal of the FRP shell is to protect the HCB elements from the environmental effects, hence increasing the beam lifetime. It also serves as a formwork during the concrete arch pour and contributes to the girder stiffness and nominal capacity. The standard laminate composition of the HCB shell is typically a quadweave glass reinforcing fabric infused with a vinylester resin matrix. Generally the quad-weave or "triaxial weave" fabrics that used in HCB comprised of multiple layers of glass rovings with varying percentages of the fibers oriented in the 0º, 90º and +/-45º directions relative to the longitudinal axis. This type of fabrics with multidirectional fibers enhances the efficiency of a composite subjected to shear strains as well as longitudinal and transverse strains. Another benefit of the multidirectional weaves is that with the proper orientation of fibers, the composite begins to behave somewhat "quasi-isotropic" which can simplify preliminary designs.

HCB Core: The core material fills the voided space within the beam shell. Polyisocyanurate (polyiso) foam was selected to serve as the core material due its lightweight, low cost, available sizes and its tremendous low thermal conductivity. The core plays two important roles during the fabrication and the service life of the HCB. First, the core serves as interior form that helps the beam to maintain its shape during the fabrication process. Without the core, the other beam elements would implode under the vacuum process. Second, it provides lateral stability to the FRP webs, hence increasing their buckling strength.

Concrete Web: The concrete web can be considered as a part of the compression reinforcement. Its main function is to transfer the loads from the lid to the concrete arch and subsequently to the tension reinforcement. It also supports the shell top flange (FRP lid) and prevents it from local buckling.

Shear Connectors: The shear connectors are intended to transfer the load from the bridge deck to the arch achieving a full composite action between the HCB and deck slab. The connectors also increase the shear capacity of the arch.

2.5.3. Fabrication and Construction Sequencing

The first step in the HCB manufacture is the fabrication of the FRP box and steel strands. The bottom shell of the beam (FRP bottom flange and webs), complete with tension reinforcing are fabricated in one mold. The top flange is fabricated in a separate mold. The shell is fabricated using the Vacuum Assisted Resin Transfer Molding (VARTM) process. VARTM is an adaptation of the resin transfer molding (RTM) process and it is very cost-effective in making large structures (Mazumdar, 2001). Although the fabrication and construction sequencing of HCB are not unique and deviate slightly from project to another, the main steps of the fabrication of the HCBs can be summarized as follow:

A three-sided box is fabricated to the dimensions of the beam. Along the centerlines of the flange, slots are made to install channels. These channels act as a line source for the resin infusion and vacuum. The layup of the shell consists of placing one layer of a surface veil over the entire mold surface, followed by one layer of a distribution media, and finally the glass fiber layers. In addition to the UV inhibitors contained in the resin, the surface veil and distribution media provide extra protection for the fiber layers against the UV degradation. The two layers also ease the resin transfer and provide a resin rich layer on the outer surface of the shell.

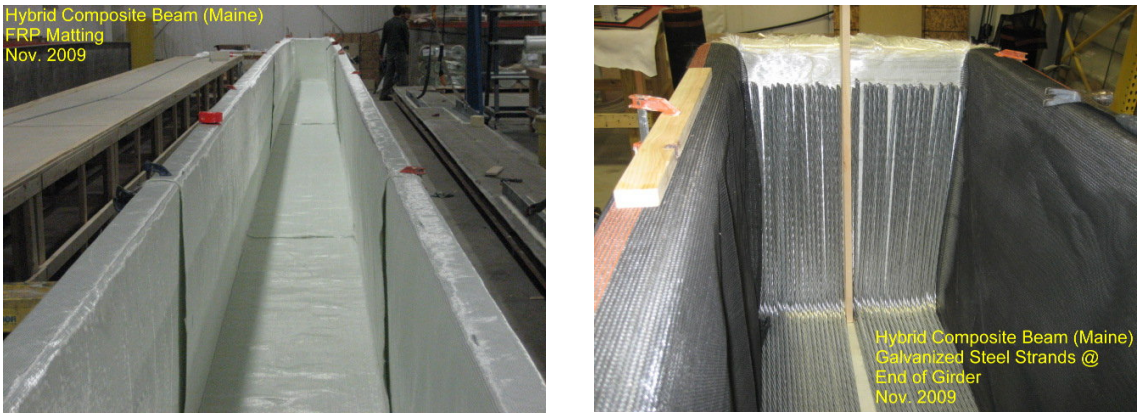

(a) (b)

Figure 2-4 Fabrication of HCB by Harbor Technology Inc., Maine
(a) Layup of the GFRP shell (b) Placement and positioning of the strands

Seven-wire high strength tendons are then placed on the top of the bottom flange fiber layers with ends running up vertically to anchor the compression reinforcement. Once the post-tensioning bars are positioned, polyisocyanurate foam blocks are placed within the mold forming arch shape. A bag is placed on the foam blocks and inflated to keep a cavity for the compression reinforcement. Spacers and clamps are used to tie the shell webs and ensure the dimensions of the cavity. Upper layer of foam blocks is placed on the top of the bag while still leaving a cavity to accommodate the concrete web.

The entire mold is completely enclosed in layers of vacuum bagging film sealed with tacky tape. Vacuum is then applied through the vacuum ports. After evacuating all of the air, the vinylester resin is pulled into the form by the vacuum pressure and the mold is kept under vacuum. The FRP lid (top flange) is fabricated in a separate mold with the same procedure. Before attaching the top flange to the bottom shell, seven-wire strands (generally two strands) are installed in the bottom of the arch and run the full length of the beam. Tie wires are attached to the strands to lift them up during installation of the shear connectors.

Figure 2-5 Cut and Preparation of the foam blocks (left image)
Placement of the air bag and Spacers (right image)

The FRP lid is glued to the bottom shell using methyl methacrylate adhesives (MMA). The MMA adhesives provide strong bond that ensure that the lid acts compositely with the bottom shell during the arch pour and the erection of the HCB. Self-tapping stainless steel screws are used to further connect the two elements. The screws are important to arrest any crack that might propagate through the adhesive bond.

Finally, holes are drilled into the lid and the bottom legs of the shear connectors are then developed below the loose strands.

2.5.4. Installation Sequence

Once fabricated, the HCB shells are shipped and erected on the supports. SCC is then pumped into a profiled conduit within the shell through preset slots in the top flange. The slots are drilled into the lid at the midspan, quarter points, and above the chimneys. Pouring the concrete arch may be executed prior to erection or even before shipment of the beams as occurred in B0410. Casting the arch after installation of the beams facilitates significantly the shipment process and allows using small cranes for beams placement. On the other hand, pouring the arch before beams shipment allows the concrete arch to gain strength while other construction activities take place, hence reducing the construction time, and yet the weight of the full HCB is about one third to one fourth the similar prestressed girders. It should be noted that once the beams are filled with concrete, they must be lifted from the ends. This can be achieved by placing strand lifting loops in the chimneys prior to casting the arch. These

loops are then removed once the HCB units installed on the substructure. Figure 2-6 illustrates the placement of B0439 HCBs.

Figure 2-6 Erection Process of B0439 HCB

Once cured, the concrete arch acts compositely with the complete shell and the concrete of the deck, by then the parapets can be placed. There are many different ways to place a concrete deck on top of a HCB framed bridge. The deck slab is typically filled in-place; however, it may also be precast prior to erection. Though casting the concrete arch and deck slab prior to erection reduces the lightweight advantage of this technology, this technique allows constructing a bridge superstructure in one day, resulting in substantial congestion relief.

2.5.5. Existing Hybrid-Composite Beam Projects

A limited number of studies have been conducted on HCB. There are two existing HCB bridges outside the state of Missouri, which were preceded by laboratory test programs to investigate and analyze the HCB behavior. These bridges are the Knickerbocker Bridge in Maine and the Tide Mill Bridge in Virginia.

The Knickerbocker Bridge in Maine was constructed in 2010. Testing was performed prior to the construction of Knickerbocker Bridge at the Advanced Engineering Wood Composite (AEWC) lab at the Advanced Structures and Composites Center at the University of Maine. The test program included static and fatigue tests performed on full-scale HCB compositely connected to a cast-in-place deck. The program also tested the durability of the

FRP shell through macroscopic-level tests performed on FRP control specimens and specimens that were subjected to UV irradiation exposure regime.

The HCB tested in AEWC lab had a height of 33" with one layer of (42-1/2") diameter seven wire strands. The beam was connected, via shear connectors, to concrete deck that was 7" deep and 48" wide. The top lid of the Knickerbocker HCB was infused in segments and spliced together. A typical cross-section of the tested beam is illustrated by Figure 2-7 (Snape & Lindyberg, 2009).

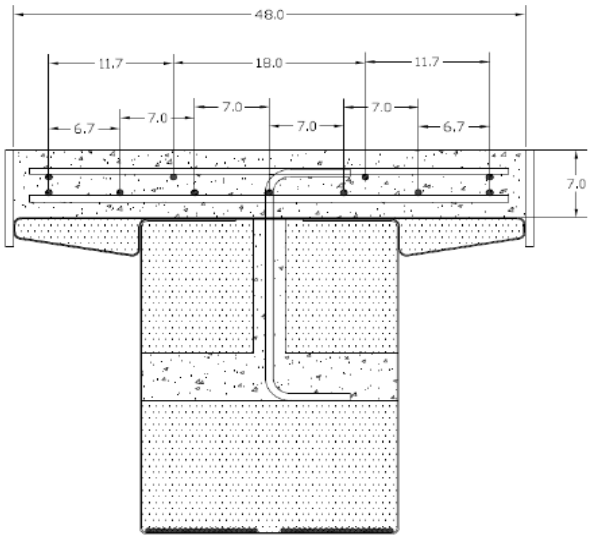

Figure 2-7 Typical cross-section of the HCB tested in AEWC lab (Snape & Lindyberg, 2009)

The measurements of the initial deflections under the fluid load of the arch concrete and the fluid load of the deck concrete were in general agreement with the design calculations. However, immediately prior to static testing, the beam had a negative camber of approximately 1 3/8" at mid-span, which was a result of the camber equations not considering the self-weight of the beam shell and shrinkage of the arch concrete and the deck concrete after placement resulting in additional deflections (Snape & Lindyberg, 2009).

Initial static shear and bending tests demonstrated that the HCB is linear-elastic under the design loading conditions. These tests also demonstrated that Hillman's model predicts the beam behavior under service loads accurately. Following 2,000,000 fatigue bending cycles, no deterioration or degradation was observed in the beam when loaded to its bending service load capacity (Snape & Lindyberg, 2009).

The FRP lid was flat transversely which made the lid susceptible to buckling. The composite wings were found to provide stiffness and stability to the tested beam during the

cast of the arch. The splicing technique used to transfer load across the joint in the top plate and wings was largely ineffective, buckling under load until the joint closed in compression. The composite cross-ties (spacers) were found to prevent the local buckling of shell webs under the fluid concrete load, although some ties were excessively stressed (Snape & Lindyberg, 2009).

All the mechanical properties of the composite shell, but the in-plane shear modulus were found to increase following the weathering regime exposure. These results suggested that the UV inhibitors that were included in the resin resisted effectively the UV irradiation effect. The increase in the mechanical properties was attributed to residual cross-linking of the polymeric structure (Snape & Lindyberg, 2009).

The Tide Mill Bridge test program was executed by Virginia Tech University. The program consisted of three phases of testing to determine the individual HCB behavior and a skewed three-HCB system behavior. The first phase of testing was conducted on HCBs before pouring the concrete arch (FRP shell and prestressing tendons only). In this phase, distributed and concentrated loads (at midspan and quarter points) were applied by placing steel angles manually at the top of the FRP lid. The second phase tests were performed on non-composite HCBs (complete HCBs including the compression reinforcement, before the deck pour). In this phase, a hydraulic static actuator was used to apply concentrated loads at midspan and quarter points of HCBs. The last phase tested a full-scale laboratory HCB bridge. The bridge consisted of three HCBs incorporated with traditional skewed reinforced concrete deck. In this phase different load cases that simulated tire loading of a HL-93 truck were performed (Ahsan, 2012).

The HCB elements were shown to behave linear-elastically during service level tests. Predicted deflections and strains in the HCB elements were often conservative compared to measured results. The neutral axis locations observed from testing were in general agreement with the predicted location. Strain profiles constructed using the strain measurements for each component, during the three phases, showed that the arch concrete has no strain compatibility with the other elements. The behavior of the arch was inconsistent with the overall HCB behavior. Though, some strain profiles showed strain compatibility between the strands and the bottom flange, other strain profiles suggested that there is no perfect bond between the two elements. Overall, Comparisons between the experimental measurements theoretical calculations, illustrated that Hillman's model predicted the strains of the strand and FRP shell with acceptable accuracy. While, the model provided a poor prediction for the concrete arch strains (Ahsan, 2012, Nosdall, 2013).

During the first and second load testing, close-range photogrammetry was used to detect out-of-plane movement of the FRP web and movement of the arch within the FRP shell due to the applied loads. During the two phases, significant lateral displacement at the midspan of the HCB was measured suggesting that beam is flexible laterally and prone to lateral displacement, especially when not connected to a bridge system. During the second phase, significant movement of the arch within the FRP shell was also detected indicating that there was no perfect bond between the two components (Mascaro & Moen, 2012).

3. HCB BRIDGES DESCRIPTION

3.1. GENERAL

Three bridges were recently constructed in Dade, Douglas, and Reynolds Counties, Missouri, USA. The bridges incorporated single-web and double-web HCBs with conventional cast-in-place (CIP) concrete decks. A brief description for the bridges details and their construction sequences are presented in the following sections. Moreover, a description of the process used to cast the concrete arch is included herein to document, generally, the process used for these experimental beams. This data is documented in anticipation of additional applications of the technology in the future, to record the process utilized in this initial application of the technology.

3.2. BRIDGE B0439

3.2.1. Design Details

The first HCB bridge (B0439) is located on MO 76 over Beaver Creek in Douglas County. Its construction was completed in November 2011, and the bridge was opened to traffic shortly thereafter. This three-span bridge is approximately 180 ft-0-in. long, and its overall width is 30 ft-8-in. The B0439 Bridge consists of five simply supported HCBs in each span for a total of fifteen HCBs. Each of these HCBs is (33-in. x 24.38-in.) and consists of SCC arch that is 5-in. deep and 22-in. wide. The concrete arch is reinforced with (2-1/2-in.) galvanized steel strands Grade (270 ksi) and is tied via (36-1/2-in.) strands of the same type arranged in one layer. The concrete arch is connected to the upper GFRP flange with SCC web with varying width ranging from 3-in. to 4-in. The concrete arch is also reinforced with #5 galvanized shear connectors. The shear connectors are located every 8-in. at a 45º angle. Typical cross-sections of B0439 and its HCB are illustrated in Figure 3-1 and Figure 3-2 respectively.

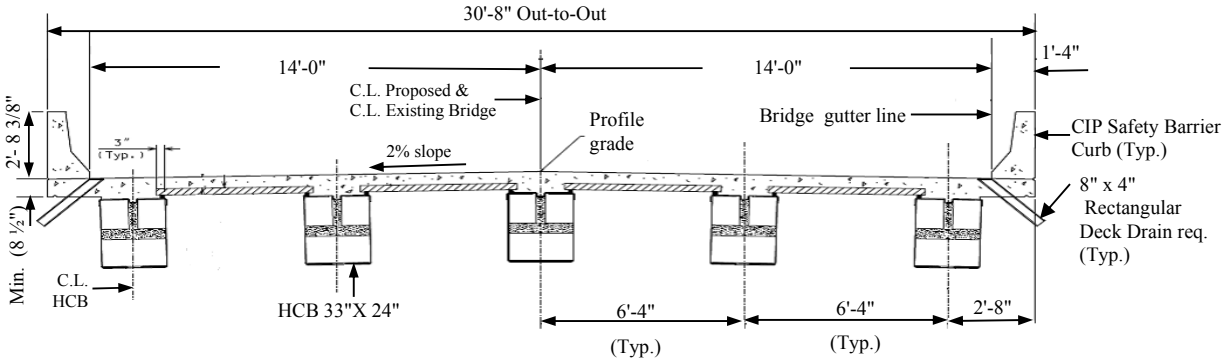

Figure 3-1 Bridge B0439 Typical Cross Section

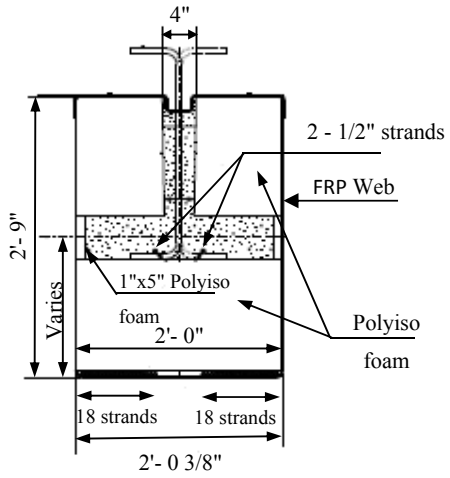

Figure 3-2 Typical Cross Section of B0439 HCB

3.2.2. B0439 Construction

The complete shells of the HCBs (FRP shells including the prestressing strands) were fabricated in Harbor Technologies inc., Maine, USA. The fifteen HCBs were then shipped to Missouri using only two trucks rather than fifteen trucks needed for similar prestressed girders. The HCB arches were poured off-site near the local ready-mix plant, Peterson Ready Mix, in Mountain Grove, MO. During the week of the pours, only one concrete truck was used to deliver the SCC to the pour site. Due to this, it took an average of 45 minutes from the end of one beam pour to the beginning of the next. Once the concrete mix for the SCC was deemed acceptable on site, the SCC was then poured into the HCBs' arches. During the week, the beams were placed together in pairs at the pour site, with enough space left in between the pairs to park a truck. Instead of using a pump truck, the SCC was poured into the beams directly from the concrete truck. For the pour, a funnel was used to aid in the pour from the truck into the HCBs' concrete arch. During the majority of the pours, workers had to throw out chunks of concrete that had begun to consolidate in the truck.

For the actual procedure, the concrete would first be poured into one end hole until the end block was filled. The workers would then switch to the other end to fill in the opposite end block. The same procedure was used for the quarter holes, filling one then switching to the other, until finally concrete was poured into the center pour hole. This procedure would allow the concrete to keep pushing itself down until the arch was completely filled. This would become apparent on site due to concrete pushing up through the pour holes as well as through the shear connectors. To aid in the consolidation and flow of concrete through the arch, workers on site tried to use vibration on the concrete. To do this, workers would 'vibrate' the shear connectors sticking out of the top of the HCB, since these

went down into the concrete arch. Workers would either hit the connectors with a hammer or shake them back and forth with their hands.

Figure 3-3 Installation of B0439 HCBs on the piers

The HCBs were then installed on the bridge piers (Figure 3-3). To expedite the superstructure construction, precast stay-in-place deck forms were used to span between the beams, which spaced at 6 ft-4-in. to accommodate the 30 ft-8-in. out-to-out dimension of the deck. As a result, the only deck forming required was for overhangs at the fascia girders, which was done using standard overhang brackets and walkways as illustrated in Figure 3-4.

Figure 3-4 Construction of B0439 Superstructure

Figure 3-5 Pour of B0439 Deck

3.3. BRIDGE B0410

3.3.1. Design Details

The second bridge (B0410) is located on MO 97 over Sons Creek in Dade County. B0410 spans 104 ft-0-in. from center-of-bearing to center-of-bearing and its out-to-out dimension of the deck is 30 ft-8-in. B0410 beams are the longest span HCBs yet constructed. Since the lengths of the HCBs are relatively long (105 ft-7-in.), the beams were fabricated as multi-celled (double-web) beams. This was intended to significantly reduce the time of fabrication and erection. The multi-celled HCBs require a slight increase in lay-up time; however, the infusion time is the same due to additional infusion ports for each cell of the beam. The entire process can still be performed in one day. The reduction in erection time was due to the contractor only handling three girders instead of six. A typical cross section of B0410 is shown in Figure 3-6.

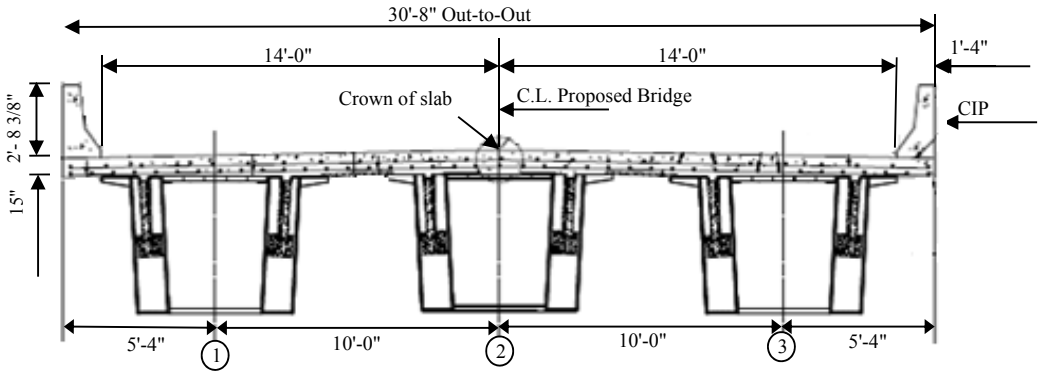

Figure 3-6 Typical Cross-Section of Bridge 0410

Each multi-celled HCB has an overall depth of 5 ft-0-in. and varying width ranging from 5'-6-in. at the bottom to 6 ft-0-in. at the top. Each single HCB consists of SCC arch, which is 10-in. deep and 10.5-in. wide. The concrete arch is reinforced with (2-1/2-in.); 270 ksi seven-wire galvanized steel strands and is tied via (44-1/2-in.); 270 ksi seven-wire strands arranged in two layers. The system is encapsulated in GFRP shell with 5 ft-0-in. depth and 13.75-in. width. The concrete arch is connected to the upper GFRP flange with SCC web of varying width ranging from 3-in. to 5-in. The concrete arch is reinforced also with #5 galvanized shear connectors. The shear connectors are spaced every 9-in. at a 45º angle. The voided spaces between the arch and the FRP shell are filled with polyisocyanurate foam. A typical cross section of B0410 HCB is illustrated in Figure 3-7.

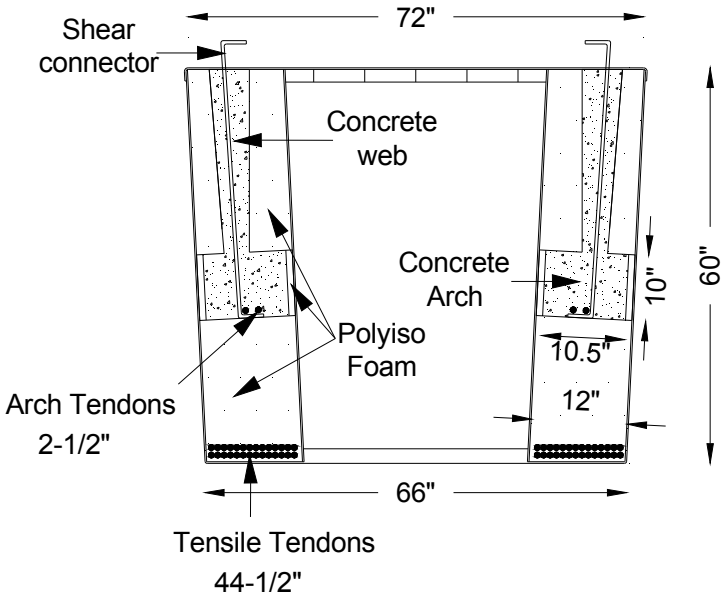

Figure 3-7 Typical Cross Section of B0410 HCB

3.3.2. B0410 Construction

After the manufacture of the complete shells in Maine, the pouring of the concrete arches took place at Coastal Precast Systems in Chesapeake, Virginia. The pour procedure for these double web HCBs generally followed the same concept as that of the first bridge. However, there were some minor differences. For this bridge, the concrete was poured into the arches using a pump truck that was placed off to one side of the beams. Different

consolidating techniques were also used for the SCC in this bridge. A concrete vibrator was used to aid in concrete consolidation instead of vibrating the shear connectors. The vibrators were placed into the pour holes, along the top crevice where the shear connectors come out of the beam, and through some shear connector openings. Figure 3-8 shows the placement of the SCC from a pump truck through the drilled slots in the FRP lid.

Figure 3-8 Placement of SCC, B0410 in Chesapeake, Virginia

In addition, since it was a double-web beam, concrete could not be filled in one arch, or web, without counterbalancing it in the other. So the pour would start at one end block, and once filled, the workers would move to the opposite end block on the other web and fill that end block. This simple procedure was to prevent the HCB from tipping over due to the weight of the concrete. The remaining end blocks were then filled. From there, the workers followed the same procedure, going from one-quarter hole to the opposite web and opposite end quarter hole. When finished with the four-quarter holes, the workers finished the pour with the two middle pour holes.

The pour for the bridge B0410 covered two weeks. One double-web HCB was poured during the first week, while the remaining two were poured the second week. The weather in Virginia prevented all three double web beams to be poured at the same time, with rain in the forecast the last few days of the first week.

During the pour of the first double web beam, it became apparent to workers and on-site quality control (QC) personnel that something had gone wrong with the concrete pour into the arch. Workers realized that the concrete was not rising as it should to the top of the arches inside the two webs. QC personnel then ran a simple test by sticking a ruler down through the shear connectors and pour holes to see if there were any voids in the concrete. A void map was then constructed from the information gathered and is shown in Figure 9. Voids were present in both arches and both ends of the beam. Additional concrete was poured into the arches through the shear connectors and additional pour holes drilled into the beam to fill the voids approximately 1 week after the original casting process. The voids were determined to be due to decreased flow ability in the concrete at the time of the pour.

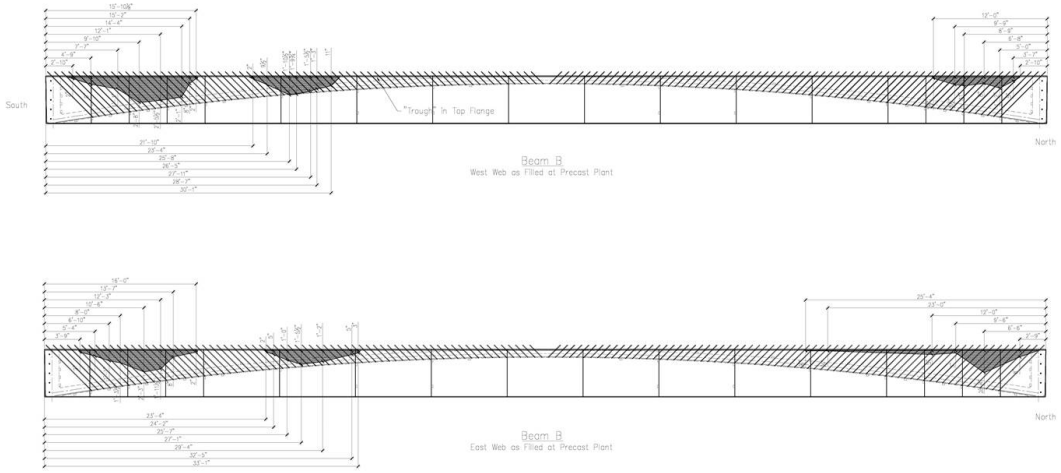

Figure 3-9 Diagrams of Voids in SCC Arch of B0410

After completion of the arches pour, the girders were shipped directly to the site and placed on the abutments. Instead of using precast planks as in B0439, this bridge incorporated the use of FRP sandwich panels spanned between the beams to eliminate the need for deck forming and speed up the construction process. It is worth mentioning that by the end of the concrete arch pouring the deflection of the HCB due to its self-weight was found about half the expected deflection. This forced increasing the depth of the B0410 deck slab to approximately 15" to eliminate the excessive camber.

Figure 3-10 Erection of B0410 Double-Web HCBs

3.4. BRIDGE B0478

3.4.1. Design Details

The third bridge (B0478) is located on MO 49 over Ottery Creek Overflow in Reynolds County. B0478 is two-span Bridge with overall length 98 ft 8-in. from center-of-bearing to center-of-bearing and its out-to-out dimension of the deck is 26 ft-8-in. The bridge consists of twelve HCBs, six simply supported HCBs in each span. The configuration of HCBs used in this project is similar to those used in B0439 with slight changes in the dimensions and tension reinforcements. A typical cross section of B0478 is shown in Figure 3-11, while Figure 3-12 illustrates the composition of each HCB.

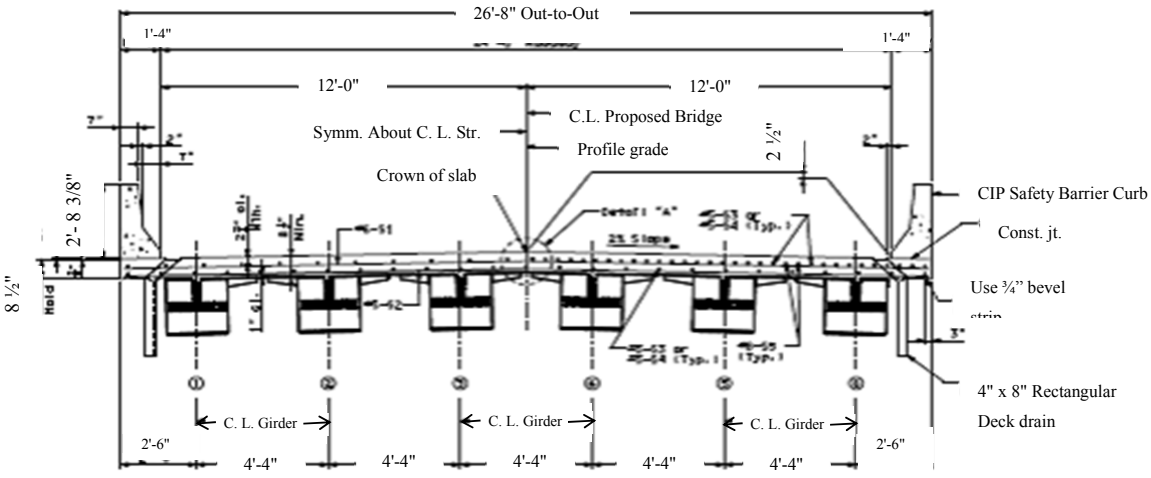

Figure 3-11 Typical Cross Section of Bridge B0478

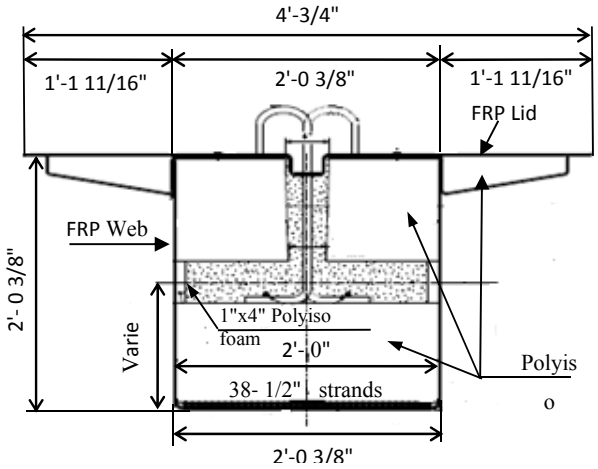

Figure 3-12 Typical Cross Section of B0478 HCB

3.4.2. B0478 Construction

Unlike the first two bridges, the placement of the concrete arches was performed after the erection of the girders on the bents. Therefore, a pump truck was required to pour the concrete into the arches since the bridge was already erected, as shown in Figure 3-13. However, since the HCBs were single web beams, the pour procedure generally followed that of the first bridge, B0439. Multiple concrete trucks were used to transport the SCC out to the bridge site in order to keep the concrete pumping continuously. It should be noted that when pouring began on the first day, it was a goal that all 12 beams were to be poured in the same day. However, delays were experienced because of difficulty with the quality of the SCC; as a result, the pouring procedure was extended into the second day.

Figure 3-13 B0478 In-Situ Concrete Pour

In order to meet the Accelerated Bridge Construction "ABC" initiatives, this bridge used a six-beam cross section with composite overhanging flanges. Subsequently, the HCB units are placed at 4 ft-4-in. centers rather than the 6 ft-4-in. spacing on the B0439. This configuration resulted in six girder lines instead of five, eliminating the need for precast planks or FRP panels for deck construction. As a result, the only deck forming required was for overhangs at the fascia girders, similar to the previous two bridges. This type of HCB cross-section and ABC technique was also employed on the eight-span Knickerbocker Bridge in Boothbay, Maine in 2011, which was introduced in the literature.

Other details of these HCB bridges, such as bearing pads, and bridge railings and parapets are not different from those used on conventional concrete box beam bridges. The different installation sequences used in the three bridges reflect the flexibility that is offered for the bridge owners to optimize the transportation and erection processes or construction time. It should be noted, that the HCB including the concrete arch is still significantly lighter than the similar prestressed beam required to support the same span length. This not only eases the transportation and the erection of the beam but also enables the utilization of the existing substructures for rapid replacement of deteriorated superstructures.

3.5. BRIDGE B0410 INSTRUMENTATION

Among the three bridges, only elements of HCB2 in B0410 have been instrumented with various strain gauges and thermocouples. The instrumentation aimed to:

- Evaluate the stress and strain levels in the HCB elements during the different loading stages.
- Monitor the thermal changes during the concrete arch pour, and evaluate their effects on the other elements.
- Examine the existing flexural design methodology along with analyzing the flexural behavior of the HCB under service loads.
- Analyze the thermal behavior of the HCB bridge superstructure.
- Monitor the short-term and long-term behavior of the HCB.

To achieve the previous goals, four electrical resistance strain gauges were adhered to tension strands. A concrete arch and its web were instrumented using nine vibrating wire strain gauges (VWSGs) / thermistors (seven gauges to measure normal strains and two gauges to measure shear strains). Twelve electrical resistance strain gauges were adhesively bonded to the FRP shell (seven sensors to measure normal strains and five to measure shear

strains). Twelve thermocouples were placed at various locations. All but the FRP shell sensors were placed during the shell fabrication at Harbor Technologies, Maine, USA. The FRP strain gauges were placed on the shell by MS&T researchers prior to the concrete pour at the precast plant in Virginia, USA. Following fabrication, data collection indicated that two strand strain gauges and two VWSGs within the concrete arch were not functioning properly. While uncertain, these sensors could have been damaged due to the exposure to very high temperature during the infusion process of the resin or during the transportation and erection processes. Figure 3-14 and Figure 3-15 illustrate the locations of the sensors within the girder. The strain gauges/ thermistors placed in the concrete are denoted by VWSG/T, the FRP gauges are denoted by FRP, the strand gauges are denoted by SSG, while the thermocouples are denoted by TC.

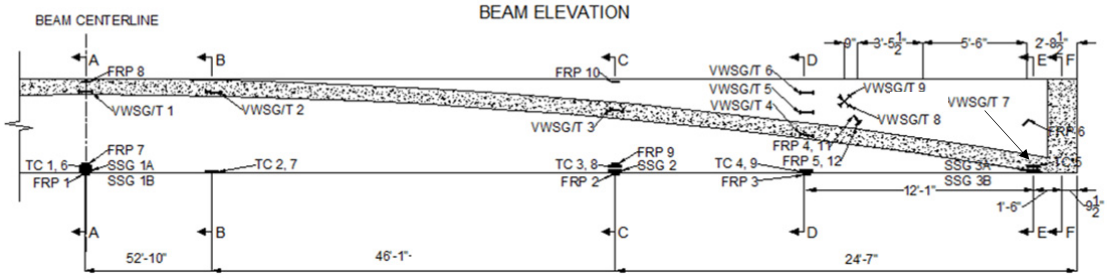

Figure 3-14 Instrumentation of HCB2, B0410 (Elevation View)

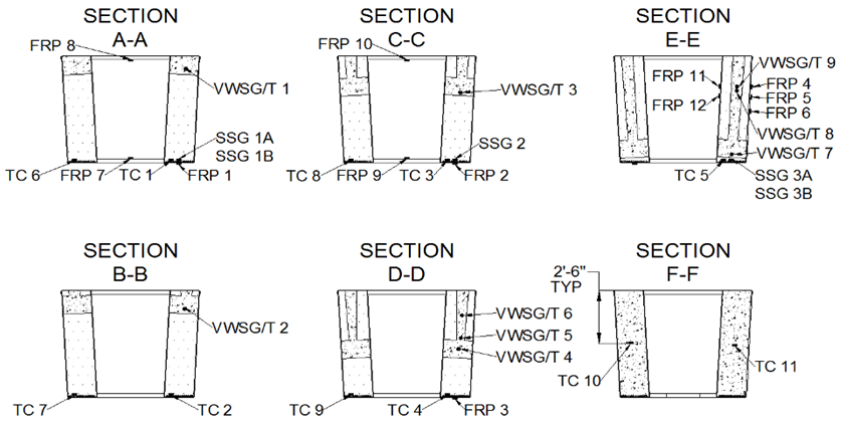

Figure 3-15 Instrumentation of HCB2, B0410 (Cross-Sections)

Figure 3-16 through Figure 3-18 show the installation of the FRP gauges before the arch pour. Figure 3-16 shows the application of the M-Bond adhesive to the strain gauge on the bottom of the shell. Figure 3-17 illustrates the system for maintaining constant pressure on the gauge to allow for proper bonding. Figure 3-18 demonstrates the completed strain gauge covering to protect the gauge and its wires from the water and weathering effects.

Figure 3-16 FRP Strain Gauge Placement, M-Bond Adhesive

Figure 3-17 FRP Gauge Placement, Constant Pressure for Drying with Added Heat

Figure 3-18 FRP Strain Gauge Placement, Final Protection of Gauges and Wiring

Figure 3-19 illustrates the entry and collection of the wires in the interior of the HCB (between the two webs). Figure 3-20 shows recording the sensors data by connecting the wires to compact RIO and laptop.

Figure 3-19 Entry of Data Cables into Interior of HCB

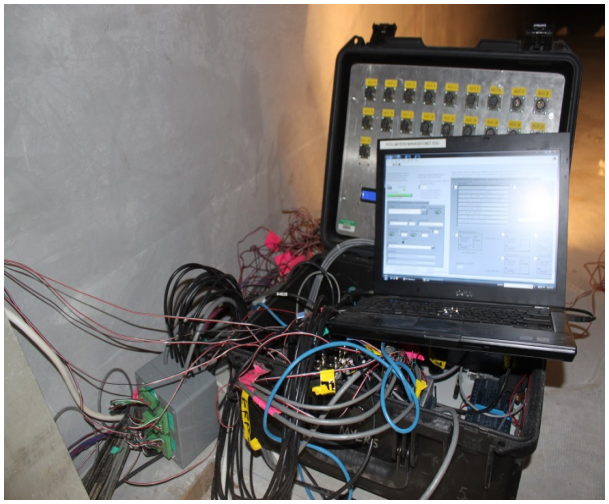

Figure 3-20 Data Collection Unit in Interior of HCB

4. QUALITY QONTROL / QUALITY ASSURANCE (QC/QA) TESTING PROGRAM

4.1. GENERAL

This chapter provides an evaluation and analysis of potential inspection challenges and suitable nondestructive evaluation (NDE) techniques to assess the experimental HCB. NDE methodologies assessed include ultrasonic testing, acoustic emission, thermography, magnetic flux leakage and tap testing. Given that HCB technology is new to the state of Missouri, and has very limited service experience elsewhere, an evaluation of potential challenges and technologies for inspecting these bridges was needed. The objectives of this chapter were as follows:

- Develop and apply methods for quality control / quality assurance testing.
- Evaluate potential serviceability and maintenance challenges.

To achieve these objectives, an analysis of the potential damage modes that could affect these bridges was conducted. These include flaws or defects that may occur during the fabrication of the HCB members, as well as in-service damage modes that may occur during the service life of the bridge. Damage modes were identified and are described herein. A survey of available inspection technologies was also conducted to identify tools that could be used to assist in quality control (QC) and quality assurance (QA) testing. The NDE tools identified were focused on QC/QA testing of the concrete arch, which may be placed in a fabrication yard or in the field at the bridge site. Tools suitable for in-service inspection of HCBs are also discussed.

The QC/QA regime of the HCBs was accomplished by executing different tests before, during, and after the construction of the beams. The testing program included fabrication of a mock-up beam before the construction of B0439 HCBs. The mock beam simulated one of the bridge HCBs and was utilized to simulate pouring the concrete through the congested arch cavity. During the arch pour of B0439 HCBs, the cure temperature of one of the end block (chimney) was monitored using thermocouples to assure the mature of the concrete. The early-age behavior of HCB2 of the second bridge (B0410) was monitored by recording the thermal changes of the concrete arch during the first 24 hours after the pour. The strains in the different elements were recorded and analyzed during the same period. Compressive strength tests were performed on standard concrete cylinders taken from the arches of the three bridges. Tensile coupon tests were applied to control specimens of the FRP shell of B0439 through durability test program. The control specimens, not only were

used to evaluate the environmental effects on the composite shell, but also were utilized to assure the tensile properties of the laminated shell that were provided by the manufacturer. QC/QA testing of the arch using thermography was also conducted for each of the members constructed during the project for three HCB bridges. During the course of the research, thousands of images of the HCB members were capture using infrared cameras. A small subset of these images is included herein, to explain the technology and describe the most significant results found in the research. Tap testing of the composite shell was also completed for one of the three HCB bridges constructed.

4.2. POTENTIAL DAMAGE MODES FOR HCB

To properly assess the suitable inspection technologies that could be applied for HCB, it was first necessary to consider the potential damage modes and deterioration mechanisms that could affect these members. The assessment of this information is focused on two time periods: during the fabrication of members, at which time NDE could have a role as a QC/QA tool, and through the service life of the bridge, when NDE could play a role in maintaining the safety and serviceability of a bridge. The damage modes considered were focused on those that are most likely to occur during the fabrication and service life of the bridge.

Figure 4-1 shows a schematic diagram of a HCB to illustrate the anticipated damage modes. These include cracking of in the composite shell surrounding the core, delamination in the composite shell, voids in the concrete, and corrosion damage in the prestressing strands that form the tie of the internal arch in the HCB members. Each of these damage modes is discussed in this section.

4.2.1. Voids in Concrete

Concrete is poured into the arch of the HCBs and acts as the compression chord for the member. SCC is used for casting this arch member. The arch forms an important compression member for the HCB, and as such, voids or other discontinuities in the arch concrete may lead to reduced load capacity, increased deflections and long-term serviceability issues. As a result, it is important that this material be continuous and without significant voids resulting from improper placement of concrete.

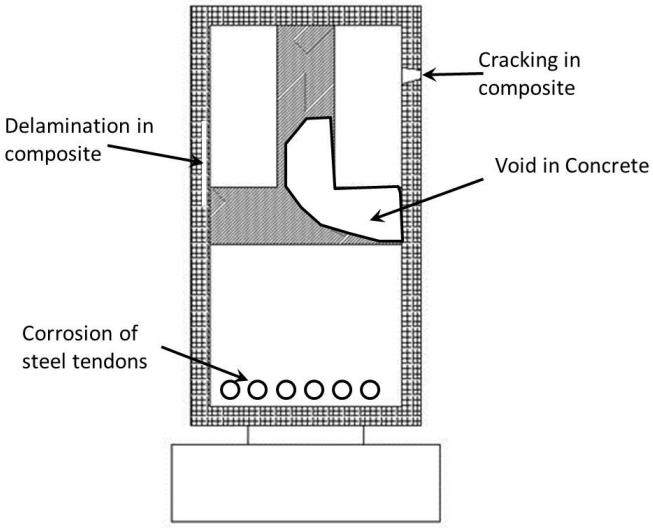

Figure 4-1 Example of Potential Damage Modes for HCB

Such voids, if they existed, are expected to be present following the concrete pour, and as such can be assessed during the construction phase and repaired if necessary. The internal concrete arch is contained within the FRP shell of the member, and approximately 1 in. of foam used to fill the HCB member and form the shape for the internal arch, into which SCC in placed. Given the geometry of the section, voids are hidden from view by the composite shell and foam inserts, and as such, these voids are not detectable through visual inspection at the time of construction.

4.2.2. Damage Modes for Shell Laminate

There are two primary potential damage modes for the composite shell of the HCB, cracking of the shell and delamination between the layers of the shell. The potential damage mode of cracking, or breaking of the fibers, in the HCB shell may result from loading or overloading of the beam, the effects of fatigue loading, or buckling of the compressive flange, separation of the flange and web, or local flange or web buckling due to overloading (Hayes, 2003, Karbhari, 2003). Generally, such a damage mode would progress to being surface-breaking and therefore can be observed through normal visual inspection.

The effect of ultraviolet radiation on the shell of the hybrid composite beam can increase the likelihood of cracking during the service life of the structure. Usually this initiates as visual cosmetic damage in the surface resin of the shell that does not affect the

structural properties of the FRP shell. This cosmetic damage includes surface color changes, loss of pigment, and loss of the surface luster of the laminate. Even though these damages are only visual cosmetic degradations in the surface resin, they can induce more significant damage in the shell (Karbhari, 2001, John R. Hillman, 2012). These degradations can eventually decrease the ultimate strain in the resin as well as decrease the specific toughness of the resin's surface layer. These decreases in the surface resin properties can cause the modulus of elasticity of the surface to increase and lead to crack propagation in the HCB shell.

Ultraviolet radiation damage to the shell of the HCB can be prevented through different additives in the resin formulas, or an application of a gel coat to the surface of the beam's shell. This gel coat is a thick resin layer on the exterior surface of the laminate, which can be applied through spraying or rolling after the manufacturing of the beam. The gel coat also improves fire protection of the beam and provides an additional barrier against moisture (John R. Hillman, 2012). Ultraviolet radiation damage is most likely to affect the fascia members of a bridge structure, particularly those facing the southern sky where solar exposure is anticipated. Generally, ultraviolet radiation damage to the composite can be observed visually and affects the outermost layers of the fibers. Given that the composite shell only has a moderate role in the primary load paths in the structure, such damage is unlikely to be a significant safety concern over the service life of a HCB structure.

Delamination between the layers of the composite shell is also a potential damage mode. Delamination is likely to occur due to improper application of resin during the fabrication of the composite shell. Voids in the resin material or resin-starved areas may develop delamination (Washer, 2013). Delamination has occurred in the lab testing of the HCBs; however, only during load testing that exceeds the factored demands (John R. Hillman, 2012). The results of these tests usually are the debonding of the web laminate from the interior polyiso foam core. However, since the loading exceeds factored demands, delamination has not been observed in the field.

Delamination can be detected using tap-testing methods or using infrared thermography (IR), as described later in this chapter. This damage mode is typically present at the time of fabrication, and as such can be appropriately addressed during QC testing. Localized delamination of the shell has only a modest effect on the tensile load-carrying capacity of the composite material, because shear transfer can be provided through the surrounding, well-bonded composite materials. As a result, delamination in the composite

surrounding the HCB core is primarily a workmanship issue that can be addressed through the QC process.

Secondary potential damage modes were stated in the HCB Design and Maintenance Manual for B0439 and are listed below with a short description of each (John R. Hillman, 2012):

- Blistering: Identified as bumps in the surface, usually caused by a porous surface resulting from a poor gel coat application.
- Presence of Moisture: The laminates applied to the HCB shell are subject to moisture absorption. This can lead to degradation of the composite material.
- Abrasion or Tearing: This type of damage may occur due to high water that results in debris impacting the composite or vehicles impacts below the bridge, which could result in section loss.
- Creep, Flow, or Rupture: These damage modes are of little concern due to the stiffness of the concrete and steel reinforcement, which creates low stresses and loads on the FRP laminates.

These secondary damage modes to the composite shell are generally available for assessment through visual inspection.

4.2.3. STEEL CORROSION

Corrosion of the steel prestressing strands that form the tie in the HCB may be a long-term maintenance concern. Given that, these strands are enclosed within the beam section, and hence unavailable for visual inspection, this damage mode will not be observable during normal, routine inspections. Steel will corrode when oxygen and moisture are present in the environment. The steel strands used to form the tie of the girder are galvanized to provide a sacrificial material that will act as the anode in electrochemical corrosion process.

As such, corrosion damage to the strands forming the tie is a long-term maintenance issue, since the galvanizing will provide adequate corrosion protection in the near term. Collection of moisture in the bottom of the HCB section, where the steel is located, could create a corrosive environment for the steel that corrodes the sacrificial zinc and leads to section loss.

Pitting corrosion in the steel strands is possible, in which localized areas of section loss develop such that overall section loss may be nominal, but deep pits reduce the tensile strength of the strand and result in strand fracture. Such localized corrosion damage may

occur when the galvanizing is damage during placement. An additional concern is for galvanized strands, given that the tie chord is formed from high-strength prestressing strand. Such high-strength steel is susceptible to hydrogen-assisted cracking; high levels of hydrogen may be produced in the corrosion process for the zinc coating the strand, leading to microcracking of the prestressing strand and subsequent reduction in load-carrying capacity. Presently, there are no viable, commercially available and practical technologies for identifying strand fracture, with the possible exception of radiographic testing (RT). Field applications of RT are relatively rare for highway bridges due to the perceived health and safety concerns, and the practical constraints of testing in the field. However, magnetic technologies developed for the detection of section loss and strand fracture in prestressed beams offer a potential technology for this application, and this technology will be discussed later in this chapter.

4.3. NON-DESTRUCTIVE EVALUATION TECHNIQUES

This section describes NDE technologies that may have application for QC/QA or in-service inspections of the HCBs. A survey of available NDE technologies was conducted, focused on the assumed damage modes previously described. Those technologies most likely to provide suitable tools for the assessment of HCBs were down-selected for inclusion in this report. These include ultrasonic testing, infrared thermography (IR), acoustic emissions, magnetic flux leakage, and tap testing.

4.3.1. Ultrasonic Testing

Ultrasonic testing has been in use as a nondestructive testing method for many years. Typically, ultrasonic tests are used to calculate the thickness of a material or detect and evaluate the size of flaws and defects, such as corrosion, voids, and cracks. This NDE method utilizes sound wave propagation to conduct these measurements. During this project, ultrasonic pulse velocity measurement were considered as a potential NDE technology that could be applied to the concrete arch for the detection of voids, honeycombs or poor quality concrete.

Ultrasonic testing uses high frequency sound energy to propagate waves, normally ranging from 50 kHz to 50 MHz in frequency, through a material to conduct the testing. An ultrasonic testing system is typically comprised of two primary elements, a pulser/receiver, and one or more transducers. The pulser produces a high voltage electrical pulse, which acts on the transducer. The ultrasonic energy then moves through the material in short bursts of

energy, interacting with the composition of the material. If there is a defect in the material, or if the wave reaches the opposite side of the material, the wave is then reflected back to the receiver. The reflected wave portion is then transformed into an electrical signal to be displayed on the system's screen for data analysis.

Generally, smaller defects require shorter wavelengths to be detected, and as such higher frequencies are typically used, around 2-4 MHz. Larger defects typically require lower frequency, and longer wavelengths, around .5 to 2 MHz, to be detected. Due to these frequency requirements, higher frequencies (shorter wavelengths) are used to test finer grained materials, such as metals, while lower frequencies (longer wavelengths) are used to test coarse grained materials, such as concrete. Increasing wavelength generally increases the penetrating power of the wave. The rule of thumb for flaw detection using ultrasonic is that the wavelength cannot be larger than twice the size of the defect. Generally, frequencies of approximately 50 KHz are used for testing concrete; 2.25 MHz is typically used for metals.

The primary limitation for ultrasonic testing is that a coupling medium is needed to transmit ultrasonic energy from the transducer into the materials under test. As a result, direct access to the surface is required, and the surface must be adequately prepared such that coupling can be achieved. Additionally, because the ultrasonic energy is reflected at boundaries of the materials, layered materials present a particular challenge. The reflection coefficient, i.e. amount of energy reflected at a the boundary of the materials, can be determined from the relative acoustic impedances of the material involved; when acoustic impedance differences are high, the reflection coefficient is also high. As a result, very little ultrasonic energy is transmitted across the boundary.

A conceptual diagram of the setup for ultrasonic pulse velocity for a hybrid composite beam is shown in Figure 4-2. As shown in the diagram, the internal foam lies between the composite materials on the surface of the member and the concrete core of the beams. As a result, ultrasonic waves cannot be transmitted directly into the arch concrete. Therefore, this approach was considered ineffective for assessing the quality of the concrete core.

Ultrasonic testing can also be used to assess delamination in the composite material, through the use of surface waves propagating in the composite layer. Such technology has been previously demonstrated for use in aerospace vehicles and pressure vessels. However, such an approach is costly, time consuming and requires hands-on access to the entire surface of the composite material to be assess. Infrared thermography, described later in this chapter, is capable of detecting these delamination without the requisite surface access necessary to

implement ultrasonic technology. Consequently, this technology was not pursued during the course of the research.

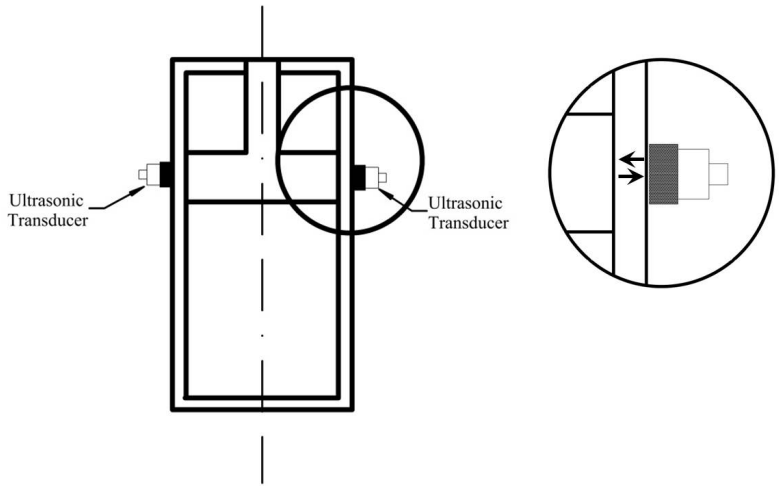

Figure 4-2 Testing Setup for Ultrasonic Pulse Velocity for HCB

4.3.2. Acoustic Emission

Acoustic Emission (AE) is a method of detecting the onset of damage in materials based on burst of elastic energy associated with the formation of the damage. The technique was first developed in the 1950's by materials scientist exploring the formation of the microstructures in metals, and later developed as a means of monitoring the development and propagation of the damage due to static and fatigue loading (Scott, 1991). Since that time, AE testing has become common for testing pressure vessels, aerospace vehicles and other engineering applications. More recently, AE methods have been developed exploring the application of AE as and NDE method for concrete and concrete structures and composite materials.

The fundamental theory behind the generation of acoustic emissions in materials is that propagation (growth) of a crack releases a small burst of elastic energy caused by the extension of the crack surface on an atomic level, and plastic-zone development processes surrounding the crack tip. This burst of elastic energy propagates as an acoustic pulse through the material and can be detected by sensors coupled to the surface of the material under test. For composite materials, cracking of the resin matrix and fracture of individual fibers produce acoustic emissions that can be monitored as a means of evaluating damage induced during loading cycles.

The acoustic emissions are typically discriminated from other noise that may be present, such as traffic noise on a bridge, rubbing of bearings, etc., based on waveform

characteristics (Nair & Cai, 2010). Analysis of monitoring results typically consists of assessing the number of AE events per unit time, with increased AE activity being associated with crack nucleation and growth.

Acoustic emission has traditionally been implemented for bridges as a monitoring technology, with a number of sensors placed permanently on a structure to monitor an area for incipient crack growth (Hutton, 1978, Vannoy, 1987, Clemena, 1995). Monitoring the acoustic emission activity of known cracks or the effects of retrofitting on arresting crack development and growth are the most typical applications, as opposed to monitoring a bridge with no known cracks (Prine, 1997, Kosnik, 2010). Applications of AE for bridges including composite materials has been very limited, although this technology is often used for composite-overwrapped pressure vessels during load testing (ElBatanouny et al., 2014). Monitoring systems for AE testing typically consists of multichannel (16 channels+) systems that can be mounted in the field and communicate data through phone lines.

The primary advantages of AE testing are the ability to monitor a large volume continuously, and to discriminate "active" damage, e.g. crack growth under load. Location of a defect can be assessed using multiple sensors on the material through cluster analysis and triangulation calculations. One of the main disadvantages of acoustic emission is directly related to its main advantage. Acoustic emission can only detect flaws that are actively growing. Therefore, if a defect is not active, AE testing would not detect it.

AE is a feasible technology for long-term monitoring of the composite shell for HCBs. The presence of the foam core material in the member, positioned between the concrete arch and the steel tension strands make monitoring of these elements infeasible with this technology. This is because any AE signal generated from damage in the concrete arch or steel strands would be attenuated before reaching the surface, where sensors would typically be placed. Given that the composite shell only plays a modest role in the structural capacity of the HCB, and this composite shell is available for visual inspection to assess damage that may develop, it was concluded that AE was not a beneficial technology looking forward.

4.3.3. Infrared Thermography

Infrared (IR) thermography has been used for a number of years for the condition assessment of concrete decks (ASTM, 2007). The technology is based on the principle that heat conduction through a material is affected by the presence of defects or discontinuities in the material, and that this disruption of heat flow manifests in observable temperature variations at the surface of the material (Manning, 1980, Manning & Masliwec, 1990, Maser

& Roddis, 1990). These variations in surface temperature can be observed and recorded with IR cameras, which image the IR energy emitted from the surface.

Infrared cameras detect the electromagnetic radiation emitted from a body, which is proportional to the fourth power of the temperature of the body. All materials emit radiation in the infrared range when their temperature is above absolute zero (-273 ºC). Infrared cameras are used to infer temperature of a material by measuring the electromagnetic radiation emitted or reflected from the surface (Bangalore, 2002). The power of emitted radiation can be expressed by the Stefan-Boltzmann equation:

$$E = \varepsilon \sigma T^4 \tag{4.1}$$

where E is the radiant energy emitted by a surface at all wavelengths, ε is the emissivity of the materials, σ is the Stefan-Boltzmann constant (5.67 x 10^{-8} W/(m²K⁴)) and T is the temperature in degrees Kelvin. The emissivity of an object is a relative measurement of rate at which the object emits radiation, 1 being a perfect emitter and 0 being no emission at all. In general, materials that are most common among civil structures, such as concrete, wood and asphalt pavement all have relatively high emissivity, between 0.9 and 1.0. The composite wrap surrounding the HCB core is expected to have a similar emissivity. The emissivity is a surface property, such that changes in the surface of the material as a result of debris, staining, oil, and water can influence the apparent temperature of the surface (Manning, 1980, Avdelidis & Moropoulou, 2003).

For concrete structures, IR has traditionally been used for the detection of subsurface corrosion damage that results in delamination in the concrete. When a subsurface delamination exists in the concrete, it disrupts heat flow through the concrete. During the warming of the day, the area above the delamination warms more quickly than the intact concrete surrounding the delamination, resulting in increased IR energy being emitted from that area. During a cooling phase overnight, the concrete surface above a subsurface delamination will likewise cool at a faster rate than the surrounding concrete and appear as a cooler area in an infrared image (Washer, 2009).

However, for the HCB beams evaluated through this research, a different approach to thermal testing was evaluated. Following the placement of the concrete in the arch section of the member, the heat of hydration developed in the arch provides a significant heat source. If this heat source is sufficient, the thermal signature of the concrete arch could be apparent on the surface of the HCB. As shown schematically in Figure 3, this would result in increased

emission of IR energy in the area of the arch, resulting in the observable signature on the surface that can be imaged using a thermal camera. This requires that the thermal energy be sufficient to penetrate approximately one inch of foam surrounding the arch, as well as the composite overwrap. If a void was present in the arch the thermal energy from hydration would not be available in the area of the void. As a result, the thermal signature of the arch would not be apparent in thermal image of the surface. Such an approach had not been previously attempted, to the knowledge of the research team. However, if effective, this could provide a critical tool for QC testing of HCBs at the time of fabrication. This approach was evaluated through the course of the research determined to be successful. Results will be described in the following sections.

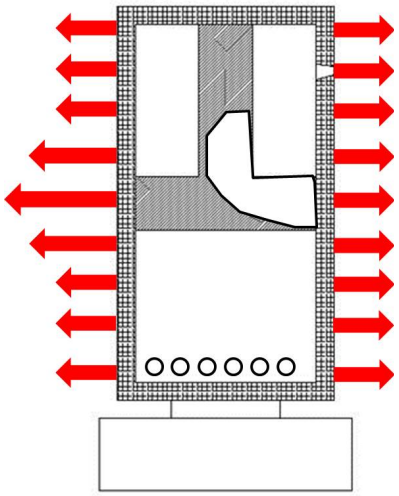

Figure 4-3 Schematic Diagram of IR Emission from a HCB During Hydration of Concrete

If such images were not collected at the time of the fabrication of the unit, the integrity of the concrete arch could also be evaluated in-service, provided that the thermal intertia of the concrete in the arch was sufficient. For such a scenario, the concrete arch would be thermally out of phase with the foam and composite that surrounds it. This would result in the arch appearing cold during the early parts of the day, when environmental temperatures are increasing, and hot during the early evening, when environmental temperatures were cooling. Again, there is no prior experience with such an approach, but this approach was evaluated through the research and found to be successful.

One of the main advantages of infrared testing is the ease of the testing procedure. The equipment is hand-held, and since it is a non-contact method, the testing can be

performed at a distance. Therefore, testing can be done quickly and without disrupting traffic, construction, or any other process on site. Access to the surface to be assessed is not required, and thermal images can be captured from distances of 100 ft. or more. For this project, thermal testing was the only technique used that could adequately detect the concrete through the FRP shell and polyiso foam core.

4.3.3.1 IR Cameras

For this research, two different IR cameras were used to collect images. FLIR S65 research-grade cameras with a temperature sensitivity of 0.08 °C and a pixel (image) size of 320 x 240 pixels were used to collect some IR images of the HCB members during the early stages of the project. A FLIR T620 with a temperature sensitivity of 0.04 °C and an image size of 640 x 480 pixels was also used. The selection of the IR camera was based simply on the availability of the camera; either device has adequate capabilities to conduct the inspections.

4.3.4. Tap Testing

A simple method for searching for delamination and debonded areas is by mechanical sounding. This method consists of using a metal or plastic object to strike the surface of the composite material and listening to the tone of the impact. Delaminated areas can frequently be found located from their distinctive hollow tone. This method can also be used to find delamination in concrete and delaminations between concrete repair materials and the original concrete.

Sounding has been implemented for aerospace structure utilizing a quarter, and hence, is commonly referred to as a coin-tap test. The low mass of a coin results in a high-pitched tone that can reveal delamination between layers of composite and possibly between the composite and the bonded substrate. For deeper features, a larger mass should be used such that the depth of the material is excited by the tapping. For composite retrofits on civil structures, a rock hammer or other suitable impact device may be used, though care should be taken to avoid damaging the composite material. The use of hammers allows for detection of features further from the surface, but near-surface features such as delamination between layers of composites, may be obscured. A 0.25-in. to 0.5-in. steel rod, approximately 6 inches in length, can also be used effectively in civil retrofit applications. The advantage of using this type of device is that it is readily available, in that it can be formed from a piece of rebar

and can provide both a high-mass and low-mass impactor depending on the orientation of the rod when impact is made.

Tap testing was utilized in this project to test the composite shell for one of the HCB members. However, IR technology is also well suited to this application, and since thermal images of all of the surface areas of all of the members was planned, tap testing was not utilized otherwise. Additionally, tap testing requires hands-on access to the entire area to be tested. As noted above, thermal imaging does not require this level of access, and is therefore more efficient and practical than tap testing.

4.3.5. Magnetic Flux Leakage

Magnetic flux leakage (MFL) is and NDE technology with the potential for detecting fractured prestressing strands embedded in concrete, and has been a topic of research for several years (Ciolko, 1999, Ghorbanpoor, 2000). This technology may have application for condition assessment of the strands that form the tie of the HCB members

The MFL method works by inducing a magnetic field within the prestressing steel strands, and detecting the leakage of that field that results from sudden discontinuities in the strand (i.e. fractured strand or section loss)(Makar & Desnoyers, 2001). The process of damage detection in the strand is analogous to the process involved in magnetic particle testing (MT). For MT, finely divided iron particles are attracted to magnetic fields leaking from a crack in the surface of the steel. For MFL, the leaking magnetic fields are detected using coils, Hall effect or SQUID (superconducting quantum interference device) sensors (Ghorbanpoor, 1998, Krause et al., 2002). This enables detection of the leaking field through significant air gaps or concrete cover of between 5-in. up to more than 11 inches, according to research results reported in the literature (Ghorbanpoor, 2000, Scheel, 2003). For the case of an HCB, the composite overwrap and the polyiso foam are diamagnetic materials that will behave similarly. The method, as applied for a prestressed beam, is shown schematically in Figure 4-4. Rare earth magnets are typically used to provide opposing poles, separated by some distance such that the magnetic field between the poles penetrates the concrete, and induces a magnetization in the embedded steel strand and any other ferromagnetic material (i.e. steel) in the area, such as stirrups or other mild reinforcing.

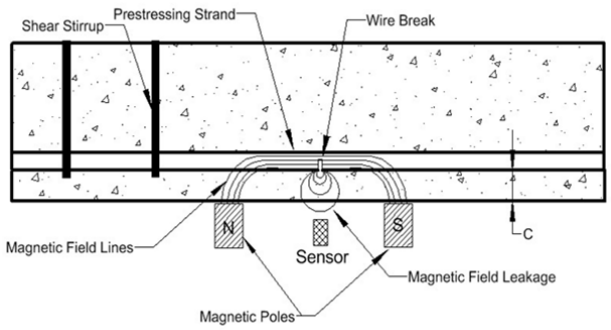

Figure 4-4 Magnetic Flux Leakage Test Schematic

A sensor is used to measure the ambient magnetic field level at its position between the magnetic poles. The sensors and magnets form a sensor head that is scanned across the surface of the concrete axially aligned with the embedded steel strand. Sudden changes in the geometry of the embedded steel, such as a broken wire, result in a sudden change in the ambient magnetic field as the sensor head is scanned along the surface (Gaydecki et al., 2007). Changes in the cross-sectional area of the steel within the aperture of the sensor head also results in variations in the ambient magnetic field levels. These changes are less localized in nature relative to the response created by a fractured strand. Mild steel, such as stirrups and other reinforcing, also result in variations of the ambient magnetic field measured, which can complicate interpretation of results (Gaydecki et al., 2007). Varying concrete cover can also create variations in the measured ambient field. However, even with these recognized limitations, the MFL approach provides a potential solution to nondestructively detecting broken and corroding strands embedded in concrete, and may also provide a technology for assessing the prestressing strands that form the tie of the HCB.

An example of the current state of the technology is shown in Figure 4-5. Figure 4-55A shows a plan view of an MFL unit; Figure 4-5B shows the orientation of an MFL unit in use on the soffit of a box girder bridge. This figure shows a MFL unit developed at the University of Wisconsin (Ghorbanpoor, 2000).

Research in the U.S. has typically focused on measuring the leakage field resulting from direct induction, i.e. during magnetization. An alternative approach is to utilize remnant or residual magnetization resulting from magnetizing the embedded steel. Electromagnetics are used to magnetize the embedded steel from distance up to ~12 inches (Scheel, 2003). The resulting magnetization of the embedded steel, which remains (at a reduced level) after the electromagnet is removed, creates a dipole in the area of a fracture of the strand or wire

(Makar & Desnoyers, 2001, Scheel, 2003). Some research has suggested this method is more effective than induced magnetic fields; however, comparison data is limited.

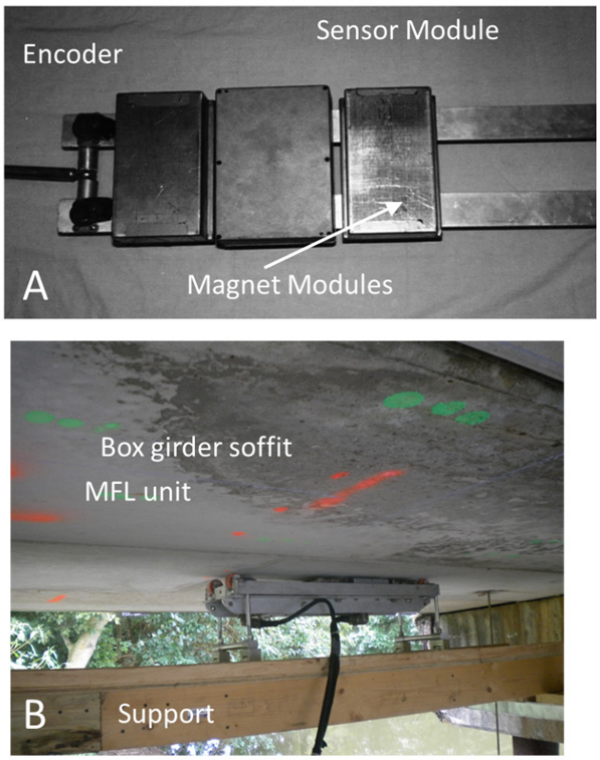

Figure 4-5 (A) MFL System Components, (B) System Deployed on a Prestressed Box Girder

Currently, MFL technology is not sufficiently developed to have been evaluated during the course of this research. The technology is experimental in nature, with the only systems available being research prototypes developed at the University of Wisconsin. However, in the longer term, such a technology may provide an important tool for detecting damage in the prestressing strands that form the tie of the HCB.

4.4. MOCK-UP BEAM

Due to the inability to monitor the concrete flow through the constricted cavity during the concrete arch pour in addition to the limited slots in the FRP lid that are drilled for the pour process, the contractor fabricated a mock-up, that simulated B0439 HCBs, before their construction. The mock beam was constructed using transparent Plexiglas in place of one FRP web to allow monitoring the concrete flow during the pour. Plywood was used to support the Plexiglas and work as a form for the beam, since the FRP shell executes that role during the arch pour. Foam and shear connectors were placed as in the original HCB, while

the prestressing strands were not included in the mock beam. To further increase the flow of the concrete during the arch cast, the pour team shook the shear connectors by hand. Figure 4-6 and Figure 4-7 illustrates the mock beam before and after the arch pour respectively. The mockup beam, shown in Figure 4-6, was only one-half of the length of the actual HCB, since the concept was to have concrete pushing itself down from the middle of the arch until the end block. As it is clarified by Figure 4-7, the beam provided visual verification for the teamwork that the SCC would flow properly around the shear connectors located throughout the arch.

Figure 4-6 Mock-UP Beam Simulates HCB of B0439 (before pour)

Figure 4-7 Mock-Up Beam (one day after pour)

Additional QC/QA tests were performed on the mock beam. These tests included: slump flow tests (following ASTM C-1611), J-ring tests (following ASTM C-1621), and standard compressive strength tests (following ASTM C39 / C39M). These tests aimed to ensure the flow of the concrete around the shear connectors and examine the mixture qualification. Figure 4-8 and Figure 4-9 illustrate performing the slump flow test with and without j-ring and measuring the difference in slump flow. The differences in the performed tests were less than 2-in. indicating good passing ability of the SCC. Samples of compressive test results that were performed during the mock beam pour are presented in Table 4-1. The results show that the concrete at the sixth day gained compressive strength higher than the target compressive strength of the three bridges arches, which is 6000 psi.

Steel Slump Cone

Figure 4-8 The Slump Flow Test Without J-ring

Plastic Plate

Figure 4-9 The Slump Flow Test With J-ring

J-ring

Table 4-1 Sample of the Compressive Strength Test Results for the Mock Beam

No. of Cylinders	Test Age (Days)	Average Compressive Strength (psi)
3	2	4417
6	6	6081
3	8	6346
3	9	6499
3	11	7447

4.5. SCC MIX DESIGN AND STANDARD COMPRESSIVE STRENGTH TESTS

The mix design and proportioning of SCC is different from normal concrete. The design process is focused on balancing the fluidity, stability, and strength of the concrete. A typical mix design generally contains lower coarse aggregate volume and higher paste (cementitous, water, and fine aggregate material) volume to fulfill the required flowability. Lowering the coarse aggregate content in the design mix also reduces the risk of aggregate segregation. The stability of the SCC mix is directly related to the ability of the concrete to resist segregation. For typical SCC mix design, the coarse aggregate to total aggregate ratio (by volume) ranges between 50% and 55%. If the ratio is higher than 55%, Viscosity Modifying Admixtures (VMA) may be needed to stabilize the mix.

The water content in the SCC mix is also of great importance, sine it affects the consistency and properties of the paste and the effectiveness of the HRWR. A typical SCC will have W/C ratio less than 45%. Since, small changes in water content can be the difference in the concrete not having the ability to properly flow to severe aggregate segregation, attentiveness should be paid to control the aggregate moisture during the mix design and production of SCC.

Table 4-2 and

Table 4-3 illustrate the mix design of the SCC used in B0439 and B0478 respectively. The mix design of the SCC used in B0410 is not available. As a part of the QC/QA program, standard compressive strength tests were performed on the concrete of the HCBs arches. The average compressive strengths of the three bridges SCC are presented in Table 4-4. The strengths are higher than the target compressive strength of 6000 psi.

Table 4-2 Mix Design of SCC of B0439 (By Peterson Gravel & Ready Mix, Inc.)

Product	**Content**	**Yield**	**Comment**
Type I Cement	600 (lbs)	3.05 (ft^3)	
Type C Fly Ash.	200 (lbs)	1.22 (ft^3)	
3/8" Gravel	1770 (lbs)	9.61 (ft^3)	
Sand	1200 (lbs)	7.34 (ft^3)	
Water	280 lbs (33.6 gal)	5.4 (ft^3)	
PolyHeed N	3 oz/cwt	N/A	Mid-Range Water Reducer
Glenium 7500	8 oz/cwt	N/A	Mid-Range & High-Range Water Reducer
Delvo	3 oz/cwt	N/A	Retarder & Water Reducer / Retarder
Rheomac VMA 362	2 oz/cwt	N/A	Viscosity Modifying Admixture
Total Yield		27.28 (ft^3)	
Water / cement ratio		0.35 lbs/lb	
Fly Ash / cementious		0.25 lbs/lb	

Table 4-3 Mix Design of SCC of B0478 (By Plottie Ready-Mix, LLC)

Product	**Content**	**Yield**	**Comment**
Type I Cement	600 (lbs)	3.05 (ft^3)	
Type C Fly Ash.	200 (lbs)	1.22 (ft^3)	
3/8" Pea Gravel	1570 (lbs)	10.02 (ft^3)	
Big River Sand	1325 (lbs)	8.43 (ft^3)	
Water	280 lbs (33.6 gal)	4.5 (ft^3)	
Grace-Adva 140M	3-5 oz/cwt	24-40 oz/yd^3	High-Range Water Reducer
Grace-Adva Cast 575	7-10 oz/cwt	56-80 oz/yd^3	Mid-Range & High-Range Water Reducer
Grace-Recover	4-6 oz/cwt	32-48 oz/yd^3	Hydration Stabilizer
Grace-V MAR 3	1-2 oz/cwt	8-16 oz/yd^3	Concrete rheology-modifying admixture (Viscosity Modifying Admixture)
Total Yield		27.21 (ft^3)	
Water / cement ratio		0.35 lbs/lb	
Fly Ash / cementious		0.25 lbs/lb	

Table 4-4 Average Compressive Strength (psi) of SCC used in the three bridges

Bridge	Test Age (Days)	Average Compressive Strength (psi)
B0439	28	8525
B0410	28	10800
B0478	28	8925

4.6. NDE OF HCB'S ARCH VIA INFRARED THERMOGRAPHY

The application of the infrared thermography as a QC/QA tool and as an in-service monitoring device is discussed in the following sections. This technology has application for voids in the concrete arch and delamination of the composite overwrap. During the course of the project, no delamination of the composite material was observed; consequently, the following sections focus on the application of IR testing on the arches.

The results show that the thermal testing during the fabrication of beams, while concrete was curing, was effective. The results have also clarified that voids or any other defects in the concrete were not typical, except for one beam in the second bridge, B0410.

4.6.1. Camera Procedure and Placement

Throughout this project, thousands of thermal pictures were taken of the three bridges. When taking these thermal pictures, certain procedures needed to be followed in order to achieve the most accurate results possible. As stated above, certain environmental characteristics need to be observed as well.

For the best results, the camera first needs to be focused properly. If the screen is not focused properly, the picture produced will be blurry and the temperatures of the material will not be accurate. If the temperatures are not accurate, the temperature contrasts between the material and surrounding environment will be incorrect, making it difficult to detect any flaws or defects in the material. It is not necessary, but the camera can be placed on a tripod to steady the picture as well.

When taking the thermal pictures, where the camera stands is also important to the quality of the picture. For these tests, the camera was placed in two different locations relative to the HCBs during the testing. One location was located next to the beam. The camera would face down the length of the beam in order to take a isometric picture of the HCB, or, in other words, a picture of the length of the concrete arch, at a low angle. An example of these pictures, along with a diagram of the camera's placement, can be seen in

Figure 4-10. This location next to the beam was used on bridges B0410 and B0478 because of the placement of the beams. In B0410, the pictures were taken at the pour site. The HCBs were placed very close together in order to make it easier on the pump truck during the pouring. Due to this location, the isometric pictures needed to be taken as there was no room for a detailed picture of the entire height of the beams. This was also true for Bridge B0478. For this bridge, since the beams were placed on the abutments before the concrete was poured, the beams were too close to each other to achieve a full height detail picture on the interior beams.

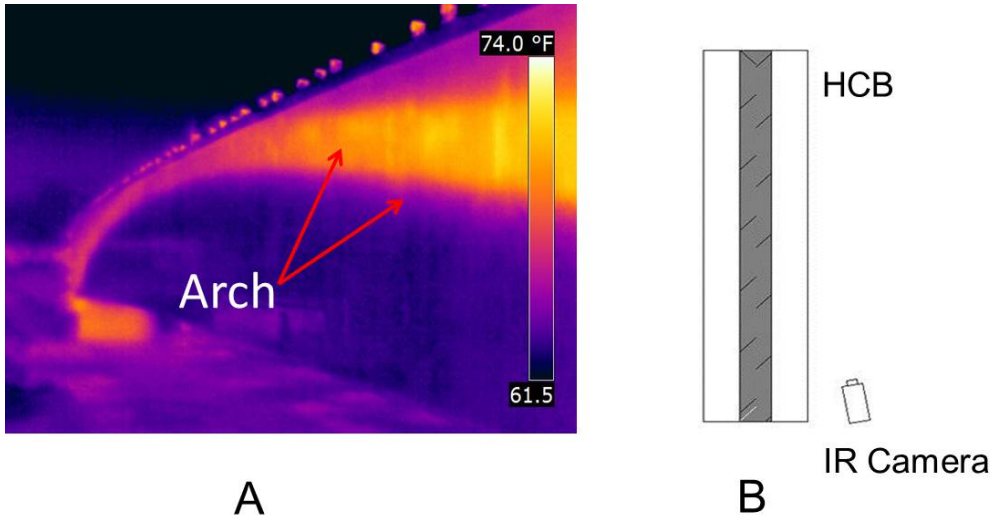

Figure 4-10 (A) IR Picture of HCB Length in B0478 and (B) Diagram of Corresponding Camera Location

The other camera location was directly perpendicular, or normal, to the surface of the beam. This location resulted in better thermal results than the profile location described above. The camera was placed facing perpendicular to one face of the HCB about 10 to 15 feet away from the beam. This placement produced a full detail picture of the full height of the beam. An example of a thermal picture for this camera placement, along with a diagram of the camera's placement, can be seen in Figure 4-11. This type of camera location was used for thermal testing, when possible, for all three bridges.

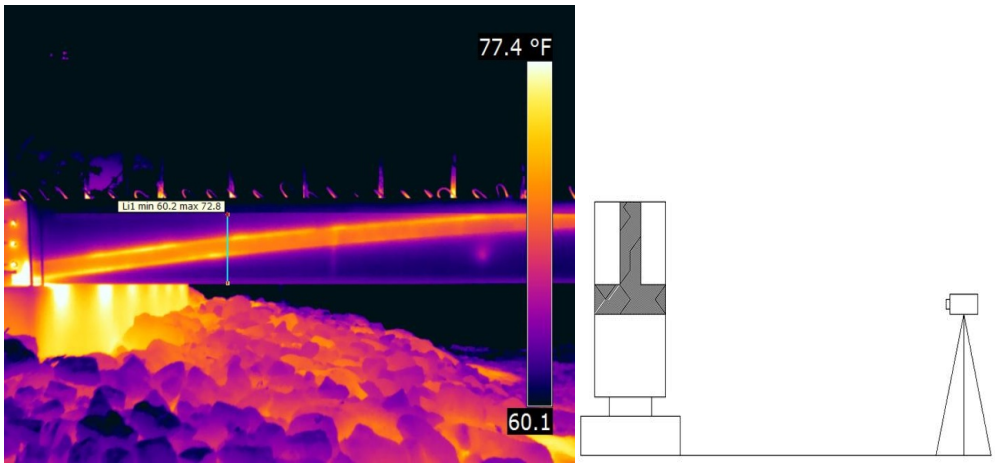

1.1.1. (A (B)

Figure 4-11: (A) Thermal Picture Perpendicular to HCB, (B) Diagram of Corresponding Camera Location Mockup Testing

The camera placement is an important consideration looking forward toward implementing the IR technology as QC tool. To provide the best images, allocation of adequate spacing for the camera to be position normal to the surface is required. When the concrete arch is placed in a fabrication yard, this space can be provided by properly positioning equipment and positioning the beams at an adequate spacing, typically 15 to 20 ft. apart. When casting of the arch occur in-place at the bridge site, positioning the camera to be most effective is more problematic, although images can still be captured effectively, as shown in Figure 4-10.

4.6.2. Mock-up IR Testing

The mock-up of the HCB was tested using the S65 thermal camera as a proof of concept test to establish if the proposed methodology for assessing the integrity of the concrete arch was implementable. The forms for the mockup specimen consisted of Plexiglas and plywood, as discussed previously. It was found during the testing that the thermal signature of the arch could not be imaged well through the Plexiglas wall of the form. These materials are often opaque in the IR range, so this result was not unexpected. Thermal images of the plywood wall of the form clearly showed the thermal signature of the concrete following placement. Figure 13 illustrates a thermal image of the concrete arch, along with a photograph of the mockup. Note that the photograph of the mockup is taken from the side with a Plexiglas wall, and shows the void prior to concrete placement. The thermal image is taken from the opposite side of the specimen, and as such has the opposite orientation.

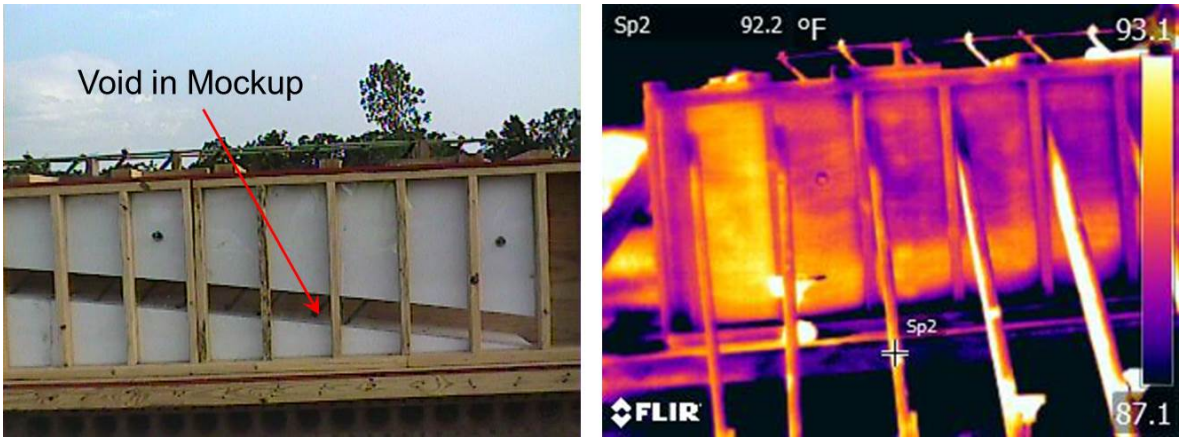

Figure 4-12: A Photograph (left) and a Thermal Image (right) of the Mockup Specimen Showing Concrete Arch

This initial test indicated that the concept of imaging the thermal signature of the concrete arch during the hydration of the concrete was a feasible approach. The general form of the concrete arch is apparent as a thermal contrast in the image, represented by different colors. This "thermal signature" of the concrete arch results from the heat of hydration of the concrete, as previously mentioned.

4.6.3. HCBs IR Testing

The application of the infrared thermography for QC testing of the HCB was demonstrated through the project. The procedure for acquiring IR data was to utilize a hand-held infrared camera to acquire data from a standing position adjacent to the HCB. A typical IR image is shown in Figure 4-13. This figure, which was acquired 24 hours after the concrete pour, illustrates how the process works. As shown in the image, the heat of hydration of the concrete in the arch results in a thermal signature on the surface of the concrete that images the internal arch. This thermal signature is revealed through the foam inserts and the composite wrapping that surrounds the arch.

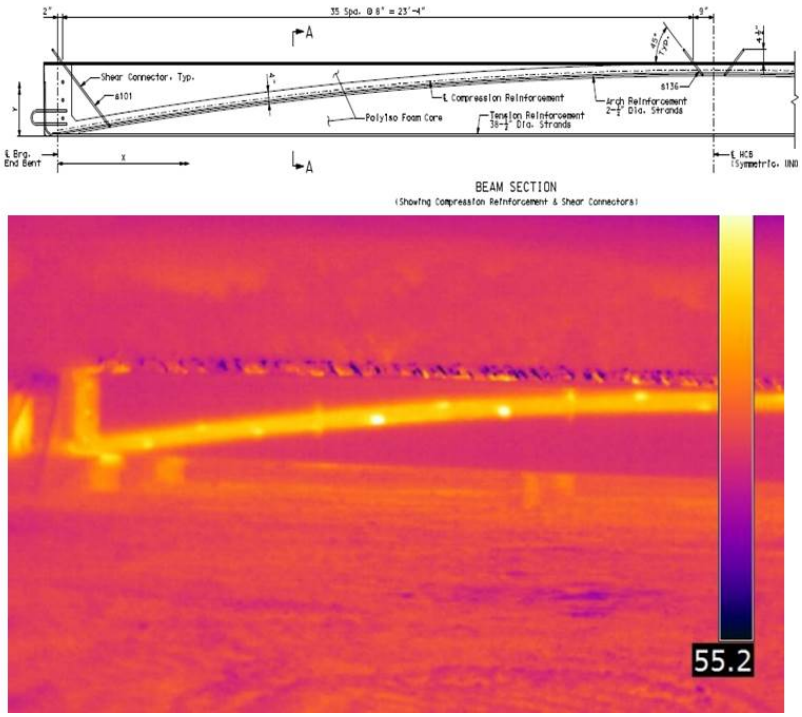

Figure 4-13 Example of thermal inspection showing thermal signature of the arch during the hydration of concrete

Testing was completed during the fabrication of each of the three HCB bridges; for two of the bridges, the testing was completed at the fabrication yard, and for the third bridge, shown in Figure 4-14, testing was completed during the erection process. In this figure, a section of the arch cast the previous day is imaged using the IR camera. Workers on the bridge shown in the photograph (Figure 4-14, right) are placing concrete on the next span, the following day.

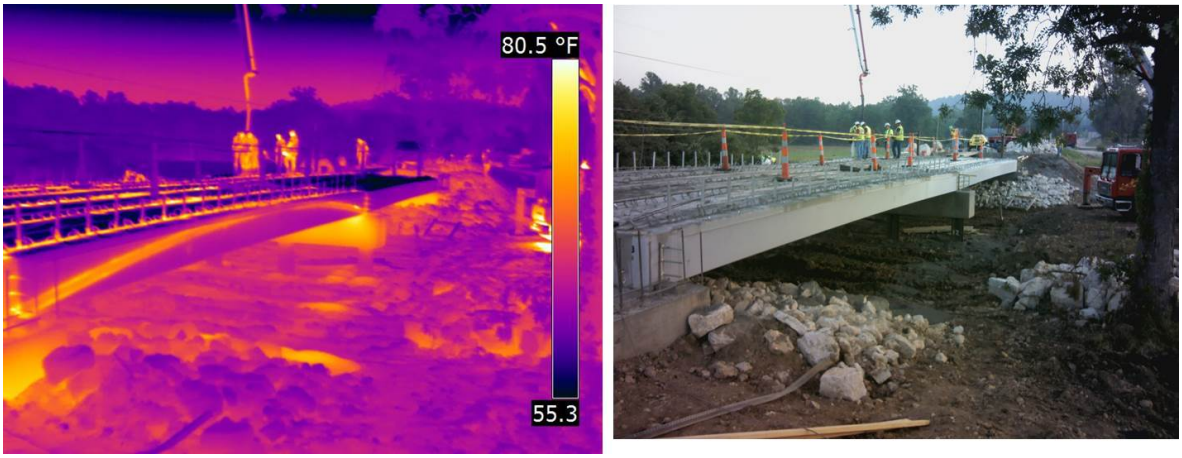

Figure 4-14 Example of IR Image (left) and Photograph of HCB Being Placed in the Field

Unlike the detection of subsurface defects in concrete, such as corrosion-induced delamination, the detection of the internal arch is not weather dependent, since the arch is generating its own heat source and as such can be imaged regardless of the temperature conditions. Caution should be used in the case of rain, simply because the presence of water on the surface will obscure the thermal image.

Testing was completed at various times following the concrete pour, ranging from 4 to 48 hours to determine the optimum times for conducting the tests. The temperature contrast was determine from the equation:

$$T_{contrast} = T_A - T_B \tag{4.2}$$

where:

T_A = Apparent temperature on the surface of the HCB above the concrete arch and

T_B = Apparent temperature on the surface of the HCB

Figure 4-15 shows a typical location that was selected for calculating the temperature contrast on the surface of the beam. This contrast can be determined to optimum times for inspection, to quantify the temperature contrast developed from the hydration of the concrete, or to quantify the contrast resulting from ambient temperature variation once the hydration of the concrete is complete.

Figure 4-15 Figure illustrating how temperature contrast was determined.

Figure 4-16 shows the temperature contrast for the arch over a 48-hour time period. This figure represents the general behavior of all of the HCB's studied during the research, and shows that the optimum time for conducting an inspection for QC purposes is approximately 24 hours after the concrete in poured. The thermal contrast between the composite shell surface above the arch and other surface areas was approximately 9 °F at this point in time, and was reduced at later measurement times. Images captured as late as 48 hrs. after placement of the concrete still provide adequate thermal contrast to enable imaging of the concrete arch. From these data, the time period over which QC testing of the arch using IR should be conducted is approximately 6 hours to 48 hours after the placement of concrete, with the optimum time being ~24 hours after placement.

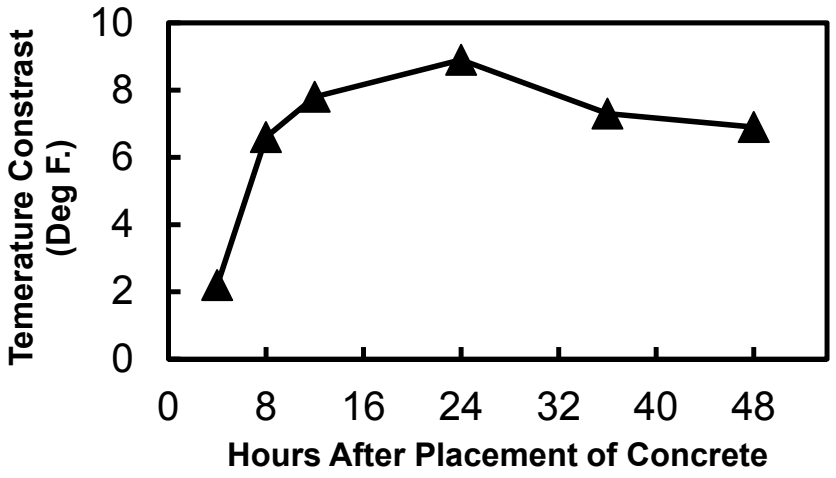

Figure 4-16 Temperature Contrast at Surface Caused by Concrete Arch

4.6.3.1 Detection of Voids

Thermal images were captured for each of the HCB bridges, typically 24 hrs. and 48 hrs. after the concrete placement. Generally, these images reveal an intact arch producing a strong thermal signature on the surface of the HCB. However, during the casting of Beam 1 of bridge B0410, the placement of the concrete resulted in several voids in the concrete arches for each web of the member. These voids were apparently caused by a lack of workability of the concrete, possible due to concrete beginning its set prior to placement. The presence of the voids in the concrete arch was recognized by the on-site QC personnel, because the concrete was not rising in the forms in certain locations along the length of the girder. These voids were detected in the thermal images captured 24 hours after the pour. Figure 4-17 illustrates the detection of the voids in the thermal images, in a composite image

formed by combining separate, individual thermal images of portions of the beam (equipment placement surrounding the HCB during casting precluded collected a single elevation along the entire length of the member). The thermal images were somewhat blurred due to high humidity at the time of the testing, which cause the auto-focus function of the camera to not perform well. However, the composite image shown below, which consist of individual images collected along the length of the girder, clearly shows the voids in the arch of the beam. Shown in the figure is the West web (A) and the East web (B) of the double – web HCB for bridge B0410. The void maps developed by on-site QC personnel are also shown to verify the thermal imaging results.

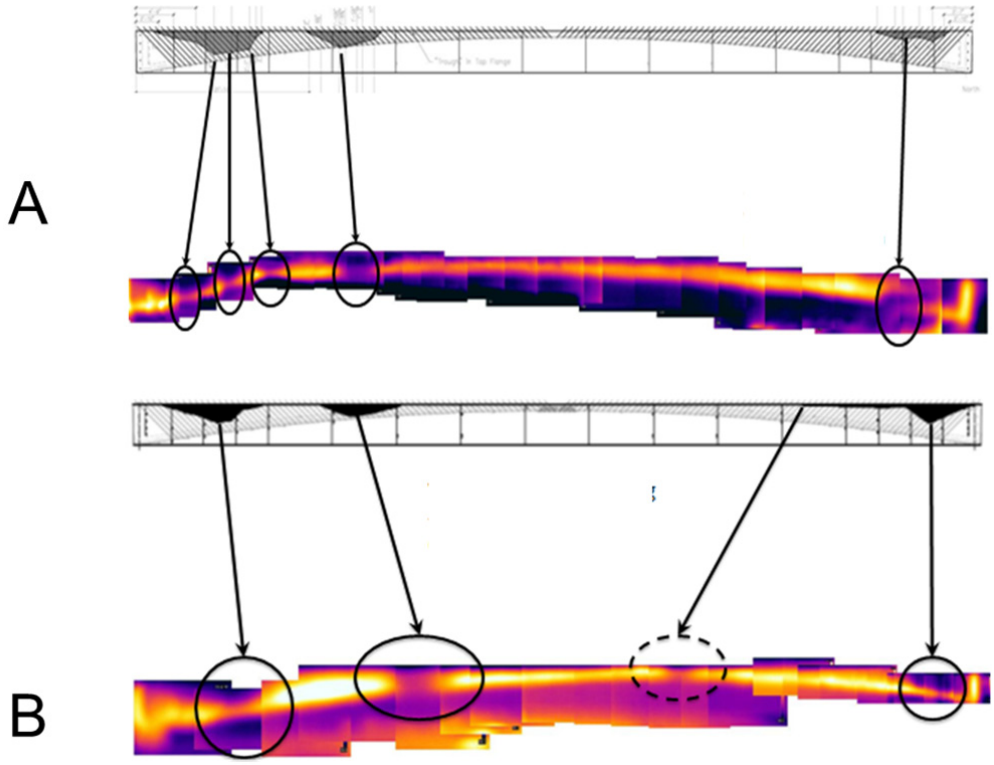

Figure 4-17 Composite Thermal Images of the West (A) and East (B) Webs of Beam 1, HCB B0410

The voids in the member result in the thermal signature of the arch disappearing at the locations of the voids, since the heat of hydration of the concrete is not available at locations where the concrete is missing, i.e. a void. Figure 4-18 quantifies the thermal detection of one of the voids detected in this member. As shown in the figure, the signature of the concrete arch is not apparent in the thermal images; the temperature variations along a line shown in

Figure 4-18A are shown in Figure 4-18B. Note that these data were obtained 48 hours after concrete placement.

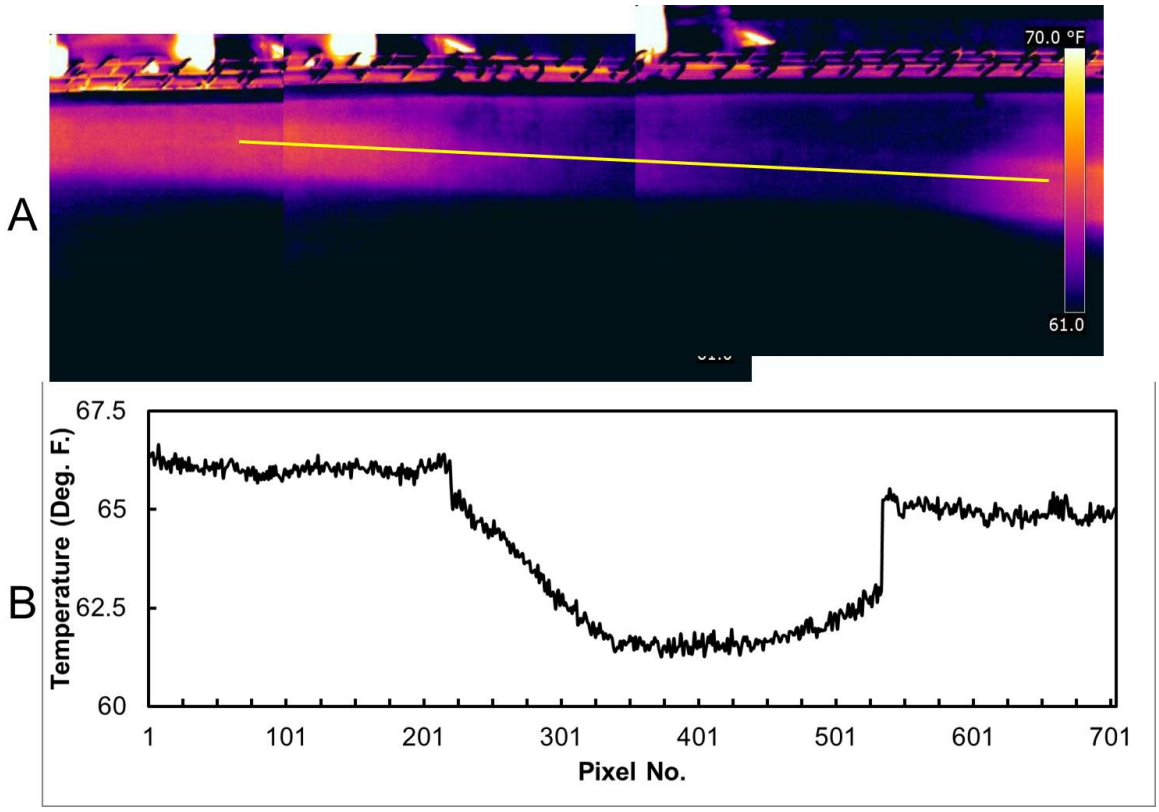

Figure 4-18 Composite Thermal Image of Void in B0410 (A) and Temperature Variations along the Line Shown in (B)

These figures clearly illustrate the ability of the thermal method to detect the presence of voids in the arch, through the polyiso foam and composite overwrap that surrounds the arch. Given that this area in unavailable, generally, for visual inspection, this technology will provide an important tool for QC/QA testing at the time of casting of the arch, either in the field or in the fabrication yard. For the example shown here, the voids could also be detected from the top of the arch, however, voids or honeycombs may also occur without being apparent through the top of the member. The thermal method is an effective way to detect these voids.

4.6.3.2 Anomalies

During the course of testing, there were a consistent pattern of anomalies appearing in the thermal images. These anomalies were represented by periodic “hot spot” appearing on

the images, usually at location on or near the surface above the arch during the hydration of the concrete. Figure 4-19 illustrates some of the thermal anomalies observed. These “hot spots” may have resulted from the concrete placed in the arch void leaking through the polyiso foam, resulting in a larger thermal contrast reaching the surface of the composite shell in localized areas adjacent to the arch. These “hot spots” have greater thermal contrast than the arch itself, indicated that the heat of hydration is conducting across less material, that is, this is concrete that has pushed through the foam included in the HCB, and hence is closer to the surface.

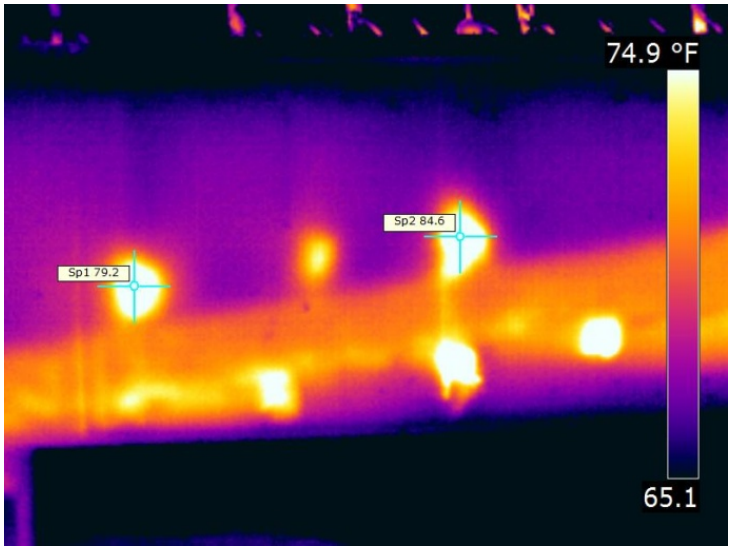

Figure 4-19 Images Showing Thermal "hot spots" Typically Observed Following Concrete Placement

These anomalies were further assessed during testing 1 and 2 years after placemen of the concrete. Figure 4-20 illustrates the locations of the anomalies one year after concrete placement for bridge B0439. As shown in these figures, the anomalies generally follow the thermal pattern of the concrete arch, that is, they are warmer during periods when the composite shell is cool, and cooler during periods when the composite shell is warm. This is due to the thermal inertia of the arch, which is out of phase with the variations in the surface temperature of the composite shell. As a result, these anomalies appear as “hot spots” during the nighttime, and “cold spots” during the warming cycle of the day. Thermal inertia or thermal mass, $\boldsymbol{I}$, is a measure of the ability of the material to conduct and store heat. It is computed as the square root of the product of thermal conductivity ($\boldsymbol{k}$), density ($\boldsymbol{\rho}$), and heat capacity ($\boldsymbol{C_p}$) as:

$$I = \sqrt{k\rho C_p} \tag{4.3}$$

Heat capacity (i.e. specific heat) is defined as the amount of heat needed to raise the temperature of a unit mass of a material by one degree. This property describes the ability of material to store heat. The volumetric heat of a material can be calculated as the product of the density and the specific heat of the material. It is a measure of the quantity of heat required to produce a unit temperature change in a unit volume (Lienhard, 2011). For the HCB, the significant thermal inertia of the concrete arch results in the temperature of the arch being out of phase with the surface temperature of the HCB in areas other than above the arch. These data indicate that these anomalies are part of the arch, i.e. this is concrete that has leaked through the foam to be in contact with the composite shell.

It is also possible that some of these thermal anomalies result from steel connection or fasteners that are in contact with the composite shell and embedded in the concrete, such that they follow the thermal pattern of the arch and conduct heat toward the surface of the composite shell. Regardless, these anomalies are not believed to be detrimental to the performance of the HCB.

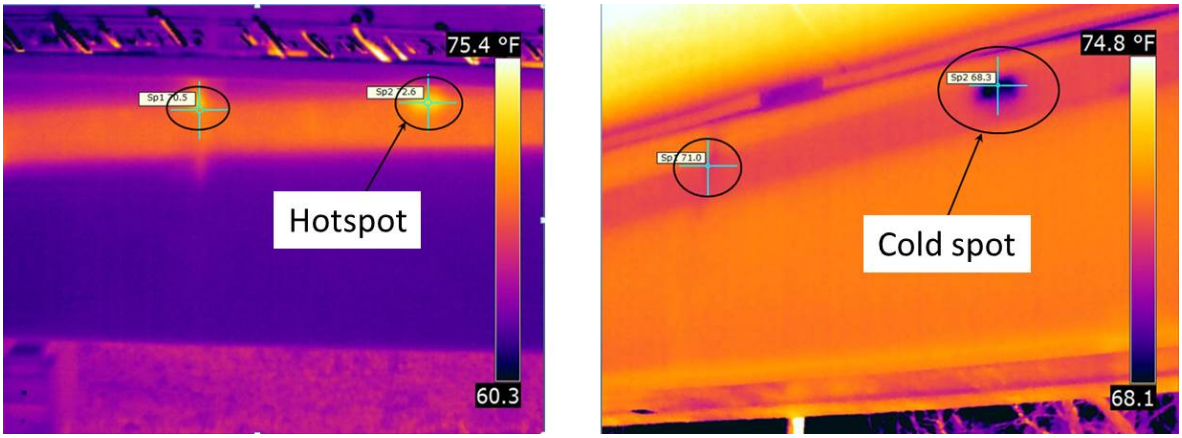

Figure 4-20 Example of Anomalies Observed in the Area of the Arch One Year during the Night (left) and During the Day (right)

4.6.3.3 Tests conducted 1 or 2 years after placement

The arch of Bridge B0439 was place in August 2011. Thermal images were captured at the time of the casting, as well as in March, 2012 (seven months after casting) and in April 2013. These data were collected to determine if the concrete arch was apparent in thermal images when the heat of hydration had thoroughly dissipated. The results of these tests indicated that the concrete arch could be imaged after the hydration of the concrete was

complete, due to the thermal inertial differences between the concrete arch and the surrounding foam. Figure 4-21 illustrates the behavior of the concrete arch during the morning and evening hours. Figure 4-21A shows a thermal image of the HCB at 6 pm in the evening, at which time the concrete arch appears cooler than the other portions of the HCB shell. The temperature gradient along the line shown in Figure 4-21A is shown in Figure 4-21B. These data illustrate the actual temperature variation between the composite shell and the arch signature. Figure 4-21C shows an elevation of the HCB at 5 am in the morning. In this image, there is a significant gradient through the depth of the member, as illustrated in the gradient along the line shown in Figure 4-21D. This gradient results from the significant thermal energy stored in the concrete deck and parapets of the structure. Because these concrete elements store the thermal energy from the previous day, conduction of this thermal energy into the HCB results gradient through the depth. This gradient results in the arch signature being difficult to observe in the image, relative to the image captured at 6 pm.

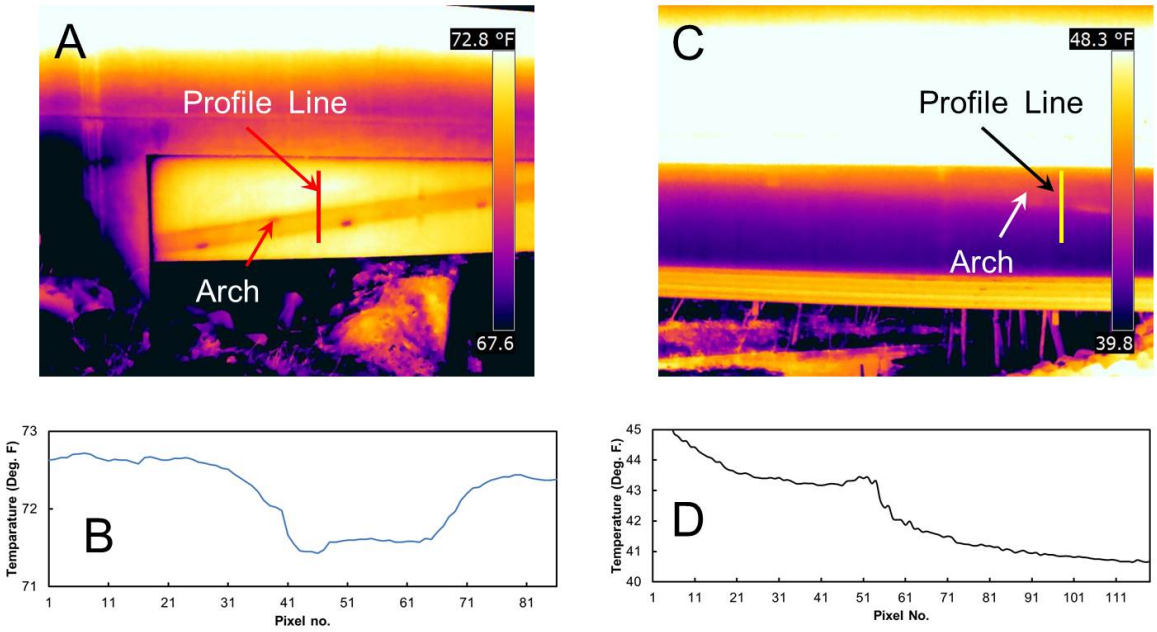

Figure 4-21 Thermal Images of B0439 20 Months After Concrete Placement Showing HCB at (A) 6 pm with Thermal Profile (B), and (C) 5 am with Thermal Profile (D).

The thermal contrast between the concrete arch signature and the composite shell was monitored over a 24-hour period to determine the optimum times to conduct an inspection intended to image the arch. As shown in Figure 4-22, the greatest thermal contrast between the concrete arch and the composite shell occurs in the early morning hours, prior to sunrise. However, as noted above, the thermal images may be more difficult to interpret at this time

due to the thermal gradient along the elevation of the member. It should also be noted that the behavior of the concrete arch is opposite of, for example, a delamination in the composite shell would be. A delamination in the concrete shell would be cold in the overnight hours, when that arch signature is warmer than the surrounding area. During the day, a delamination would appear warmer than the surrounding area. As a result, such a defect could be easily discerned from the arch signature. However, no defects of this type were observed over the course of the project.

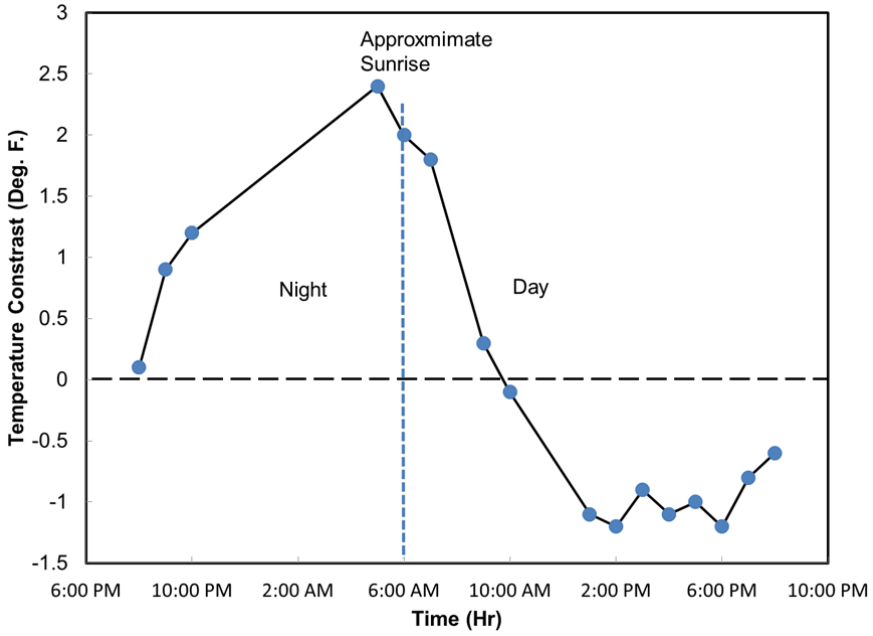

Figure 4-22 Thermal Contrasts Over a 24 Hour Period for B0439, 20 Months After Placement of Concrete Arch.

4.7. END BLOCK CURE TEMPERATURE OF B0439

During the concrete arch placement of B0439 HCBs, three thermocouple sensors were placed in HCB elements and attached to a maturity meter. The thermocouples were placed: in the center of the chimney, 2" below the top of the chimney, on the exterior edge of the FRP shell that encapsulated the chimney, and in a concrete cylinder as a control to gain an understanding of the thermal behavior of the hybrid composite beam during concrete placement and curing. The setup of the maturity meter is shown by Figure 4-23.

Figure 4-23 Overview of Maturity Meter Setup

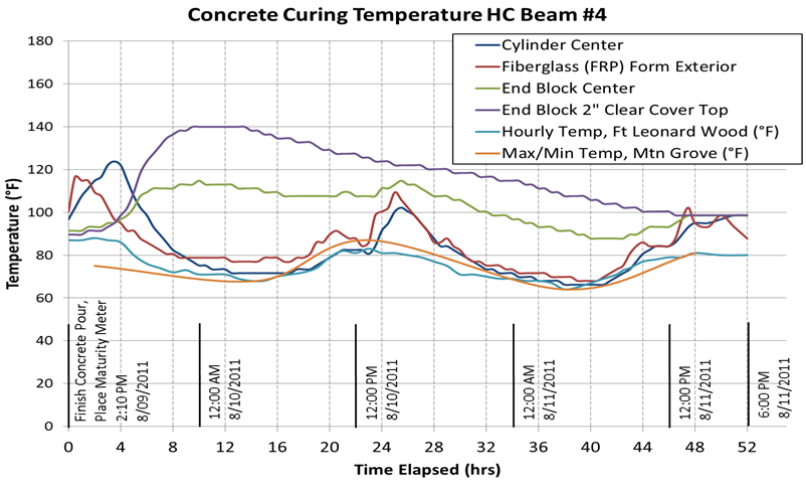

Figure 4-24 Curing Temperature Profile of HCB Member, B0439

The temperature changes for the different locations can be seen in the temperature profile, Figure 4-24, in comparison with the ambient temperature taken from the weather station data at Mountain Grove and the nearby Fort Leonard Wood, Missouri, USA. The resulting values are indicative of the strength development in the concrete end block and consistent with exothermic process of the Portland cement hydration explained by Mindess and Young (1981) and Lachemi et al. (1997). Results show that the thermocouple located 2" below the top of the end block captured the peak temperature rise within the member during placement of the concrete arch. In addition, the composite shell temperature rise during the day was also noteworthy. However, the FRP shell and the standard concrete cylinder suffered lower levels of temperature rise during the concrete cure. This can be attributed to the exposure of the cylinder and FRP shell to the surrounding environment, which probably allowed them to dissipate temperature by convection. The rise in their temperature at noon, which can be attributed to the exposure to the sunrays, assures that they were affected by the

surrounding atmosphere. On the other hand, the concrete inside the chimney was encased in the FRP box which prevented them from being affected by the surrounding environment and dissipating temperature.

The thermocouples were placed within the chimney and the adjacent FRP shell because it was thought that the peak hydration temperature would occur in the end block where the concrete mass was greatest. However, the data recorded after the arch pour of B0410 HCB2, demonstrated that the maximum hydration temperature took place within the arch close to the beam midspan. An interpretation for this behavior along with more explanation to the thermal changes after the concrete pour are presented in the following section through the analysis of the early-age behavior of B0410 HCB2.

4.8. EARLY-AGE BEHAVIOR OF B0410

Figure 4-26 displays the change in the concrete temperature at sec. (B-B) (thermistor #2) during the first 24 hours after the beginning of the concrete arch pour of HCB2. The hydration of Portland cement is highly exothermic process. Mindess and Young (1981) and Lachemi et al. (1997) divided the Portland cement hydration process into five phases. In Phase 1, the heat is rapidly evolved for a short period during the initial mixing. Thereafter, a dormant period (Phase 2) starts for several hours. During this phase, the concrete remains plastic. Once the dormant period ends, a vigorous reaction between the calcium silicate in the cement and the water begins until a maximum rate of heat evolution is reached. Final set occurs during this acceleration phase (Phase 3). Then, the heat generation continues but with slow rate. The concrete temperature rises slowly during this phase (Phase 4) until the peak hydration temperature is reached by its end. During the final phase (Phase 5), the heat generation is minimal and the concrete loses heat until a state of equilibrium is reached with the surrounding environment.

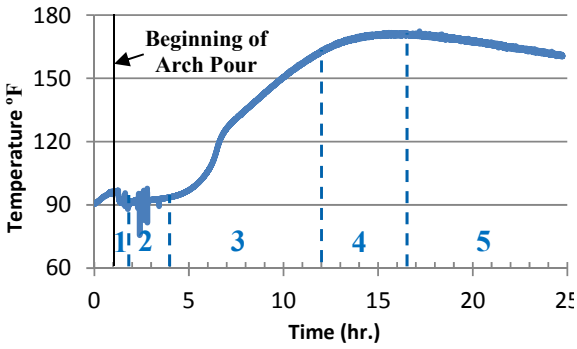

Figure 4-26 Concrete Temperature during Hydration Process at VWSG/T2

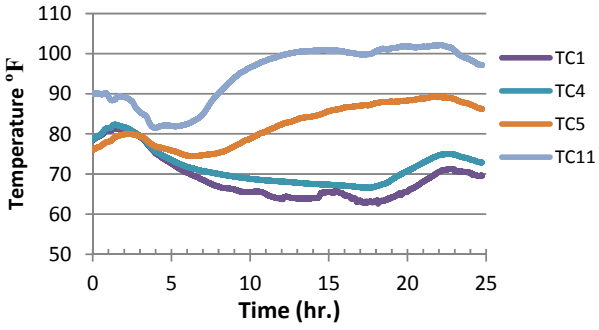

Figure 4-25 Strands Temperature of HCB2, B0410 during and after the Arch Pour

The occurrence of the five phases during the arch pour is demonstrated graphically by Figure 4-26. The temperature changes captured by the remaining thermistors were similar to what recorded by T2. Since the hydration development was not almost affected by the ambient temperature, the hydration curves were similar to what might be expected under adiabatic conditions. The maximum temperature rise (around 100 ºF) was captured by T4 at sec. (D-D), while the minimum temperature increase (around 41 ºF) occurred close to the beam end (T10). Though it was expected that the concrete close to the end would experience the highest temperature rise due to the relatively large amount of concrete in the chimney, the low temperature rise at the beam ends may be attributed to the large number of the tendons tied the concrete arches. These tendons might work as temperature sink that reduced the concrete temperature at the beam end. Figure 4-25 illustrates that, the temperature of the strands during the 24 hours was maximal at the beam ends and decreased as we move toward the midspan. These results support the conclusion that the strands absorbed the concrete temperature at the beam end. Moreover, the holes drilled at the chimneys, quarter points, and midspan, to allow casting the concrete, might slightly reduce the concrete temperature at these locations relative to the temperature at sec. (D-D).

The maximum temperature rise (100 ºF) matches the ACI Committee 363 (1992) suggestion that the temperature rise during hydration for high-strength concretes ranges from 11 to 15 ºF per 100 lb/yd^3 of cement.

Figure 4-27 shows the strain data recorded at the midspan of HCB2 during and after the concrete pour. The strain increased gradually at all the gauges up to the end of the concrete pour. By the end of the cast, the strain at FRP8 is found about three times the strain at FRP1 suggesting that the NA located about one-fourth the depth of the shell from the beam lower fiber. This is expected, because with the absence of the compression reinforcement, the tension reinforcement significantly moves the NA downward. Once the pour ended, the strain remained almost constant for several hours. As the concrete temperature began to rise at the top of the beam (sec. A-A), tensile strains induced at the upper fibers, while compressive ones took place at the lower fibers. The magnitudes of the induced strains due to the thermal effects seem to be compatible with the NA location at this stage. When the concrete started to cool, reversed strains induced in the shell elements.

The concrete is known to go through a phase of expansion during the plastic state followed by a phase of drying shrinkage during the hardened state. Subsequently, the strains induced in the FRP shell and strands, after the concrete pour, are expected to result not only

from the thermal effects, but also from the concrete volumetric changes due to the physical and chemical reactions of the concrete with its internal and external environment.

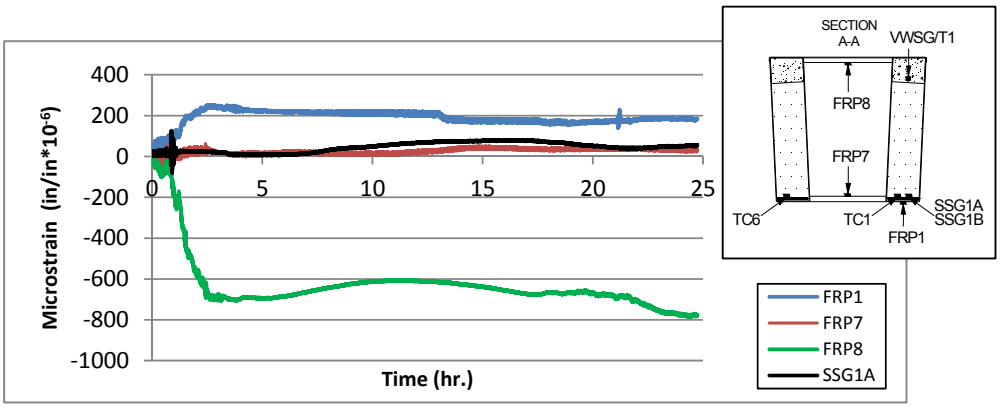

Figure 4-27 The Strains Induced in the Strands and FRP Shell at sec. (A-A) of HCB2, B0410, during and After the Arch Pour

Figure 4-27 clarifies that there is no strain compatibility between the strands and the bottom FRP shell (SSG1A & FRP1), unlike to what was expected. This indicates that, in spite of the simultaneous infusion with resin, the two elements separated allowing each element to suffer different levels of stress. The figure also demonstrates that the maximum normal strain occurred during the concrete pour (FRP8) was about 7% of the ultimate compressive strain (0.012 in/in). While the maximum tensile strain was less than 1% of the ultimate tensile strain (0.026 in/in).

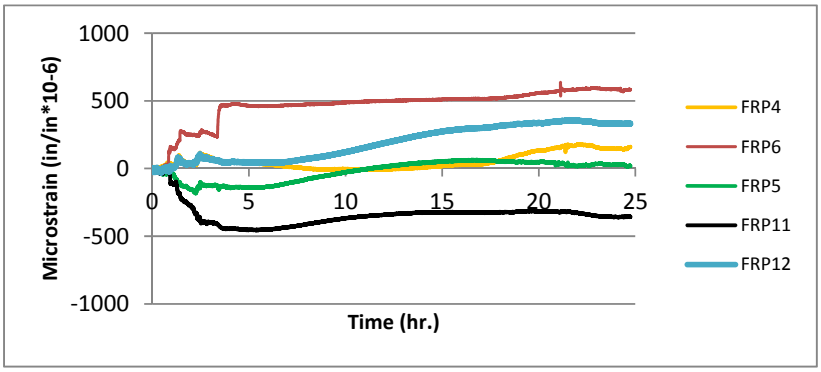

Figure 4-28 B0410 Shear Strain during and after the Arch Pour

Figure 4-28 displays the shear strains induced in the FRP shell due to the concrete pour. Gauge FRP 6, which is located at distance 2'-6" (half the shell depth) from the centerline of the support, captured the highest shear strain. Gauges FRP 4 and 5 were adhered

on the exterior shell, while gauges FRP 11 and 12 were placed at the same locations as FRP 4 and 5 but on the interior shell of the girder. However, the exterior gauges (4 & 5) read lower strains than those read by the interior ones (11 & 12) rather than similar strains as expected. This behavior is unexplained; however, the exterior webs suffered slight outward deformation (buckling) during the concrete pour which might affected the exterior gauges readings.

The maximum shear strain captured after the concrete pour was about 600 $\mu\varepsilon$ with corresponding shear stress equals about 35% of the ultimate shear strength (3.3 ksi). These results indicate that the shear and wrinkling of the shell webs are the most critical criteria during the design of the shell. It should be noted that the stress corresponding to the shear strain was calculated via multiplying the shear strain by the shear modulus. In other words, the FRP was assumed isotropic and neither the Poisson's ratio nor the coupling effects were included in that calculation.

4.9. SUMMARY AND CONCLUSIONS

A QC/QA testing program was implemented on the HCBs of the three bridges. The program included a theoretical study for the potential damage modes for the HCB members, and an assessment of the available inspection technologies. Potential damage modes for the HCB include voids or lack of consolidation in the arch, damage of the HCB composite shell, and corrosion damage of the prestressing strands.

The experimental QC/QA program started with a fabrication of a mockup beam simulating B0439 HCBs to verify the flowability of the SCC through the constricted arch cavity. The beam provided visual verification that the SCC would flow properly around the shear connectors located throughout the arch. The program included performing standard compressive tests on the SCC used to form the arches. The tests demonstrated that the arches of the three bridges gained compressive strengths that are significantly higher than the target strength of 6000 psi. Standard tensile tests were also implemented on FRP specimens taken from a shell web of B0439. The results of these tests, which will be presented in chapter 7, verified also the properties provided by the manufacturer. Concrete arches of B0439 and B0410 were instrumented with thermocouples to record their cure temperature. The measured values were indicative of the strength development in the arches and consistent with the well-established exothermic process of the Portland cement hydration.

Though the mockup beam demonstrated that the SCC can flow properly through the arch cavity, voids took place in the concrete arches of the a double-web HCB of B0410. The

voids were determined to be due to decreased flow ability in the concrete at the time of the pour. Methods for implementing thermal images to address the voids in the concrete arch were developed, tested and verified during the course of the testing. This technology successfully detected voids in the arch section during the casting of the arch for bridge B0410. The approach developed was innovative and capitalized on the heat of hydration generated during the curing of the concrete. As such, IR imaging is an ideal solution for QC/QA of the concrete arch concrete placement.

Damage modes for the HCB composite shell are generally available for visual inspection, and as, NDE technologies for this application were not pursued. However, the thermal methods used for assessing consolidation of the concrete arch are suitable for detection of delamination in the composite material, and this technology can be applied as a QC/QA tool to assess the workmanship of the composite construction. The damage mode of corrosion damage for the prestressing strands has limited available NDE technologies to detect and assess such damage. Experimental methods based on magnetic flux leakage were described in this chapter. This technology is experimental at this time, and generally not available for practical bridge inspections.

5. FIELD TESTING AND FINITE ELEMENT MODELING OF HCB

5.1. GENERAL

As it is clarified by the literature, only a very limited number of research studies have been conducted on HCB. The experimental results of these studies demonstrate that HCB's behavior has not been completely understood. HCB was thought to behave like a tied arch beam. While testing the first HCB-prototype, however, Hillman (2003) concluded that the HCB behaves like a beam element rather than a tied arch. Hillman (2003) also found that, when the actuator load exceeded certain limit, the HCB behaved in a manner similar to a tied arch. He suggested that, at high loads, a redundant load path was created, and the load was distributed from the FRP webs to the compression and tension reinforcement. The results of the study performed by Virginia Tech on the HCB, demonstrated that, under some load cases, the concrete above the neutral axis was subjected to tensile stresses (where compressive stresses were expected to exist) (Ahsan, 2012). The concrete arch was also found to suffer high compressive stress close to the junction with the chimney. At this location, the concrete was very close to the neutral axis and was supposed to have very small stresses. As it is mentioned in the literature, the study concluded that Hillman's model is inaccurate in estimating the strains and consequently the stresses in the concrete arch (Ahsan, 2012, Nosdall, 2013).

Diagnostic load tests were performed on the three bridges, to test their static responses under different load cases. Due to the uncertain behavior of the HCB, finite element models (FEM)s for B0439 superstructure were constructed to provide a better understanding of the HCB's behavior. The models were constructed via the commercial finite element analysis (FEA) packages; ANSYS V13 and SAP2000 V14.2.

The FEA of the HCB bridge is unconventional due to the novelty of the HCB, its unique configuration and its hybrid nature. It was, therefore, the main goals of the FEA of B0439 to: examine the accuracy of finite element analysis to predict the static performance of the HCB under service loads, establish a methodology for applying finite element modeling to the HCB, provide a better understanding for the HCB structural behavior, and emphasize the areas that need more research and examination.

During this chapter, the field load tests that were applied to B0439 and B0478 are explained, while the load testing of B0410 is presented in the next chapter. The finite element modeling of B0439 is detailed. The existing design procedure that is based on the

transformed area method is also used to predict B0439 HCBs' deflections. The measured deflections are compared to the estimated ones, and then the FEMs are used to analyze the HCB's static behavior.

5.2. LOAD TESTING OF BRIDGE 0439

A load test of B0439 was conducted by a research team from Missouri University of Science and Technology (MS&T) on March 26, 2012. A Leica total station and 19 prisms were used to measure the deflection along each girder. An additional three prisms were used as control points to ensure the total station did not move during the testing. One of these points was located along the top of the barrier over the abutment and will serve as a reference for comparison with future load tests. The load test trucks, prisms, and total station are shown in Figure 5-1.

Figure 5-1 Load Test of Bridge B0439; MoDOT Trucks (Left Image);
Total station and prisms (Right Image)

Two Missouri Department of Transportation (MoDOT) three-axle trucks were used to perform three stops, simulating three different load cases on the first span of the bridge. The front tire load (p1) from the first truck (T-6732) was 6.9 metric tons (15.2 kips) and the rear axle load (P2) was 15.9 metric tons (35 kips); the front load (P1) from the second truck (T-7627) equaled 7 metric tons (15.5 kips) and the rear load (P2) equaled 14.6 metric tons (32.2 kips). The truck stops, distribution of the rear tires load and the trucks configuration are all displayed in Figure 5-2.

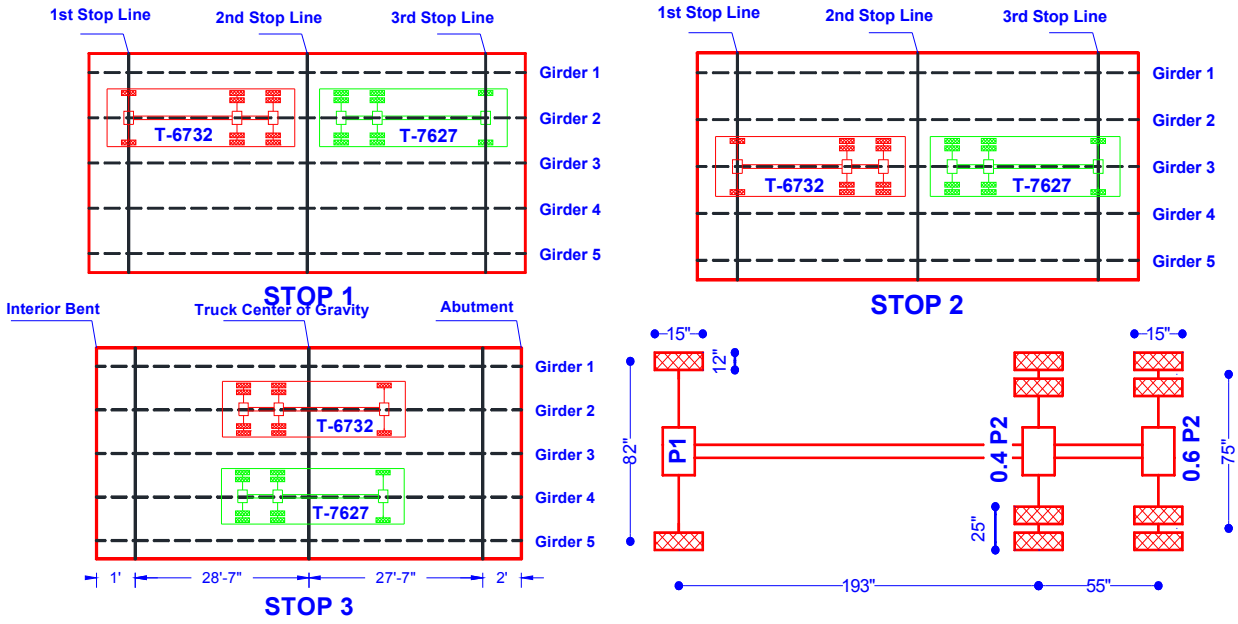

Figure 5-2 Truck Stop Locations, distribution of tire loads, and Truck Dimensions

5.3. FINITE ELEMENT MODELING OF BRIDGE B0439

Two FEMs were constructed to model the superstructure of the bridge B0439. A FEM with a very fine mesh was constructed using ANSYS V13.0. This FEM consisted of a total 75032 elements and 54698 nodes. In this model the gravity direction was presented by Y-axis, the longitudinal direction of the bridge was presented by X-axis and the transverse (lateral) direction was presented by Z-axis. The second FEM has a coarse mesh relative to the first one and was constructed via SAP2000 V14.2. The FEM consisted of 13595 elements and 10896 nodes. In the SAP model the gravity direction was presented by Z-axis, the longitudinal direction was presented by X-axis and the transverse direction was presented by Y-axis. The number of elements in both models was selected based on convergence study that is explained later. Figures Figure 5-3 and Figure 5-4 display the two FEMs constructed by SAP2000 and ANSYS software respectively.

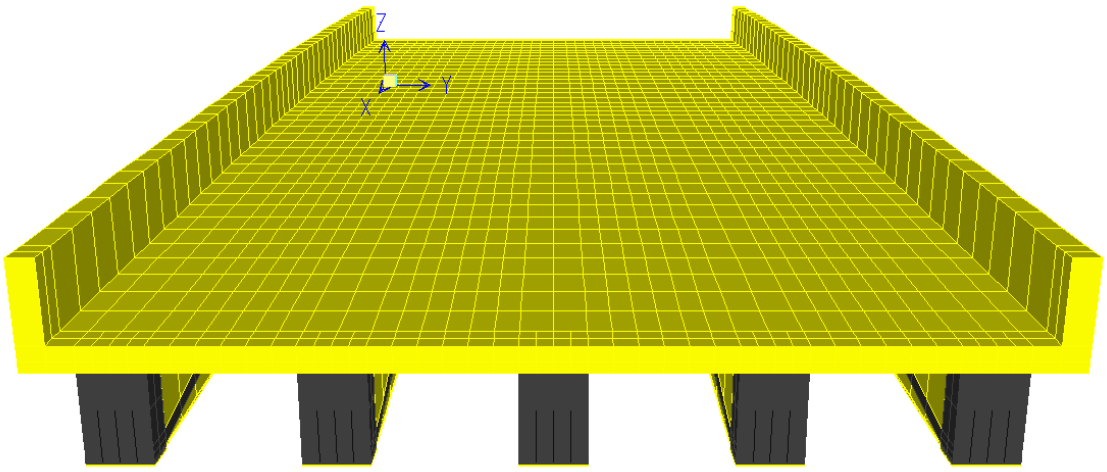

Figure 5-3 Finite Element Modeling of B0439 Superstructure by SAP2000 V14.2

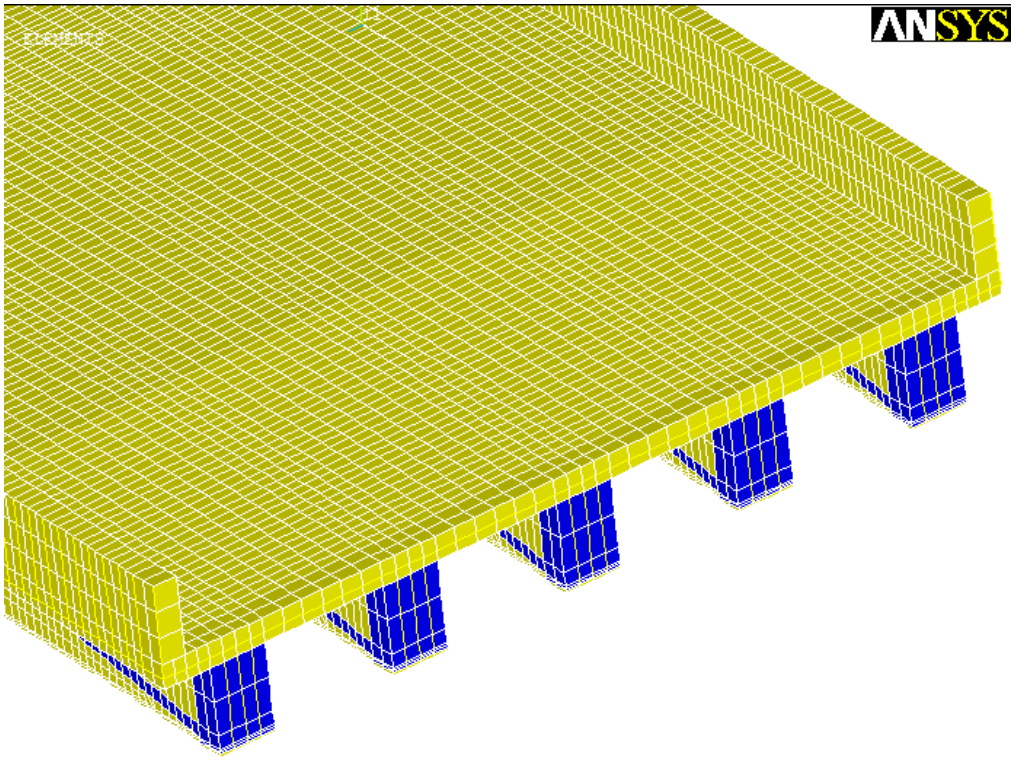

Figure 5-4 Finite Element Modeling of B0439 Superstructure by ANSYS V13.0

The maximum deflection measured during the load test of B0439 was found to be 0.0508-in. and occurred due to stop 3. This very small value indicated that there is no need to perform nonlinear geometric analysis and gave an indication that all the materials may

behave within its linear elastic range. Consequently, the first FEA trial, represented all the materials as linear elastic in the two models. The results obtained from the FEMs prove that the linear behavior assumption is valid.

5.3.1. Material Properties

5.3.1.1 FRP Composites

FRP composites are anisotropic materials. that is, their properties are not the same in all directions. The unidirectional lamina that has fibers oriented only in one direction possess three orthogonal planes of material symmetry. It is so-called especially orthotropic material where the fiber direction is the same as one of the global directions (Gibson, 2011). The relation between the stress tensor $\{\sigma\}$ and the strain tensor $\{\varepsilon\}$ of an orthotropic material can be given by:

$$\begin{Bmatrix} \varepsilon_{xx} \\ \varepsilon_{yy} \\ \varepsilon_{zz} \\ \gamma_{xy} \\ \gamma_{xz} \\ \gamma_{yz} \end{Bmatrix} = \begin{bmatrix} \frac{1}{E_x} & -\frac{\vartheta_{yx}}{E_y} & -\frac{\vartheta_{zx}}{E_z} & 0 & 0 & 0 \\ -\frac{\vartheta_{xy}}{E_x} & \frac{1}{E_y} & -\frac{\vartheta_{zy}}{E_z} & 0 & 0 & 0 \\ -\frac{\vartheta_{xz}}{E_x} & -\frac{\vartheta_{yz}}{E_y} & \frac{1}{E_z} & 0 & 0 & 0 \\ 0 & 0 & 0 & \frac{1}{G_{xy}} & 0 & 0 \\ 0 & 0 & 0 & 0 & \frac{1}{G_{xz}} & 0 \\ 0 & 0 & 0 & 0 & 0 & \frac{1}{G_{yz}} \end{bmatrix} \begin{Bmatrix} \sigma_{xx} \\ \sigma_{yy} \\ \sigma_{zz} \\ \tau_{xy} \\ \tau_{xz} \\ \tau_{yz} \end{Bmatrix} \tag{5.1}$$

where ε_{ii} is the strain in the direction i, γ_{ij} is the shear strain in the plane ij, σ_{ii} is the normal stress in the direction i, τ_{ij} is the shear stress in the plane ij, E_i is the young's modulus in the direction i, G_{ij} is the shear modulus in the plane ij, ϑ_{ij} is the possion's ratio (the ratio of strain in the j direction to strain in the i direction when the applied stress in the i direction), i,j = x, y, z and i≠j. Equation (5.1) can be rewritten as:

$$\{\varepsilon\} = [S]\{\sigma\} \tag{5.2}$$

where [S] is the compliance matrix, and the S_{ij} coefficients are given by equation (5.1).

Most of the unidirectional laminate for structural applications have fibers with a circular cross-section and hence can be assumed as orthotropic transversely isotropic because the properties of these composites are almost the same in any direction perpendicular to the fibers. For orthotropic transversely isotropic materials, the strain tensor can be related to the stress tensor via the compliance matrix as follow (Lubarda & Chen, 2008).

$$\begin{Bmatrix} \varepsilon_{xx} \\ \varepsilon_{yy} \\ \varepsilon_{zz} \\ \gamma_{xy} \\ \gamma_{xz} \\ \gamma_{yz} \end{Bmatrix} = \begin{bmatrix} S_{11} & S_{12} & S_{12} & 0 & 0 & 0 \\ S_{12} & S_{22} & S_{23} & 0 & 0 & 0 \\ S_{12} & S_{23} & S_{22} & 0 & 0 & 0 \\ 0 & 0 & 0 & S_{44} & 0 & 0 \\ 0 & 0 & 0 & 0 & S_{44} & 0 \\ 0 & 0 & 0 & 0 & 0 & 2(S_{11}-S_{12}) \end{bmatrix} \begin{Bmatrix} \sigma_{xx} \\ \sigma_{yy} \\ \sigma_{zz} \\ \tau_{xy} \\ \tau_{xz} \\ \tau_{yz} \end{Bmatrix} \tag{5.3}$$

In equation (5.3), the axis of isotropy is along the X-direction (direction of fibers in case of unidirectional laminates). Equation (5.3) indicates that $E_y = E_z$, $\vartheta_{xy} = \vartheta_{xz}$, $\vartheta_{yz} = \vartheta_{zy}$, $G_{xy} = G_{xz}$, $G_{yz} = \frac{E_y}{2(1+\vartheta_{yz})}$, and hence reducing the number of independent elastic constants from 9 in case of orthotropic materials to 5 in case of orthotropic transversely isotropic materials.

On the other hand the multidirectional fabrics begin to behave somewhat "quasi-isotropic", consequently theses composites can be assumed to have isotropic properties to simplify preliminary designs. As was mentioned in section 2.5.2, the standard laminate composition of the HCB FRP shell is typically a woven glass reinforcing fabric infused with a vinylester resin matrix. The woven fabrics used in the FRP shell of bridge B0439 are comprised of two multidirectional plies. The multidirectional fabrics can be assumed to have isotropic properties to simplify preliminary designs. However for more accurate modeling of the shell, it is assumed orthotropic transversely isotropic. Experimental tests were performed by the manufacturer to the FRP webs at the macroscopic level to determine the elastic constants of the laminate. The experimental tests identified the tensile and compressive in-plane moduli of elasticity (E_x^+ , E_x^- ,E_y^+ ,E_y^-), the in-plane shear modulus (G_{xy}), the effective longitudinal compressive and tensile strengths (S_L^-, S_L^+ respectively), effective transverese compressive and tensile strengths (S_T^-, S_T^+ respectively), and the effective shear strength (S_{LT}).

The test results enable the calculation of only three elastic constants, in order to calculate the remaining two constants, ϑ_{xy} is assumed 0.26 and ϑ_{yz} is assumed 0.30 (Kachlakev et al., 2001). A summary for material properties used for modeling the FRP shell is listed in Table 5-1.

Table 5-1 Material Properties Used for Modeling the FRP Shell

	Effective Strength (ksi)	Elastic Modulus (ksi)	Poisson's Ratio	Shear Modulus (ksi)
Tensile properties	$S_L^+ = 54$	$E_x^+ = 3998$	$\vartheta_{xy} = 0.26$	$G_{xy} = 919$
	$S_T^+ = 18$	$E_y^+ = 2277$	$\vartheta_{xz} = 0.26$	$G_{xz} = 919$
	$S_{LT} = 3$	$E_z^+ = 2277$	$\vartheta_{yz} = 0.3$	$G_{yz} = 876$
Compressive properties	$S_L^- = 20$	$E_x^- = 1254$	$\vartheta_{xy} = 0.26$	$G_{xy} = 919$
	$S_T^- = 22$	$E_y^- = 1378$	$\vartheta_{xz} = 0.26$	$G_{xz} = 919$
	$S_{LT} = 3$	$E_z^- = 1378$	$\vartheta_{yz} = 0.3$	$G_{yz} = 530$
Density Ib/ft^3	$\rho = 105$			

5.3.1.2 Concrete

Concrete is a quasi-brittle material with different compression and tension behaviors. In compression, the stress-strain relation is linearly elastic up to 30% of the maximum compressive strength (Kachlakev et al., 2001). In tension, the stress-strain curve is approximately linearly elastic up to the maximum tensile strength. However, the tensile and the compressive moduli of elasticity are almost the same in the elastic linear range. In B0439, self-consolidating concrete (SCC) is used to form the compression reinforcement of the HCB.

Domone (2007) analyzed the data from more than 70 recent studies on the hardened mechanical properties of SCC to produce comparisons with the properties of equivalent strength normally vibrated concrete (NVC). Domone concluded that the design rules and practice for NVC developed over many decades can be used for structures cast with SCC. He also found that the elastic modulus of SCC can be significantly lower than of NVC at low compressive strengths. Based on Domone (2007) study, the elastic modulus and the maximum tensile strength are calculated via the following ACI 318-11 (2011) equations:

$$E_c = 57000\sqrt{f'_c} \text{ (ASE)} \quad (5.4)$$

$$f_r = 7.5\sqrt{f'_c} \quad \text{(ASE)} \quad (5.5)$$

where f_c' is the compressive strength of concrete, f_r is the modulus of rupture of concrete and E_c is the elastic modulus. In equations 2 and 3, f_c', f_r and E_c are in psi.

5.3.1.3 Steel Reinforcement

Two types of reinforcement bars were used in B0439. Typical steel reinforcing bars were used in the deck, while seven wires, conventional prestressed concrete strands (Grade 270) were used in the HCBs. Both types were assumed to have identical behavior in tension and compression. The high strength tendons were assumed to have young's modulus equals 28,500 ksi, while the typical steel bars were assumed to have young's modulus equals 29,000 ksi. The two types were assumed to have 0.3 Poisson's ratio and 490 lb/ft^3 density.

5.3.1.4 Polyisocyanurate Foam

Polyiso foam is a 2.0 lb/ft^3, rigid, closed cell foam supplied as blocks with 24-in. width. The tensile and compressive elastic moduli and shear moduli are provided by the manufacturer in the longitudinal and perpendicular directions. In this study, the foam is assumed to behave as orthotropic transversely isotropic material. Poisson's ratios ϑ_{yz} were calculated based on the provided moduli, while ϑ_{xy} and ϑ_{xz} are assumed to be 0.33 (Friis et al., 1988). A summary for material properties used for modeling the polyiso foam is listed in Table 2.

Table 5-2 Material Properties Used for Modeling the Polyisocyanurate Foam

	Elastic Modulus psi	Poisson's ratio	Shear Modulus psi
Tensile properties	$E_x^+ = 1225$	$\vartheta_{xy} = 0.33$	$G_{xy} = 220$
	$E_y^+ = 463$	$\vartheta_{xz} = 0.33$	$G_{xz} = 220$
	$E_z^+ = 463$	$\vartheta_{yz} = 0.308$	$G_{yz} = 177$
Compressive properties	$E_x^- = 700$	$\vartheta_{xy} = 0.33$	$G_{xy} = 220$
	$E_y^- = 434$	$\vartheta_{xz} = 0.33$	$G_{xz} = 220$
	$E_z^- = 434$	$\vartheta_{yz} = 0.226$	$G_{yz} = 177$

5.3.2. Element Types and Model Simplifications

5.3.2.1 Hybrid Composite Beam (HCB)

Because the HCB's GFRP shell has a very small thickness relative to its length and width, it was modeled using two-dimensional space elements: shell181 element in ANSYS and traditional shell element in SAP2000. Both elements are four-node elements with six degrees of freedom (DOFs) at each node. Shell 181 element in ANSYS is based on the first-order shear deformation theory. In SAP2000 model, thick-plate formulation was selected for the traditional shell element. This formulation was selected because it includes the effects of transverse shearing deformation. The compressive FRP properties were assigned to FRP webs and upper flange elements while the tensile FRP properties were assigned to the lower flange elements. The concrete web was also modeled using shell181 element in ANSYS and traditional shell element in SAP2000.

The concrete arch was modeled using solid65 element in ANSYS and traditional solid element in SAP2000. The polyiso foam was modeled using solid185 element in ANSYS and traditional solid element in SAP2000. Solid elements in both models are defined by eight nodes, each node has three translational DOFs. Foam tensile properties were assigned to the elements below the concrete arch, while the compressive properties were assigned to the elements above the concrete arch. For the upper and lower foam, axis of isotropy was taken along the gravity direction (Y-dir. in ANSYS and Z-dir. in SAP2000).

The HCB strands were modeled using beam188 element in ANSYS and traditional beam element in SAP2000. The tension reinforcement lies directly on the lower FRP flange. Previous experimental tests performed by Snape and Lindyberg (2009) showed that, due to the simultaneous infusion with resin, there is perfect bond between the strands and the lower flange resulting in the strands reinforcing the bottom flange. However, the experimental test executed on B0410 during the arch pour showed a significant difference in the strains of the two elements, indicating that they have indicated slip/separation from each other (sec.4.8) Consequently, it was assumed, conservatively, that the bridge under study has a similar behavior to B0410. Since the strands were modeled using one-dimensional space elements in both models, if they are modeled directly on the lower flange, the flange will behave as if it is reinforced with these strands. In order to achieve the strain incompatibility assumption between the two components, the strands were modeled in two layers separated from the lower flange and from each other with 0.5-in. Modeling the 36 strands via 36 separate beam elements would complicate the meshing; consequently, the 36 strands were represented by 6

beam elements, 3 per each layer. The total cross-sectional area of the 6 beam elements is equal to the area of the 36 strands.

Based on experimental testing, it is found that the shell webs are stiffened by a resin bond to both the concrete arch and polyiso foam (Hillman, 2003). This bond allows the webs to reach the allowable shear strength of the GFRP within the service load limits without suffering elastic buckling. It is, therefore, acceptable to assume perfect bond between the shell webs with the compression reinforcement and the polyiso foam. Generally, a perfect bond between all the components of the HCB was assumed in the FEA of B0439. This was achieved in the two FEMs by maintaining the same mesh for all the constituents. Maintaining the same mesh guaranteed that the joints of any component coincide with the joints of other components that are in intimate contact with this component, consequently achieving the assumption of the perfect bond. The HCBs of bridge B0439 were manufactured with an initial 5.25-in. camber to equilibrate the downward deflection of the beams when subjected to the full dead loads. This camber was presented in the FEMs. Figure 2-3 displays the finite element modeling of HCB using SAP2000.

5.3.2.2 Bridge Deck

The bridge slab was modeled using solid65 element in ANSYS and traditional solid element in SAP2000. Two solid elements were used throughout the slab depth, to allow modeling of the reinforcement bars. The reinforcement bars in longitudinal and transverse directions were modeled using beam elements in both models. The parapet was poured simultaneously with the slab, and its reinforcement extended in the deck. A previous study by Myers et al. (2008) showed that when a composite action is achieved between the slab and the parapet, the deflection is significantly decreased. Consequently, the parapet was included in the FEMs and simulated using solid65 element and traditional solid element in the ANSYS and SAP2000 respectively. Although, some states do not allow taking into consideration the contribution of the parapet to the stiffness of the bridge superstructure, representing the parapet in the FEMs aimed to simulate the actual behavior of the bridge superstructure and allow realistic comparison between the measured and predicted data. A previous study (Hillman, 2008) proved that the shear connectors of the HCB achieve full composite action between the bridge deck and the HCBs. In the FEA, a perfect bond is assumed between the deck components and between the deck and the HCBs. Figure 5-5 illustrates modeling of B0439 superstructure in ANSYS.

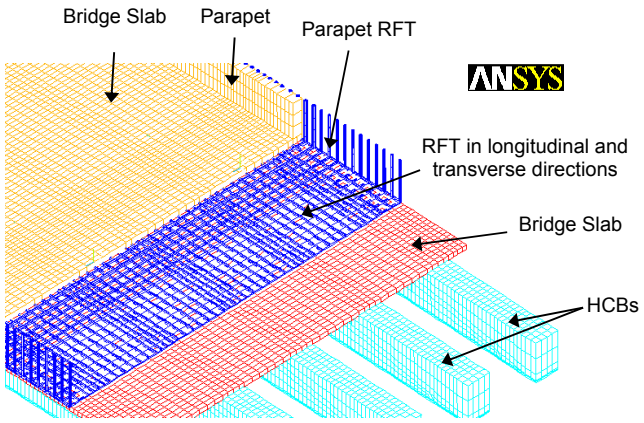

Figure 5-5 Modeling of the Bridge Deck and the HCBs in ANSYS

5.3.3. Load Modeling

A time dependent analysis was performed to account for the stress history of the HCBs resulting from casting the concrete arch and the bridge slab in addition to the dead and live loads. The time dependent analysis was performed through three stages:

Stage 1: In this stage, the permanent stresses induced in the strands and the GFRP shell, due to pouring the concrete arch, were calculated. Consequently, the HCB was modeled without the concrete arch and web. The self-weight of the HCB components were included in the analysis, while the weight of the concrete arch and web were applied as distributed load on the upper face of the lower foam elements (the foam below the concrete arch). Neither the dynamic effects nor the lateral stresses that may occur during pumping the concrete were included in the analysis because these stresses were considered to be temporary.

Stage 2: As it was explained in sec. (3.2.2), B0439 incorporated the use of precast stay-in-place deck forms to expedite the construction process. Consequently, the deck was not shored during the construction. This stage calculated the stresses induced in the complete HCB due to casting the bridge slab and barriers. This was achieved by applying the weight of the bridge slab and barriers as uniform distributed load on the upper FRP shell elements. The self-weight of the HCB components was not included in this stage, since it was considered in the first stage.

Stage 3: In this stage, complete models for B0439 superstructure were constructed. Only the wearing surface weight, which was assumed 1-in., and the truck loads were applied on the composite section. Both the dead and live loads were applied as uniform pressure on the upper surface of the slab elements. The tire loads were modeled as distributed loads instead of point loads, because using 3D elements is non-consistent with the concentrated loads.

When applied to 3D elements, the concentrated loads may result in a stress singularity, as the element size become smaller and smaller as the stress increases and tends to infinity, hence mesh convergence cannot be achieved.

Finally, linear superposition was performed between the three stages to obtain the total stresses induced in the different constituents of the HCBs. The principle of the superposition was used because the HCBs did not undergo large deformations in all the three stages and the different materials were found to behave within their linear elastic ranges. Moreover, the total maximum stresses obtained from the time dependent analysis, which will be presented later, were found within the elastic ranges of all the materials.

5.3.4. Boundary Conditions

Each end of the HCBs of B0439 is supported on a steel-laminated neoprene bearing pad with plan dimensions of 8-in. by 1 ft-10-in. Generally, the elastomeric bearing pads are designed to allow horizontal deformations of the beams due to thermal changes, applied loads and time-dependent concrete changes. For that reason, it is common to model bridge girders as simply supported beams that have a pin support at one end and a roller support at the other end. However many researches proved that the actual bridges are stiffer than their theoretical models due to neglecting the restrained forces at the beam-pad interface. Tests on twenty six bridges in Canada proved that bridges are generally stiffer than theoretical assumptions (Yazdani et al., 2000). Yazdani et al (2000) predicted translational and rotational stiffness values that can simulate the bearing restraint effect. The predicted stiffnesses were found to be very close to the calculated stiffnesses based on AASHTO specifications (1996). However, when Yazdani et al (2000) used the calculated stiffnesses during finite element modeling of prestressed I-beam bridge in Florida, USA, the maximum deflection and tensile strain at mid span were found to be significantly larger than the measured values. Even when the bearing pad was assumed to have shear modulus equals 25 times the maximum shear modulus that is required by the AASHTO specifications to simulate the effect of aging and cold, the maximum deflection and maximum tensile strain were found to be higher than the field test data by about 19% and 25% respectively.

Based on the previous studies, it is thought that modeling the HCB using pin supports at each end may provide more realistic predictions for the deflections. Consequently, pin supports were applied to the lower flanges at the locations of the bearing pads. Due to the continuity of the bridge slab, the edge of the slab over the interior bent was restrained from

translation and rotation in all directions. While over the abutment, the edge of the slab was restrained from translation in all direction.

The bridge incorporated the use of concrete diaphragms that span between the HCBs ends and rested directly on the interior and exterior bents. These diaphragms were simulated by applying supports that restrain the lateral translation of the HCBs at the contact areas between the diaphragms and the beams.

5.3.5. Convergence Study

An important step in the FEA is the selection of the mesh density. The elements should be discretized such that a convergence of results is obtained. The minimum number of elements that can be used to model accurately a structure is the number after which the increase of mesh density leads to insignificant change in the results. In the current study a simple convergence study was carried out to determine the appropriate mesh density using only the concrete arch of the HCB. The boundary conditions that were described in the previous section were used in the convergence study. The compression reinforcement including the chimneys were modeled in ANSYS V13.0 with increasing number of elements: 128, 208, 416, 736 elements. Five response parameters were used to test the convergence of results. These parameters are: the deflection at midspan of the arch, the stress at the bottom fiber of the arch midspan, the stress at the top fiber of the arch midspan, the maximum compressive stress in the chimney, and the maximum tensile stress in the chimney. The results of this study are illustrated in figures Figure 5-6 and Figure 5-7.

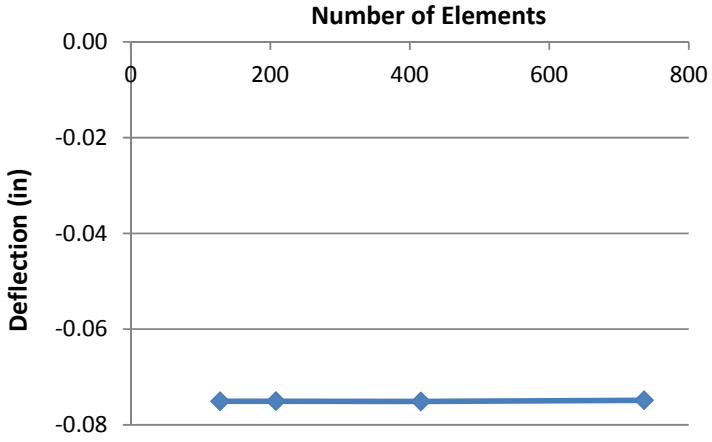

Figure 5-6 Deflection of HCB parabolic arch (Convergence Study)

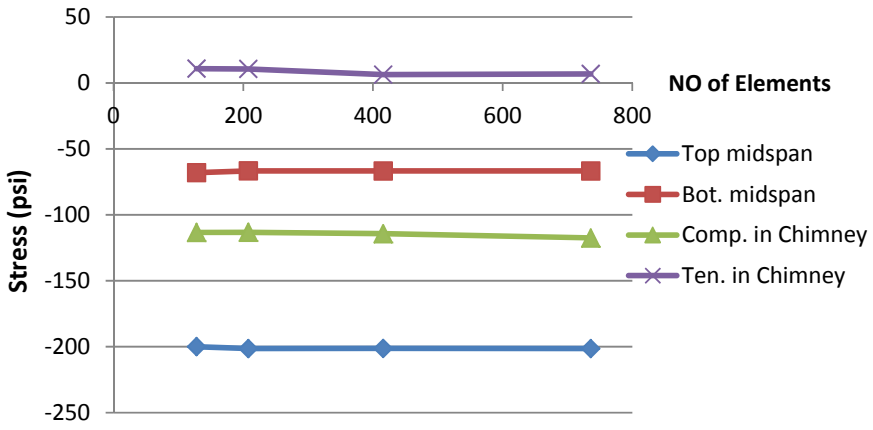

Figure 5-7 Stress at different locations in the arch (Convergence Study)

The results demonstrate that the convergence of results was achieved via all the proposed mesh densities. However, since the study included only the compression reinforcement of the HCB, two different meshes were used in the two FEMs to assure the result obtained from this study. In the SAP2000 model the concrete arch was modeled with 128 elements and the remaining HCB constituents and the deck components were modeled with the same mesh density to achieve the perfect bond assumption between all the components. This resulted in a model with 13595 elements. In the ANSYS model the finest proposed mesh was used. The concrete arch was modeled with 736 elements resulting in a model with a total of 75032 elements.

5.4. MATHEMATICAL CALCULATIONS OF THE DEFLECTION

In order to calculate the deflection of the HCBs, the first step is to define the beam stiffness. In calculating the section properties of the HCB, two factors should be considered. The first factor is the different constitutive properties of the different materials used. Hillman's design methodology (Hillman, 2003, Hillman, 2012) uses the transformed area technique to transform the different constituents of the HCB to equivalent amounts of the GFRP of the webs. The other factor is the fact that the HCB sections are not prismatic along the length of the beam due to the parabolic profile of the concrete arch. As a result, Hillman's model calculates the section properties at $1/10^{th}$ points along the beam length. Hillman proposed that his model is sufficient only for simply supported structures under conventional live loads. The HCBs of B0439 are simply supported. However, the deck is continuous over the three spans. In this study, the efficiency of a mathematical algorithm, similar to Hillman's model, to detect the deflection in B0439 is tested.

Hillman's methodology accounts for the composite properties of the HCB with the concrete deck. However, the model ignores the foam, concrete web and the reinforcement bars of the deck during the calculations. In the present study, these components were included in the calculations and the section properties were calculated at $1/20^{th}$ points along the beam length.

The calculation of the beam stiffness starts with calculating the transformation factor, modular ratio, n_i

$$n_i = \frac{E_i}{E_w} \tag{5.6}$$

where E_w is the modulus of elasticity of the FRP web and E_i is the modulus of elasticity of the constituent i that need to converted to equivalent amount of GFRP.

Since the FEA validated that all the materials behave within their elastic range and that the concrete has not cracked, the moment of inertia at each section was calculated based on the elastic neutral axis (ENA) of the beam. The moment of inertia at each section can be determined as follows:

$$A_{tij}(x) = n_i \times A_{ij}(x) \tag{5.7}$$

$$\overline{y}_j(x) = \frac{\sum_{i=1}^{n} A_{tij}(x).y_{ij}(x)}{\sum_{i=1}^{n} A_{tij}(x)} \tag{5.8}$$

$$I_j(x) = \sum_{i=1}^{n}\left(I_{tij}(x) + A_{tij}(x)\left(y_{ij}(x) - \overline{y}_j(x) \right)^2 \right) \tag{5.9}$$

where $A_{ij}(x)$ is the cross-sectional area of the component i at the section j, $A_{tij}(x)$ is the transformed area of the component i at section j, $y_{ij}(x)$ is the distance from the c.g. of the componet i to the extreme lower fiber of the beam at the point j, $\bar{y}_j(x)$ is the distance from the ENA of the composite section to the extreme lower fiber of the beam at section j, $I_{tij}(x)$ is the transformed moment of inertia of the component i with respect to its c.g. at section j, $I_j(x)$ is

the moment of inertia of the composite section at section j, n is the total number of HCB components and j = 1,2,…, 21. In this work, a MATLAB code was constructed to calculate the stiffness of the HCB at each section.

The second step in calculating the deflection is identifying the load distribution factor for each girder due to the applied loads. In this study the lever rule provided by AASHTO LRFD (2012) was used to determine the load distribution factors for the exterior HCBs. While the load distribution factor, *g*, for the interior beams was determined by the following AASHTO LRFD (2012) equations:

$$g = \left(\frac{S}{3.0}\right)^{0.35}\left(\frac{Sd}{12.0L^2}\right)^{0.25} \quad \text{(ASE)} \tag{5.10}$$

$$g = \left(\frac{S}{6.3}\right)^{0.6}\left(\frac{Sd}{12.0L^2}\right)^{0.125} \quad \text{(ASE)} \tag{5.11}$$

where S is the spacing of the beams in feet, d is the depth of the beam in inch, and L is the span of beam in (ft.). Equation (5.10) was used when one lane was loaded, while equation (5.11) was used when two lanes were loaded. Equation (5.10) includes the multiple presence factor for loading one-lane, which is 1.2. Consequently, it was divided by 1.2 to allow realistic comparison with the applied loads.

Finally, the deflection was calculated by modeling each HCB in SAP2000 using 20 non-prismatic elements.

5.5. RESULTS DISCUSSION

A sample of the experimental measured deflections and the predicted deflections by the two FEMs and theoretical calculations is given in Figure 5-8. The deflection is measured and predicted at the quarter, mid and three quarter points of each girder span. Generally, the results demonstrate a good agreement between the two FEMs predictions and the field measured data and an excellent agreement between the two FEMs results. The differences between the measured data and the FEA predictions can be attributed to the common error sources such as the deviation of the real dimensions of the bridge elements from the dimensions provided by the drawings, FEM assumptions and simplifications, unknown material properties and experimental errors.

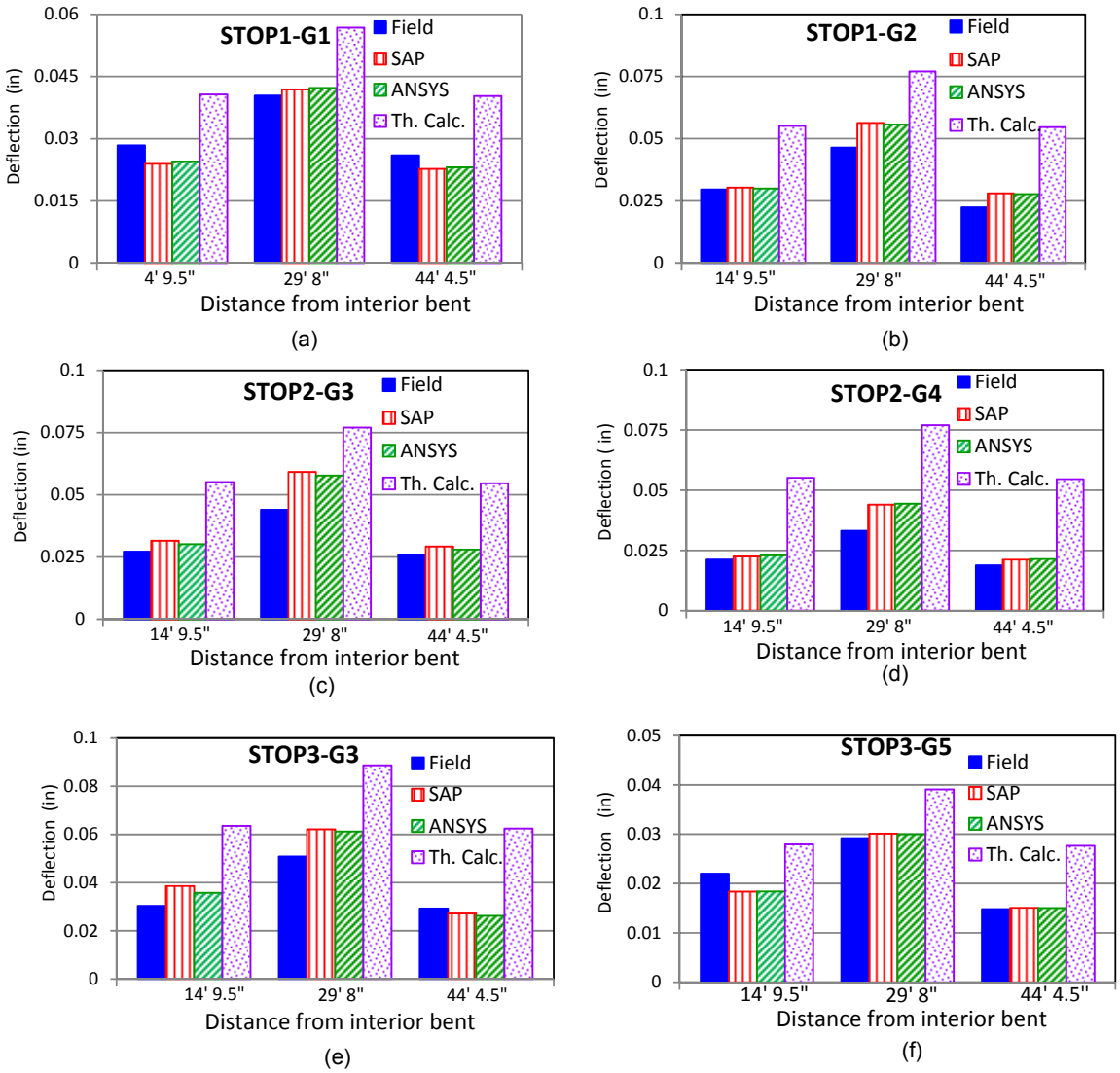

Figure 5-8 Comparison of the Bridge 0439 Deflections Measured at Field and Predicted by ANSYS, SAP2000 and Theoretical Calculations

In a previous study, Myers et al. (2008) found that, the experimental errors in bridges field tests led to the following deflection deviations: a transverse shift in the truck stop location by 12″ changed the deflection by 10%, a longitudinal shift in the truck stop location by 12″ changed the deflection by 5%, 5 kips error in truck weight reporting altered the deflection by 7%. They also concluded that the sensitivity of surveying equipment, total station, is ± 0.005-in. Some of these errors were incarnated in stop 2. As it is shown in Figure 5-2, the two trucks loads are symmetric about the longitudinal centerline of the bridge, consequently deflections were expected to be the same along girders 1 and 5, and girders 2 and 4. However, the experimental data showed that the average deflections through girder 2

(G2) are larger than those through G4 by an average value equals 28% and that the average difference between G1 and G5 measurements is 12%, which indicates that the two trucks shifted transversely toward G1 and G2.

Figure 5-8 clarifies that the two FEMs overestimated the deflection at the mid-span of the five girders in all the stops. In addition to the aforementioned error sources, the thermal changes effect might contribute to the overestimation of the mid-span deflection. The bottom surfaces of the HCBs are not only close to the river surface but also unexposed to sun's radiation, which might reduce their temperature. On the other hand, the deck is exposed to the sun during the daytime and can gain heat from the sun's radiation. This thermal ingredient causes upward deflection, consequently reducing the total deflection at mid-span. According to Radolli and Green (1975), the stresses induced through the depth of the structure due to diurnal cycles can exceed the live loading in some cases. Initial and final measurements were recorded by the total station for the bridge without the trucks loads at morning and afternoon respectively. The measurements showed that at the final no-load test the HCBs suffered negative deflections at all the prisms' locations with deflection equals -.009-in. at the mid-span of G3. This indicates that maximum deflection in the last stop was reduced by about 15%. However, since the temperatures of the different superstructure elements at the time of each load test were not measured, a correction for the thermal effects could not be performed. It was found that the average difference between the measured deflections and the ANSYS FEM results is 15.8% and the average difference between the field deflections and the SAP2000 FEM results is 16.5%. It was also found that the ANSYS FEM overestimated the maximum deflection observed during the load test of B0439, the mid-span deflection of G3 due to stop 3, by 21% while the SAP2000 FEM overestimated the maximum deflection by 22%. These results validate the modeling assumptions and simplifications and demonstrate that the linear FEA predicted the behavior of the hybrid composite superstructure of B0439 under the applied service loads with acceptable accuracy; hence, it can be used to analyze the HCB behavior.

The results presented in Figure 5-8 demonstrate that the theoretical calculation procedure highly overestimated the deflections in the three load cases. The theoretical method predicted higher deflections than those predicted by the FEA and consequently than the measured data for several reasons. First, the tire loads were distributed to all the bridge girders using the load distribution factors and the lever rule provided by AASHTO LRFD (2012) . The sum of the load distribution factors of the five girders is found to exceed 100% in all the stops. For example in stop 3, the sum of the load distribution factors is 1.1, which

means that the applied loads to the girders exceed the real ones by 10%. Second, the theoretical procedure ignores the effect of the parapet on the deflection. Similar to what was observed by Myers et al. (2008), it was found in this study that the parapet significantly reduces the deflections of the bridge girders. The effect of the parapet was found dependent on the load and girder locations. When the bridge was modeled by ANSYS without the parapets, it was found that due to stop 1 loads, G1 suffered deflections higher than the deflections of the original FEM by 59%. This difference reduced gradually as we moved inward until almost no difference was observed on the deflections of G4 due to removing the parapets from the model. In stop 3, it was found that after removing the parapets, the average deflections of G1 and G5 increased by about 49%, the average deflections of G2 and G4 increased by 15%, and the average deflections of G3 increased by 8%. Similar differences to those observed due to stop 3 were obtained due to stop 2 loads. These differences are based on the average deflection of the quarter, midspan and three quarter points, but the differences of the maximum deflections at the midspan points are higher than the mentioned values. Third, the HCB was simulated in the theoretical calculations by beam elements while it was modeled in the FEA by a combination of solid elements, shell elements and beam elements. Since the beam element is more flexible than the shell and solid elements, it is expected that the predicted deflections by the theoretical analysis will be higher than the actual ones. Finally, in the theoretical analysis, the continuity of the slab over the interior bent was not considered, while in the FEM, fixed supports are applied to the slab edge over the pier to account for deck continuity. Consequently, the mathematical procedure that is implemented in the current study can be used as a simple method for the preliminary design of the HCB in continuous structures. While for more accurate prediction of the HCB deflection in continuous structures, a sophisticated analysis is recommended. It is worth mentioning that the complex FEMs constructed in this study aim to predict the stresses in the different components of the HCB and analyze its structural behavior. However, the authors believe that simpler FEM can predict the deflection of the HCB in the continuous structures with acceptable accuracy.

Since the design of the HCB is stiffness-driven, a study was performed to examine the accuracy of the design/analysis of HCB in case of assuming isotropic properties for the FRP and polyiso foam. In this study, the FRP and foam were assumed isotropic materials with different moduli of elasticity in compression and tension equal to E_x^- and E_x^+ listed in Tables Table 5-1 and Table 5-2 respectively. The study illustrated that this simplification can result

in a deviation of the deflection calculations not more than 10% in stage 1, 7.5% in stage 2, and 5% in stage 3. These results validate that it is acceptable to assume isotropic behavior for the multidirectional FRP and polyiso foam to simplify preliminary design/analysis of the HCB.

5.6. STRUTURAL BEHAVIOR ANALYSIS

The stresses obtained by the two FEMs are similar to each other; however, the stresses obtained by the ANSYS model are found higher than those obtained by the SAP2000 model. This can be attributed to the difference in mesh densities between the both models. Since the ANSYS model has finer mesh, all stress results presented in the following sections are extracted from this model. The presented stresses of the different HCB components are the major stresses in the longitudinal direction of the beams (X-direction). These stresses are the stresses induced in G3 due to the total loading of the three stages with stop 3 loads included in the third stage, which was found to produce maximum stresses among the three stops. The maximum compressive stress induced in the concrete arch of G3 was found 14.2 2060 psi which is less than 30% of the compressive concrete strength of 10 ksi. Though tensile stresses induced at the concrete arch midspan due to stage 3 loads, the induced compressive stresses due to stage 2 loading led to subjecting the arch to pure compressive stresses under the applied service loads. The maximum stress in the tensile reinforcement of the HCB was found 5480 psi, which is much lower than the yield stress of the tendons. The maximum compressive stress in the lower FRP shell was 3980 psi and the maximum tensile stress was 1875 psi, which are much lower than the effective longitudinal tensile and compressive strengths of the GFRP given in Table 1. The stresses in the FRP upper flange and webs were found lower than the stresses in the lower flange, while the maximum shear stress in the FRP shell was 1300 psi. This occurred in the shell web as it is expected. About 80% of this stress occurred in stage 1, while after hardening of the concrete arch; significantly, lower shear stresses took place in the web. The stresses in the bridge deck were also found to be within the elastic range of the concrete and reinforcement bars. These values assured that all the materials behave within their linear elastic ranges and indicated that the total load due to the three stages loading are much lower than the capacity of the HCBs. The maximum measured deflection 0.05-in. due to stop 3 is much lower than the allowable live load deflection provided by the AASHTO LRFD (2012) of span length/800, which is 0.89-in. This is compatible with the stress indication that the applied load is much lower than the ultimate capacity of the HCBs.

A study was performed to compare between the HCB behavior under the actual truck loads used in the implemented load testing and the notional loads recommended by AASHTO LRFD (2102) for the optional live load deflection evaluation. The study started by identifying the design truck axel spacing, the trucks orientations in the longitudinal and transverse directions of the bridge, and the load case that produce maximum deflection. The results clarified that two design trucks with all axel spaced 14 ft-0-in. oriented symmetrically about G3 in the transverse direction produce maximum deflection in G3. The total load of one design truck, including the dynamic load allowance, is 95.8 kip, which is about twice the average load of the trucks used in the load test. However, the HCB was found to still behave within the elastic ranges of its constituents. The maximum tensile stress in the concrete arch due to the fictitious truck loads in addition to the second stage load was found 36 psi, which is much lower than the modulus of rupture of the concrete. This small stress indicates that the HCB can maintain the gross section properties under significantly higher loads than the notional loads provided by AASHTO LRFD (2012). The maximum deflection predicted by the ANSYS model due to the design trucks loads was found as 0.15-in. This deflection is also much lower than the allowable live load deflection provided by AASHTO LRFD (2012).

Figure 5-9 illustrates the locations of the maximum tensile and compressive stresses in the concrete arch of G3 due to the loads of stages 2 and 3. In stage 2, the maximum compressive stress took place close to the junction of the arch with the chimney. Since, the non-composite HCB is simply supported, according to the current design methodology by Hillman a small bending moment tends close to zero is supposed to occur at this location. Moreover, the location of the maximum compressive stress is below the ENA of the HCB. Consequently, a very small tensile stress is expected to take place at this location. This result is compatible with the literature (Ahsan, 2012) and contradicts the current design methodology. While in this stage, the maximum tensile stress is found to occur at the concrete web close to the junction of the concrete web with the chimney. These results indicate that, though the non-composite HCB is simply supported, negative bending moment might take place at the end of the beam. The maximum compressive stress in the concrete arch took place at the lower extreme fiber and was higher than the compressive stress at the extreme upper fiber of the arch at the same location. Moreover, the stress in the upper FRP flange at this location was found tension, while the stress in the lower FRP flange at this location was found negative. These results support that the moment at the end of the HCB is in fact negative. One explanation of this behavior is that, the chimney provides partial fixation to the beam resulting in negative moment at its end. In stage 3, the results also

indicated that there is negative moment at the end of the beam, while the maximum tensile stress occurred close to the midspan at the lower fiber of the arch. Figure 5-10 displays the stresses in the lower FRP flanges of all the girders due stage 3 loads. The compressive stresses are displayed with the grey color in the ANSYS model and with the purple color in the SAP model. Compressive stresses induced in the lower FRP flange in the three stages at the same locations as in Figure 5-10. It is clear from this figure that significant portions of the lower flanges are subjected to compressive stresses, while it is expected according to the current design methodology that all the lower flanges be subjected to tensile stresses only.

To verify these results a comprehensive study was performed in which the HCB was modeled individually and as a framing system in B0439. The HCB was modeled in each case with two boundary conditions; hinge-hinge and roller-hinge. Finally, the HCB was modeled individually with camber and without camber. In all the cases, the concrete arch and the lower FRP shell under different applied loads had stresses similar to what displayed in Figures 5-9 and 5-10.

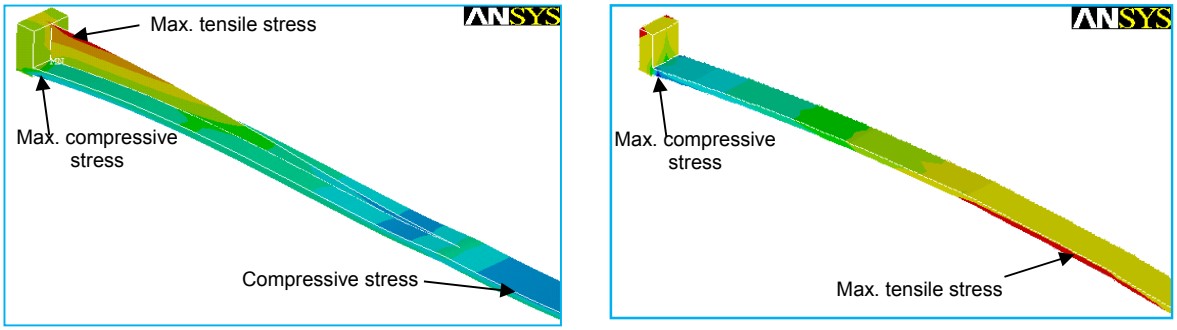

Figure 5-9 The Maximum Tensile and Compressive Stresses Locations in the HCB Concrete Arch of G3 due to a) stage 2 loading b) stage 3 loading

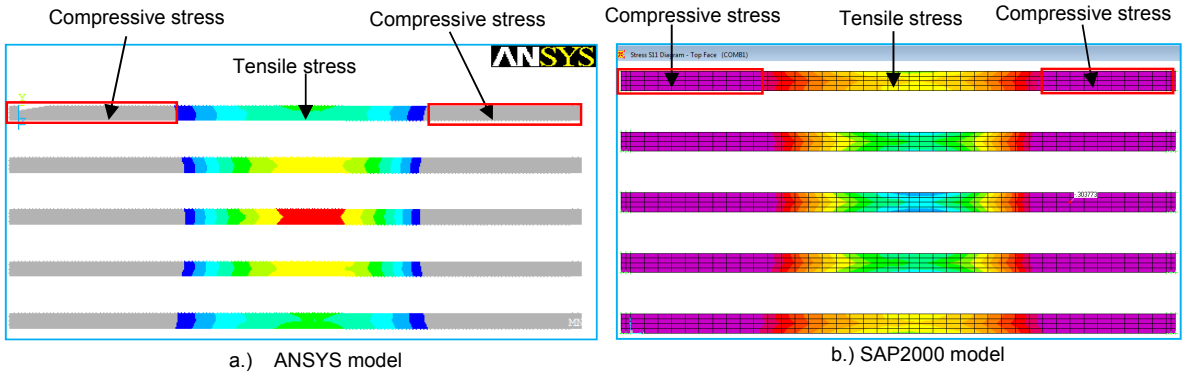

Figure 5-10 Stresses in the Lower FRP Flanges of all the Girders due to Stage 3 loading

The previous results indicate that the current design methodology may need some refinements. An experimental investigation is recommended to assure the stress results obtained from the FEMs. Regardless the design methodology and assumptions, the results proved that the classic arch shape optimizes the use of the concrete and preserves the HCB overall stiffness under the service loads.

The results showed that the HCBs underwent lateral and rotational deformations under the vertical truck loads in the three stops. The value of the maximum lateral displacement occurred in FRP webs in G1 and G5 and was found about 20% of the maximum vertical deflection in the three load cases. Since, this may indicate that the HCB has weak lateral and torsional stiffness, field measurements need to be performed to verify the FEMs observation. Figure 5-11displays the lateral and rotational deformations of the HCBs due to stop 3 loads.

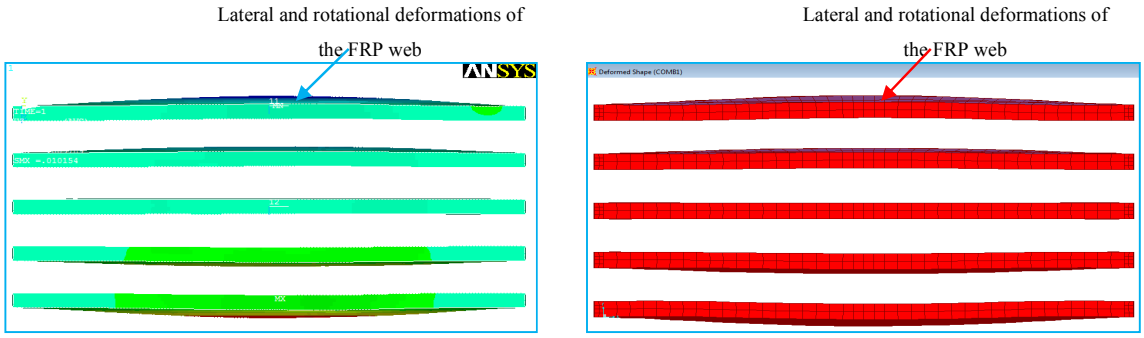

Figure 5-11 Exaggerated Deformed Shape of HCBs Due to Stop 3 Loads

A study was performed to identify the contribution of the polyiso foam to the lateral stiffness of the HCB. It was found that when the foam was removed from the HCBs, the FRP webs underwent very large deformations. Consequently, the exact contribution of the foam to the lateral stiffness could not be precisely determined. Nevertheless, the previous study proved that the foam plays an important role for the stability of the FRP shell because it prevents the local buckling of the FRP webs and provide lateral stability to them.

5.7. LOAD TESTING OF BRIDGE 0478

The research team from MS&T conducted a load test on B4078 on November 14, 2013. A Leica total station and 18 prisms were used to measure the deflection along each girder. An additional three prisms were used as control points to make sure the total station did not move during the testing. Two MODOT three-axle trucks were used to perform four

stops simulating different load cases on the first span of the bridge. A sample of these stops is illustrated by Figure 5-12. Similar to the load testing of B0439, the stops were selected to produce maximum moments and shear forces in the HCBs. Because, FEMs were developed to simulate the superstructures of B0439 and B0410, there was no need to construct FEMs to B0478. The test was used to assure that the induced deflections are within the permissible values provided by AASHTO LRFD (2012). The maximum deflection took place on the midspan of girder 4 (G4) due to stop 3 Figure 5-13. The maximum deflection was found 0.204-in. This deflection is 28 % of the permissible maximum deflection (L/800), which is 0.72-in. Though, this deflection is significantly higher than the maximum deflection resulted in B0439 HCBs, it suggests that the HCBs of B0478 possess the required flexural and shear rigidity to withstand the applied loads.

Figure 5-12 Two MoDOT Truck Simulating Load Cases on B0478

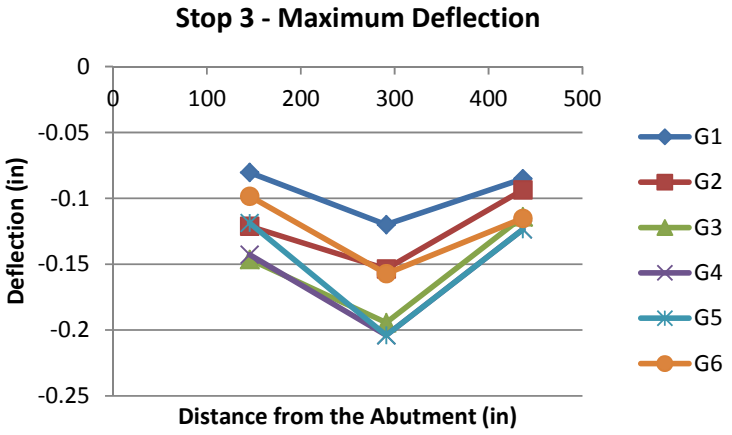

Figure 5-13 Measured deflections in B0478 girders due to Stop 3

5.8. SUMMARY AND CONCLUSIONS

In this chapter, the results of the field tests performed on B0439 and B0478 are presented. Two FEMs were constructed for bridge 0439 superstructure using the commercial packages ANSYS V13 and SAP2000 V14.2. The FEMs demonstrate that the linear FEA can predict the behavior of the HCB under service loads with acceptable accuracy. A simple analytical procedure, based on the transformed area method, was used to estimate the deflection along B0439 HCBs. The methodology was found significantly conservative in predicting the HCBs deflection. This can be mainly attributed to ignoring the continuity of the bridge deck. The results showed that the design/analysis of the HCB in continuous structures requires sophisticated analysis.

The FEA proved that the classical arch shape of the compression reinforcement optimizes the use of the concrete and preserves the overall stiffness of the HCB under service loads. The maximum measured deflection in B0439 HCBs due to different load cases was found less than 6% of the permissible live load deflection provided by AASHTO LRFD (2012) . The numerical simulation illustrated that the maximum deflection due to the notional loads provided by AASHTO LRFD (2012) is expected to be in the range of 17% of the permissible live load deflection. While the maximum measured deflection in B0478 HCBs due to different load cases was about 28% of the permissible live load deflection provided by AASHTO LRFD (2012). These deflections and the predicted stresses by the FEA clarify that the HCB possesses a sufficient flexural and shear rigidity that avoids excessive deflections under service loads. In addition, the low stress carried by the FRP shell under the service loads, maintains the ability for long-term durability of the shell, hence increasing the lifetime of the HCB as a whole.

Although the HCB seems to be a promising technology in the bridge applications, the FEMs' results suggested that the current design methodology of the HCB has room for improvement and may need some refinements. It also pointed out that the HCB may suffer lateral and rotational deformations under the vertical loads. The experimental investigations and the mathematical analysis performed on B0410 aimed to examine the flexural behavior of the HCB based on these conclusions. The results of the study performed on B0410 are presented in the following chapter.

6. FLEXURAL BEHAVIOR OF HYBRID COMPOSITE BEAM

6.1. INTRODUCTION

Based on the finite element modeling of the first bridge and the literature results, this chapter aims: to examine the flexural behavior of the full-scale HCB within in-service bridges, to evaluate the current design methodology and assumptions, and to propose modifications to the current methodology to enhance its ability to predict the stresses under the service loads. To achieve these goals, a FEM is constructed for B0410 superstructure using the commercial software, Ansys V14. The FEM, the existing design methodology, and a proposed methodology are used to predict the normal strain in the different elements of the instrumented HCB, through different loading stages.

In this chapter, the field-testing of the second bridge (B0410) is presented. The numerical predictions are compared to the experimentally measured strains during the concrete arch pour and the conducted load test. Finally, the flexural behavior of the HCB is analyzed.

6.2. LOAD TESTING OF BRIDGE 0410

As it is described in 3.5, different elements of HCB2 (the middle girder) of B0410 have been instrumented with different sensors. Due to the construction sequence of the HCB bridges, HCB2 is subjected to three stages of dead and live loading. In the first stage: the GFRP shell and the strands are subjected to stresses result from casting the concrete arch and web. In the second stage: the non-composite HCB is subjected to the load result from the deck and barriers pour. In the third stage: the composite HCB is subjected to the live load resulting from in-service traffic.

Strain readings were taken an hour before the beginning of the concrete arch pour until 24 hours after the completion of the pour. The initial strain data were subtracted from the final readings providing the strains induced in the shell and strands during stage 1 loads. A sample of these results is presented in 4.8. Unfortunately, no data was collected during the deck pour (stage 2).

A load test was carried out, using two fully loaded ten-wheel three-axle trucks, to simulate stage 3 loading. The trucks performed three stops simulating three different load cases (Figure 6-1). The stops were selected to produce maximum bending moments and shear forces in HCB2. The front axle load (P1) of the first truck (T-1995) was 16.48 kips; the

middle axle load (P2) was 15.58 kips; and the rear axle load (P3) was 24.4 kips. While P1 of the second truck (T-2406) equaled 16.42 kips; P2 equaled 20.52 kips; and P3 equaled 20.04 kips. Figure 6-2 illustrates the dimensions of the trucks used to perform to load.

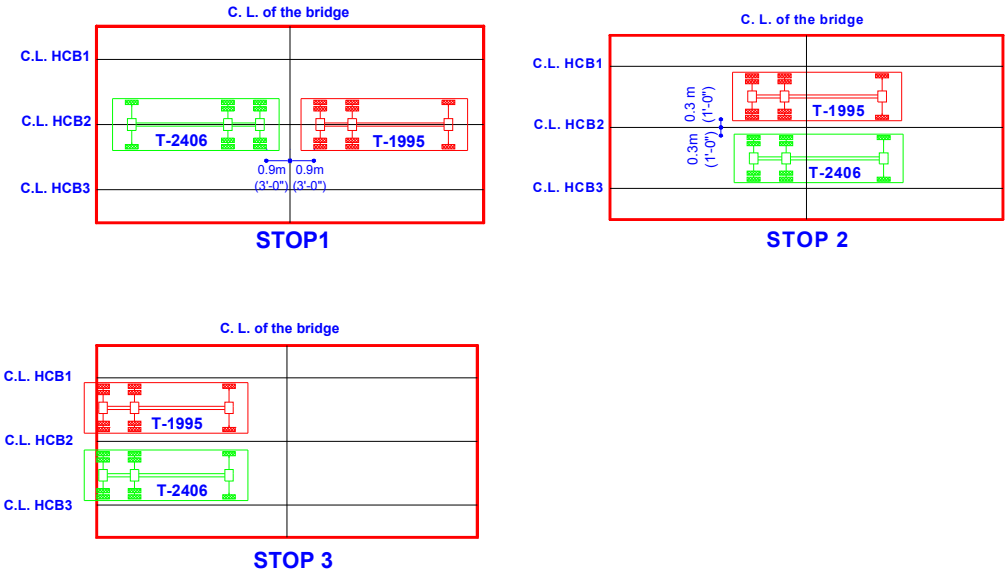

Figure 6-1 Truck Stops during B0410 Load Test

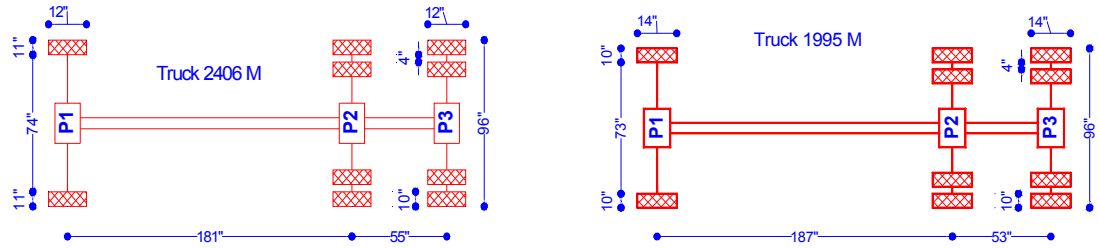

Figure 6-2 Truck Dimensions (B0410 Load Test)

The traffic was stopped, and initial strain measurements were recorded before performing the three stops. As in the first stage, these strains served as baseline and were subtracted from the strains induced due to the three stops. Hence, the strains induced in the HCB2 elements due to pure live loading were obtained.

6.3. FINITE ELEMENT MODELING OF BRIDGE 0410

The bridge superstructure was modeled via the commercial FEA software ANSYS 14. The FEM consists of 224568 elements and 213634 nodes. The Y-axis was oriented in the

gravity direction, the X-axis was oriented in the longitudinal direction of the beams, while the Z- axis was oriented in the lateral direction of the HCBs. Figure 6-3 shows the FEM of B0410 superstructures.

Based on the experimental measurements and the mathematical predictions (that will be presented later) all the materials were modeled as linear elastic. The results obtained from the FEMs also proved that all the materials behave within their elastic range.

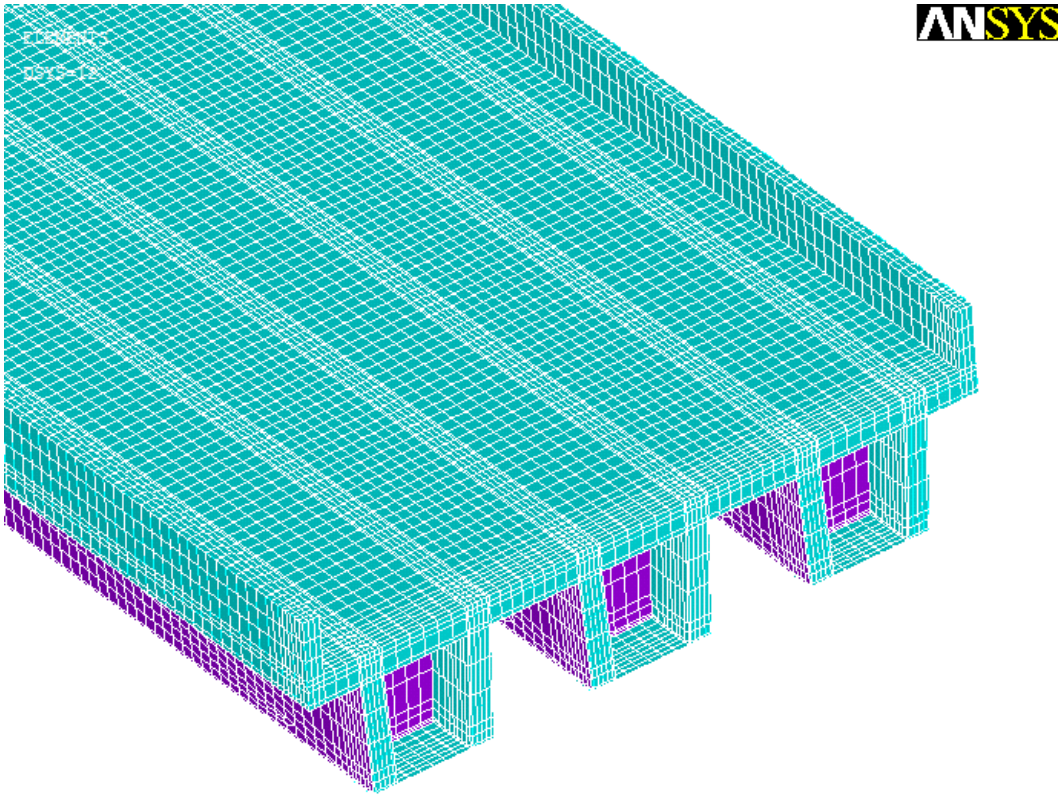

Figure 6-3 Finite Element Modeling of B0410 using ANSYS V14.0

6.3.1. Element Types and Model Simplifications

6.3.1.1 Hybrid Composite Beam (HCB)

Similar to B0439, the HCB was modeled using a combination of one, two and three-dimensional space elements. The GFRP shell and the concrete web were modeled using shell181 element. The concrete arch was modeled using solid65 element and the polyiso foam was modeled using solid185 element. The HCB strands were modeled using beam188 element, which has six DOFs at each node. The tension reinforcement is arranged in two layers that lie directly on the lower FRP flange. In the FEM the strands were shifted upward and modeled in one layer separated from the lower flange by 1" foam. To simplify modeling,

the 44 strands were modeled via five separate beam elements. The total cross-sectional area of the five beam elements equals the cross-sectional area of the 44 strands. A perfect bond between all the components of the HCB were assumed. This was achieved by meshing all the constituents using the same mesh. Figure 6-4 demonstrates the finite element modeling of HCB using ANSYS V14.

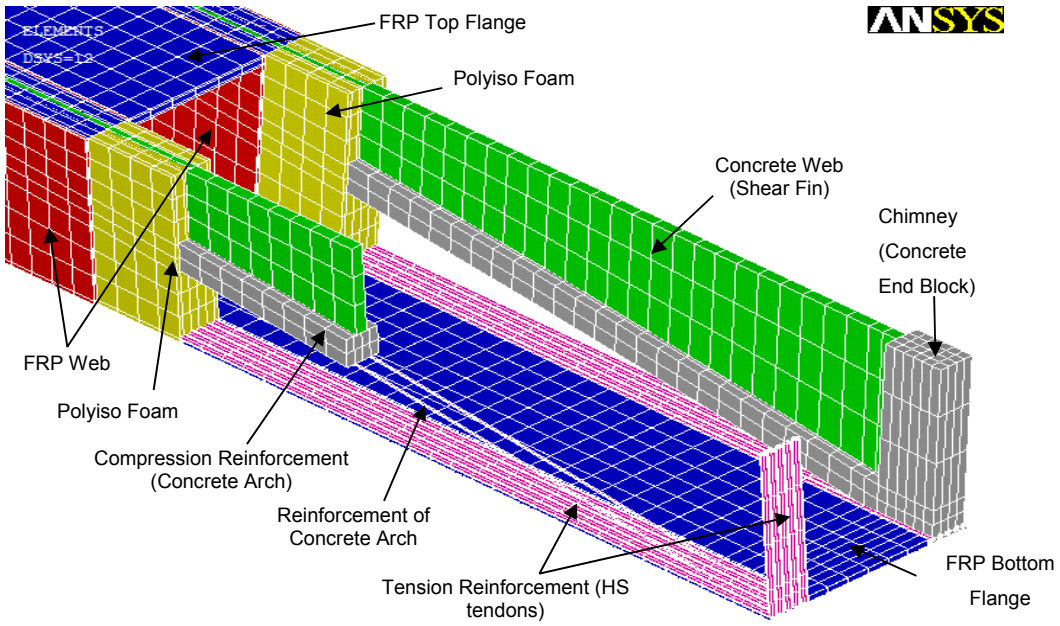

Figure 6-4 Finite Element Modeling of Double-Web HCB of B0410 using ANSYS V14.0

6.3.1.2 Bridge Deck

Solid65 elements were used to model the bridge concrete slab. Three solid elements were used throughout the slab thickness to allow modeling of the upper and lower reinforcement bars via beam188 elements. The parapet was poured simultaneously with the slab, and its reinforcement extended into the deck. Consequently, the parapet was included in the FEM and simulated using solid65 element. A perfect bond was assumed between the deck components and between the deck and the HCBs.

6.3.2. Modeling of Loads

In the first stage, the weight of the concrete arch and web were applied as uniform load on the lower foam elements (the foam elements below the concrete arch). In the second stage, the weight of the deck was applied as uniform load on the upper flange elements of the non-composite HCB. In the last stage, the trucks loads were applied to the bridge superstructure as uniform distributed load on the upper surface of the deck elements. Finally,

a linear superposition was performed between the three stages to obtain the total stresses in the different components of the HCB.

6.3.3. Modeling of Boundary Conditions

Each end of the HCBs of B0410 is supported on two steel-laminated neoprene bearing pads. Each elastomeric bearing pad is 12-in. x 12-in. x 0.75-in. and located underneath the chimney. The stress-strain behavior of an elastomer is controlled by the shear modulus and the shape factor of the elastomer (Yazdani et al. 2000). According to AASHTO LRFD (2012) the elastomer shall have a shear modulus ranges from 95 psi to 200 psi. In the current work, the shear modulus of the elastomer is assumed 145 psi. The shape factor, S, of rectangular elastomer layer is given by (AASHTO LRFD 2012):

$$S = \frac{LW}{2h_{ri}(L+W)} \tag{6.1}$$

where L is the dimension of the bearing in the longitudinal direction of the beam (X-dir.), W is the dimension of the bearing normal to the longitudinal beam axis (Z-dir.), h_{ri} is the thickness of a single elastomer layer.

A simplified equation based on the shear modulus, G, and the shape factor is provided by AASHTO (1996) to detect the stiffness of the bearings as follows:

$$E_b = 6GS^2 \tag{6.2}$$

where E_b is the effective compressive modulus of the bearing.

Yazdani et al (2000) derived six translational and rotational stiffness values that can simulate the restrained forces and moments at the beam-pad interface. According to their study, the translational stiffness of the bearing in X-dir., k_{xb}, and the rotational stiffness about Z-axis, k_{rzb}, are given by:

$$k_{xb} = \frac{CGA_{xz}}{H} \tag{6.3}$$

$$k_{rzb} = \frac{CE_bI_z}{H} \tag{6.4}$$

where A_{xz} is the area of the bearing in the xz plane, H is the total thickness of the bearing, I_z is the moment of inertia of the bearing about z-axis and C is a factor that presents the effects of aging and cold temperatures on the elastomer stiffness. The aging and temperature effects can increase the stiffness of the elastomer up to 50 times the original stiffness (Roeder et al. 1989). Based on the results obtained by Yazdani et al (2000), C is assumed 25 in the current study.

The FEA study of B0439, presented in the previous chapter, showed that modeling the bearing pads using pin supports that restrain the translational movements in all the directions led to acceptable predictions of the HCBs deflections. During the FEM of B0410 superstructure, two models were constructed with different boundary conditions to study the best simulation of the bearings effects. In the first model, the bearings were simulated via pin-pin supports similar to the B0439 FEM. While in the second model, the bearings were represented by preventing the vertical movement in the gravity direction (Y-dir.), in addition to applying translational and rotational springs given by equations (6.3 and 6.4) respectively. In the second model, the out-of-plane translational and rotational springs (k_{zb}, and k_{rxb} and k_{ryb} respectively), derived by Yazdani et al (2000), were not applied because the bridge incorporated the use of concrete diaphragms that span between the HCBs ends and rested directly on the interior and exterior bents. These diaphragms were simulated in both models by applying supports that restrain the lateral translation of the HCBs at the contact areas between the diaphragms and the beams. The comparison between the field measured strains due to the three load stops and the FEM predictions showed that the second model achieved better correlation with the experimental data. Consequently, the supports of the HCB in second and third stages were presented using roller supports combined with translational and rotational springs as in the second model. During the concrete arch pour (the first stage); the HCB was supported on two concrete blocks. These blocks were assumed to prevent the displacement of the HCB in all directions. Consequently, in this stage the HCB was modeled with pin supports at each end.

6.4. FLEXURAL DESIGN OF HCB

A typical cross-section of composite HCB is illustrated in Figure 6-5. In real bridges, the actual elements may deviate slightly from those shown in this figure. The current flexural design methodology calculates the nominal bending moment capacity of the HCB using the following assumptions:

Plane sections perpendicular to the neutral axis (NA) before bending remain plane and perpendicular to the NA after bending (linear strain distribution throughout the depth of the HCB).

The strain of different constituents at the same level is equal (perfect bond between the constituents of the beam).

The concrete below the NA has cracked and no longer contributes to the strength of the beam.

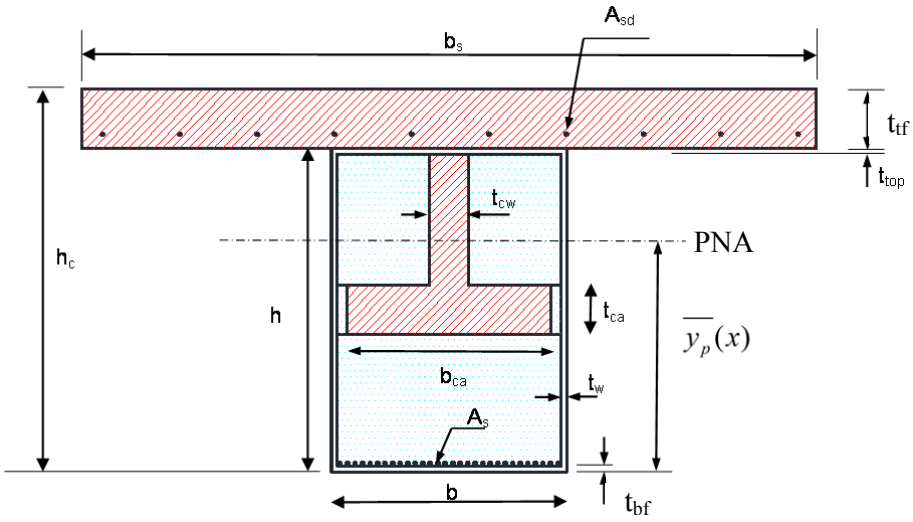

Figure 6-5 Typical Cross-section of the Composite Hybrid-Composite Beam

Based on bridges designed and constructed to date, the failure mode for HCB is crushing of the concrete rather than failure of the laminate or ductile failure of the strands (Hillman, 2012). By considering the HCB over-reinforced, the design process, for the nominal bending capacity, starts with considering the strain at the extreme upper fiber of concrete equals to the ultimate concrete strain. Using the strain compatibility approach, the strains in the different components are related to the concrete strain as follows:

$$\varepsilon_i(x) = \frac{\varepsilon_{cu} \times \left(y_i(x) - \overline{y_p}(x) \right)}{h_c - \overline{y_p}(x)} \tag{6.5}$$

where $\varepsilon_i(x)$ is the strain of the component i at distance x from the beam end, ε_{cu} is the ultimate strain of the concrete and is assumed -0.003 (ACI, 2011), $y_i(x)$ is the distance from

the c.g. of the component i to the extreme lower fiber of the beam at distance x from the beam end, $\overline{y_p}(x)$ is the distance from the plastic neutral axis (PNA) of the composite section to the extreme lower fiber of the beam at distance x, and h_c is the total depth of the composite section.

The force in the FRP elements, strands, and the deck reinforcement, $F_i(x)$, can be calculated as follows

$$F_i(x) = E_i \varepsilon_i(x) A_i \tag{6.6}$$

where E_i is elastic modulus of the component i, and A_i is the cross-sectional area of the component i.

By assuming the PNA, at distance x from the beam end, to be within the concrete web, the force in the concrete components can be calculated as follows

$$F_{cs}(x) = 0.85 f_{cs}^{'} t_s b_s \tag{6.7}$$

$$F_{cw}(x) = 0.85 f_{ca}^{'} \beta_1 \left(h - t_{tf} - \overline{y}_p(x)\right) t_{cw} \tag{6.8}$$

$$F_{ca}(x) = 0 \tag{6.9}$$

where $F_{cs}(x)$, $F_{cw}(x)$,and $F_{ca}(x)$ are the forces in the deck slab, concrete web, and concrete arch respectively, $f_{cs}^{'}$ and $f_{ca}^{'}$ are the compressive strength of the deck and arch concrete respectively, t_s, t_{tf}, and t_{cw} are the thicknesses of the deck slab, top FRP flange, and concrete web respectively, b_s is the effective slab width, h is the depth of the FRP box, and β_1 is a factor that relates the depth of the equivalent stress block to the actual stress depth. The value of β_1 can be found in (ACI, 2011).

The PNA location can be calculated by equilibrating the horizontal forces:

$$\sum_{i=1}^{n} F_i(x) = 0 \tag{6.10}$$

where n is the number of the HCB elements. However, the PNA may lie within the deck slab, concrete web, concrete arch, or below the concrete arch. Subsequently, identifying the PNA location requires using a trial and error method.

Once the PNA is identified, the reduced nominal moment capacity of the composite section can be estimated by summing the moments around the PNA location and applying the reduction factor:

$$\phi M_n(x) = 0.81\left(\sum_{i=1}^{n} F_i d_i(x)\right) \tag{6.11}$$

where $d_i(x)$ is the distance from the component i force to the PNA (moment arm), and ϕ is the reduction strength factor. Though, ACI (2012) recommends a strength reduction factor which equals 0.65 for the reinforced concrete compression controlled member, Hillman (2012) uses the factor recommended by ACI (2012) for tension controlled members (0.9) multiplied by other reduction factor (0.9) that compensates for including FRP laminates in the HCB.

Finally, the reduced nominal moment should satisfy the following equation:

$$\phi M_n(x) \geq M_u(x) \tag{6.12}$$

where $M_u(x)$ is the factored bending moment. For highway bridge applications, the factored moment shall be estimated using the design loads provided by (AASHTO-LRFD, 2012).

It should be noted that the compression forces calculated in the concrete components using Whitney stress block (equations 6.7 & 6.8) are approximate forces. Because Whitney stress block method is applied for concrete elements that subjected to strains range from zero to the ultimate concrete strain. For example, equation (6.8) overestimates the concrete force in the web because the strain at the top of the concrete web is less than 0.003.

Hillman (2003) proposed second methodology that achieves more accurate estimation of the nominal bending capacity of the HCB. Instead of assuming a uniform stress in the compression block, the actual stress relative to the strain in the concrete is used based on a parabolic stress-strain curve for concrete. The most common curves that are used to relate the concrete compressive stress to its strain are: modified Hognestad curve (Hognestad, 1951), Todeschini curve (Todeschini et al., 1964), and Thorenfeldt, Tomaszewicz, and Jensen curve

(Thorenfeldt et al., 1987). A brief discussion about these curves can be found in (Wight & MacGregor, 2012).

Once, the stress is related to the strain in the concrete components, the axial force in each component, $F_{Ci}(x)$, can then be calculated by:

$$F_{Ci}(x) = b_i \int_{y_{li}}^{y_{ui}} f_i(x, y) dy \tag{6.13}$$

Where b_i is the width of the concrete component i, y_{uij} and y_{lij} are the distances from the extreme upper and lower fibers of the component i to the extreme lower fiber of the beam at distance x respectively, and $f_i(x, y)$ is the stress of the concrete component i at the location (x, y).

6.5. MATHEMATICAL CALCULATION OF THE STRAIN

The strains in the different HCB elements of B0410 due to the applied loads were calculated using the second design methodology presented in the previous section. However, the concrete subjected to tensile stress was assumed to contribute to the strength and stiffness of the HCB up to the modulus of rupture of the concrete. This aimed to allow the comparison between the tensile strains captured by some sensors in the arch and the estimated strains. It should be noted also that, under the applied loads the strain at the upper concrete fiber cannot be assumed to equal the ultimate concrete strain.

A MATLAB code was implemented to calculate the PNAs at the sensor locations using iterative procedure. The code assumes initial value for the PNA at distance x. Thereafter, the axial forces of the different components are calculated. If the forces don't equilibrate the code moves the PNA upward or downward based on the forces' values, and the process is repeated until convergence is achieved.

However, the strains obtained from the mathematical procedure are found in the elastic ranges of all the constituting materials. Consequently, the strains under the applied loads can be calculated in one-step by:

$$\varepsilon_i(x) = \frac{M(x)\left(\bar{y}(x) - y_i(x)\right)}{I(x)E_w} \tag{6.14}$$

where $M(x)$ is the bending moment in the HCB at distance x due to the applied loads, $\bar{y}(x)$ is the distance from the elastic neutral axis (ENA) to the extreme lower fiber of the HCB at distance x, E_w is the elastic modulus of the shell web, and $I(x)$ is the transformed moment of inertia of the composite section, with respect to the elastic modulus of the shell web, about the ENA at distance x. The transformed moment of inertia can be calculated via equation (5.9).

6.6. MODIFIED METHODOLOGY

Two modifications were applied to the current design methodology to enhance the strain estimation in the different components of the HCB. One modification was applied to the beam geometry, while the other was applied to its boundary condition.

Due to the parabolic profile of the compression reinforcement, horizontal movements and normal forces are expected to induce through the length of the beam. Consequently, the stresses and strains are expected to be sensitive to the type of translational restraint that is provided at the end of the beam in its longitudinal direction, X-dir. The current design methodology models the HCB as a simply supported straight beam. Therefore, neither axial forces induce through the beam nor the model is sensitive to the restrained translational DOFs in the longitudinal direction. It is noticed, during the mathematical modeling of B0410 and B0439 that, the ENAs of the non-composite and composite HCB (stages 2 and 3) form curved path starting at the bottom at the supports with an apex at the center of the beam. Therefore, the first modification was achieved by modeling the HCB as curved beam, based on the ENAs locations, rather than straight one.

The second proposed modification was performed by modeling the supports at each end by roller support that prevents the displacement in Y-dir. in addition to translational spring in X-dir. and rotational spring about Z-axis. Under static vertical loads, the FRP shell and the strands are expected to deform downward only, while the concrete arch is expected to perform horizontal and vertical movements. The horizontal deformation of the concrete arch is partially restrained by the strands at the end of the beam, while the horizontal movement of the overall beam is partially restrained by the bearing pads at each end. Since the concrete arch is the source for the horizontal movement of the HCB under static vertical loads, it may be acceptable to simulate the restrained horizontal forces at each end of the beam using translational spring that has the following stiffness

$$K_x = K_{xb} + K_{xs} \tag{6.15}$$

where K_x is the translational spring stiffness at the end of the HCB in X-dir., K_{xb} is the stiffness presented by the bearing pad and is given by Eq. (5), and K_{xs} is the stiffness provided by the strands.

It can be shown that K_{xs} is given by the following equation:

$$K_{xs} = \frac{2E_s A_s}{L} \tag{6.16}$$

where E_s the elastic modulus of the strands and A_s is the cross-sectional area respectively. The stiffness of the rotational springs at the HCB ends were calculated using eq. (6.4). Then, the strains were estimated by modifying eq. (6.14) to account for the axial force in the beam as follows:

$$\varepsilon_i(x) = \frac{M(x)\left(\bar{y}(x) - y_i(x)\right)}{I(x)E_w} + \frac{N(x)}{A(x) \times E_w} \tag{6.17}$$

where *N(x)* is the axial force at distance (x), *A(x)* is the transformed cross sectional area of the composite section, with respect to the elastic modulus of the shell web.

The proposed modifications were applied only to the second and third stages. While in the first stage, HCB without compression reinforcement, the ENA is at the same location along the beam length. Consequently, the beam was modeled as a straight beam without any modification to the existing methodology.

6.7. RESULTS DISCUSSION

Figures Figure 6-6 and Figure 6-7 illustrate the measured and estimated normal strains in the different elements of HCB2 due to the loads of the three stops (stage 3), and casting the concrete arch (stage1) respectively. While figures Figure 6-8 and Figure 6-9, show only the estimated strains in HCB2 due to the second stage loads and the total loading of the three stages respectively. The total loads of the three stages were obtained by adding stop 2 loads to the loads of the first and the second stages. In these figures (Figure 6-6 to Figure 6-9), the VWSGs are denoted by C, the FRP gauges are denoted by F, and the strands strain gauges are denoted by S. The results show that the field measured strains and the estimated ones by the FEM during the first and third stages are in a good agreement. At the location of the FRP

strain gauge F7, the FEM predicted higher strains than the measured ones in the three stops and the first stage. As it is clarified in figures Figure 3-14and Figure 3-15, the gauges F1 and F7 are very close to each other and were expected to capture close strains as predicted by the three numerical methods in all the stages. However, all the measured strains by F7 are significantly lower than those captured by F1. This indicates that F7 might provide inaccurate strain readings due to the anisotropic nature of the FRP. The strain gauge may capture a local behavior of the FRP shell at this location or may be affected by the fiber orientation of the outer layer (Ahsan 2012).

The results also clarify that the FEM predicted higher strains in the concrete arch than the measured strains in the three stops. Since the mix design of the concrete arches of B0410 contained fly ash, an explanation of this difference is that the arch might gain higher strength than that is used in the FEM. Studies executed by many researchers such as (Han et al. 2003, Hwang et al. 2004) showed that the fly-ash concrete achieves significant increase in the strength after 28 days and the increase in strength continues at the long-term due to the pozzolanic reaction. Generally, the differences between the FEM predictions and the measured strains may be within the expected range of errors for a full-scale bridge testing. Consequently, the FEM was used to analyze the flexural behavior of the HCB and as a reference for evaluating the performance of the current and modified methodologies in estimating the strains due to the second stage and total loading.

In the three stops, the maximum compressive stresses in the concrete arch were found very close to the junction of the arch with the chimney. Figure 6-6 demonstrates that the VWSG (C7) instrumented at this location captured the maximum normal compressive strains due to all the truck stops. Figures Figure 6-6 and Figure 6-10 show that the same behavior predicted by the FEM. According to the existing design model, C6 is located below the ENA in all the stops and the bending moment is small at this location. Consequently, the current model always predicted very small tensile strains at C6. Figures (Figure 6-6-b and Figure 6-6-d) illustrate that the FRP strain gauge F3 captured compressive strains during stops 1 and 2. These results indicate that the HCB is subjected to negative bending moment at the support locations due to the restrained moments at the beam-pad interface. The negative moment is probably combined with axial compressive force along the beam length due to the parabolic profile of the compression reinforcement.

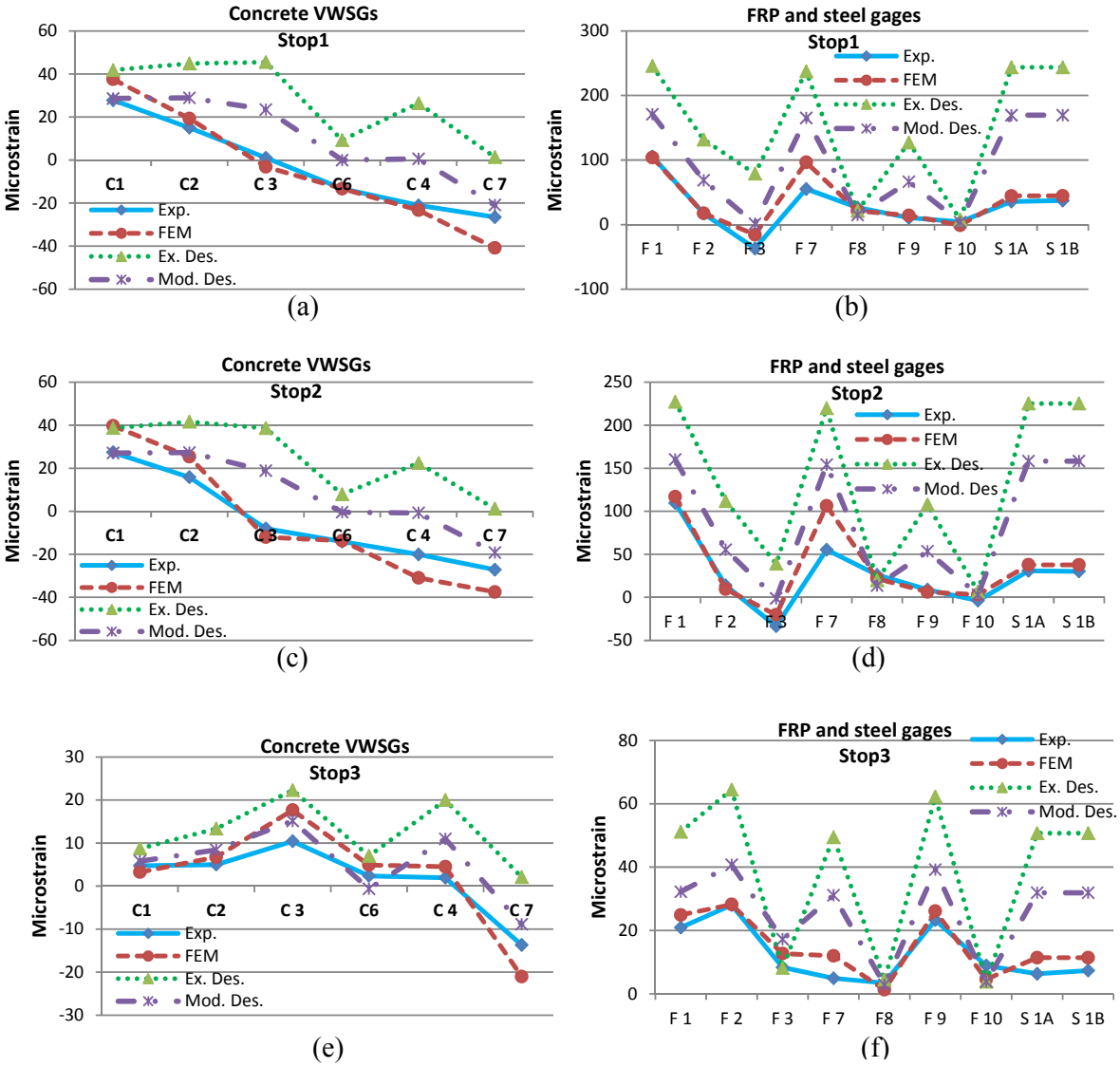

Figure 6-6 Strain Values in HCB2, B0410, Due to the Three Stops (Stage 3)

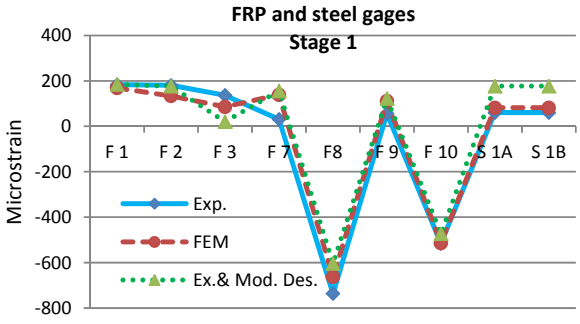

Figure 6-7 Strain Values in HCB2, B0410, Due to the Concrete Arch Pour (Stage 1)

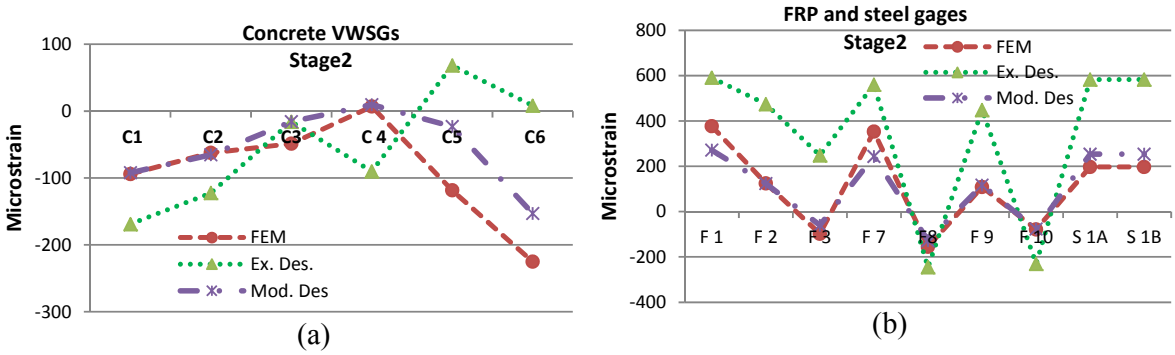

Figure 6-8 Strain Values in HCB2, B0410, Due to the Deck Pour (Stage 2)

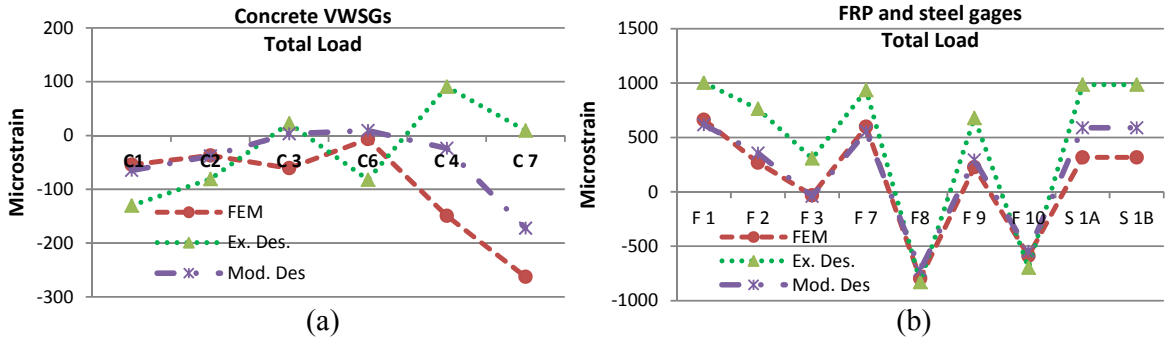

Figure 6-9 Strain Values in HCB2, B0410, Due Total Loads of the Three Stages

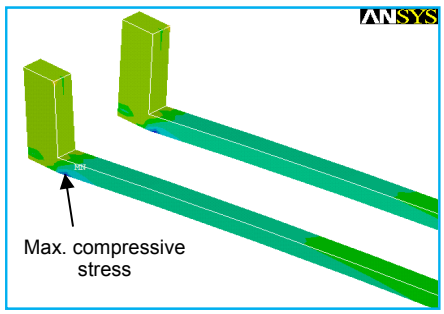

Figure 6-10 Normal Stresses in Concrete Arches of HCB2 due to Stop1

Generally, the comparison between the field strains and existing design procedure strains shows that the methodology is accurate in predicting the strains in the first stage, in which the HCB is prismatic along its length. While the results clarify that, the model is unable to predict the maximum compressive stresses in the concrete arch and significantly conservative in predicting the tensile stresses in the FRP shell and strands in the third stage. The same trend was observed in the second stage, based on the FEM predictions. This behavior can be attributed to neglecting the negative moment at the beam end and the axial force through the beam. When the non-composite HCB of B0410 was modeled using pin

supports at one end and roller support at the other end, the maximum compressive stress in the concrete arch was found at the same location and negative bending observed at the end of the beam. In the previous chapter, the writers attributed the negative moment at the beam end of the simply supported HCB to partial fixation provided by the chimney to the beam end. Since the bearing stiffness effect is documented by many researchers such as (Yazdani et al. 2000, Cai and Shahawy 2003), it is assumed that the bearing stiffness is the main cause of the negative moment at the HCB end in this study. Consequently, no definite conclusion regarding the chimney stiffness effect can be drawn from the experimental results of the current work.

Figure 6-6 illustrates that the measured strains at the strands mid-span (S1A and S1B) are significantly lower than the bottom flange strains at the same location (F1). In the FEM, the strands were separated from the lower flange by 1-in. foam, and a perfect bond was assumed between all the superstructure components. If the HCB has perfect beam-behavior, the strains in the strands and the bottom flange should be very close to each other. However, similar difference, to what observed experimentally, was detected by the FEM. This indicated that some of the design assumptions might be invalid. In order to verify the design assumptions, the FEM results were used to develop strain profiles throughout the thickness of the composite and non-composite HCB. The strain profiles at section (A-A) due to stop 1, and (D-D) due to stop 3 are presented in figures (Figure 6-11-a) and (Figure 6-12-a) respectively. While the strain profile of the non-composite HCB at section (C-C) is displayed in Figure 6-12-b. Figures Figure 6-11 and Figure 6-12 illustrate also the strain profiles obtained by the modified methodology, which is based on the same assumptions as the current one. In these figures, the FEM strains in the concrete arch and web, strands, FRP shell, and concrete of the deck are denoted by CM, SM, FM, and DM respectively. The strain profiles show that the assumption “the strain of different constituents at the same level is equal” is invalid. Nosdall (2013) also noticed a strain incompatibility between the concrete arch and the GFRP shell, which agrees with the FEM results presented in this study. The strain incompatibility between the HCB components can be attributed to the low shear moduli of the polyiso foam. The foam behaves as a flexible shear connection and allows differential vertical and horizontal displacements between the HCB elements. Figure 6-11-b shows the displacement in X-dir. of the composite HCB elements at the midspan of the beam due to stop 1. Vertical differential movements between the HCB components was also detected by the FEM. (Mascaro and Moen 2012) recorded relative vertical movements between the concrete arch and the FRP shell using two experimental methods: close-range

photogrammetry and LVDTs measurements, which matches the current FEM results. Due to the relative movements between the HCB elements, the strain distribution throughout the deck, concrete arch and concrete web is linear due to the rigid connection between these components, the strain distribution through the GFRP shell components is linear but with different slope, while the strain in the strands is independent. The effect of the flexible shear connections is documented by many researchers among them Keller and Gürtler (2006).

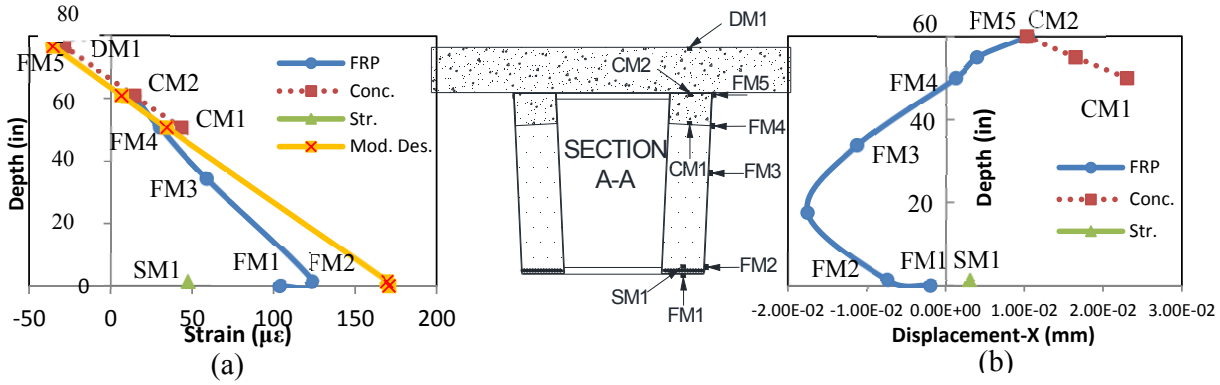

Figure 6-11 (a) Strain Profile (b) Displacement in X-dir.
Due to Stop1 Sec. (A-A)

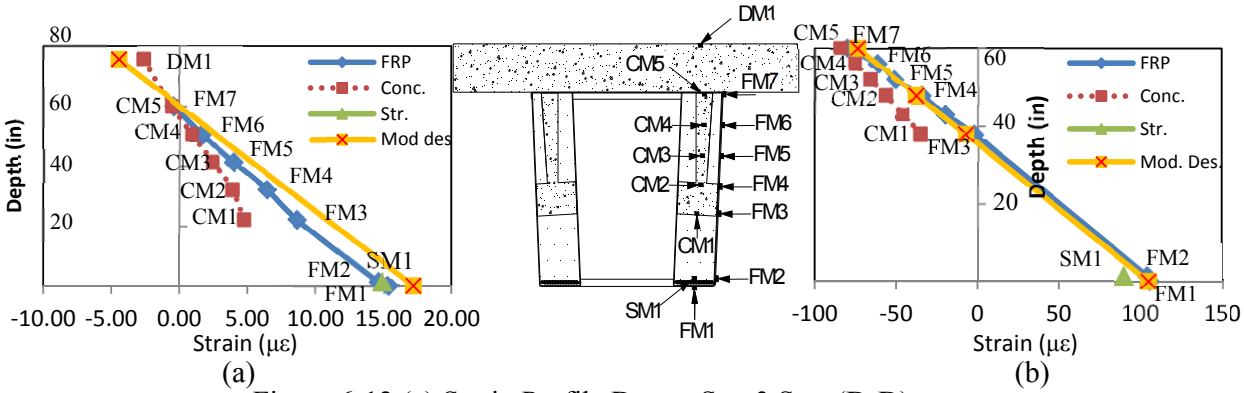

Figure 6-12 (a) Strain Profile Due to Stop3 Sec. (D-D)
(b) Strain Profiles Due to Stage 2 Loads Sec. (C-C) (non-composite HCB)

The FEM results showed that the stress is not constant along the strand length. The same behavior was noticed by Hillman (2003) during testing the first HCB prototype, consequently he concluded that the HCB behaves like beam rather than tied arch. However, the strands were found always subjected to tensile stresses even where the FRP lower shell has compressive stresses. This indicates that the strands are subjected to axial force at the beam end and work as a tie for the concrete arch and at the same time contribute to the flexural rigidity of the beam. When Snape and Lindyberg (2009) loaded the HCB up to failure, the failure occurred when the anchoring of the tension reinforcement broke free at

end of the beam. This behavior supports the conclusion that the strands are subjected to axial force at the beam end and restrain the horizontal movement of the beam as assumed by equation (6-15). Figure 6-11-a illustrates a difference between the strains at the bottom flange and the web (FM1 and FM2). Similar differences were noticed at other sections and can be attributed to the differential movement between the strands and the bottom flange. Due to this displacement, shear stresses induce at the strands-foam and flange-foam interfaces and result in axial forces along the length of the strands and the bottom flange. In practice, these axial forces are expected to transfer between the strands and the bottom flange through the layer of resin that separate the two elements.

Including all the aforementioned factors to the mathematical model seems challenging and would complicate the design process for several reasons, among them: the differential displacement between the HCB elements does not follow specific pattern at some sections as it is clarified by Figure 6-11-b. Even if the differential displacement is assumed to follow linear pattern to simplify driving an equation that relates the slippage to the distance in X-dir., the fact that the geometric properties are functions of the distance in X-dir., leads to complex differential equation that has no explicit solution. Consequently, no closed form solution can be obtained to identify the relative displacements between the different elements of the HCB. Consequently, the modified methodology accounted only for the bearing effects and the curved shape of the HCB to simplify the design process. Figure 6-6 demonstrates that the modified methodology achieved some enhancement in estimating the normal strain in the different elements of the HCB. However, it illustrates that the methodology is unconservative in identifying the maximum compressive stress in the concrete arch and unable to identify the strains in some of the concrete locations accurately. The same trend was observed in the second stage, Figure 6-8-a. This suggests that the axial compressive force induced in the arch may be higher than that predicted by the modified methodology especially close to the beam end. Due to the partial composite action between the HCB constituents, the arch may have axial compressive force that is not proportioned to the axial forces of the other elements through their extensional stiffnesses as suggested by Equation (6.17).

Figures (Figure 6-9, Figure 6-11, and Figure 6-12) illustrate that, in spite of ignoring the strain incompatibility between the different elements of the HCB, the design methodology proposed in the current work achieved an acceptable accuracy in identifying the normal strains in the HCB elements under the service loads and is comparable to very complex and time consuming FEM. Moreover, the modified methodology is as simple as the current one and suits the daily design. However, it is clear that this methodology is applicable only to the

service loads and its applicability to the ultimate strength design of the HCB needs to be experimentally verified.

The results of this study suggest that during the flexural design of the HCB, it is important to study the stresses at two sections, the midspan and the end of the beam, rather than the midspan only. They suggest also including the bearing stiffness effects during the design of the HCB in bridge applications. Since the bearing stiffness is time-temperature dependent, it may be advisable to design two cases that include two extreme values for the temperature and aging parameter (C in equations 6-3 and 6-4) that are expected to take place during the lifetime of the bridge (for example 1 and 50 based on Roeder et al. (1989)). The lower C value will cause maximum stresses at the midspan, while the larger value will cause the maximum stresses at the end of the beam.

6.8. SUMMARY AND CONCLUSIONS

Based on the results of the FEA of the first HCB bridge constructed in Missouri (B0439), this chapter examined the current flexural design methodology and assumptions. This was achieved by instrumenting one of B0410 HCBs with different sensors. The strains induced in the beam elements during different loading stages were recorded. A FEM was developed for B0410 superstructure using ANSYS V14.0. The strains were also estimated using the current design methodology and a modified methodology.

The linear FEA was found accurate in predicting the normal stresses of the HCB under the service loads. The FEM clarified that the polyiso foam works as flexible shear connection and achieves partial composite action between the different elements of the HCB resulting in differential displacement between them. Consequently, the different components at the same level have different strains. The current design methodology was found unable to predict the maximum compressive stress in the concrete arch because the procedure ignores the restrained moments at the beam-pads interface and the curved shape of the beam. The results suggested that the HCB has no perfect beam behavior. The tied arch and the relative movements between its elements affect its behavior.

A modified procedure was developed. The methodology accounted for the effect of the tied arch by modeling HCB as curved beam rather than straight one, and by including the effect of the tie (the tension reinforcement) in the stiffness of the springs that simulate the bearing pads. However, the proposed algorithm ignores the partial composite action between the HCB elements and is based on the same assumptions as the existing one. The methodology was found to achieve significant enhancement in predicting the normal strains in the different

elements of the HCB. The results obtained by the modified procedure suggest that it is acceptable, during the flexural design of the HCB, to ignore the relative movements between the HCB components and assume strain compatibility between them. The proposed methodology was examined using service loads. Future work should investigate the applicability proposed within to the design of the ultimate flexural strength of the member.

7. DURABILITY OF HCB

7.1. Introduction

The main concept of the HCB is to acquire its strength and stiffness mainly from less expensive construction materials (i.e. steel and concrete), while the environmental protection is provided by a relatively more expensive, however, more durable material (i.e. GFRP composite). Subsequently, the composite shell must possess not only sufficient strength and stiffness to withstand the self-weight and applied loads, but also relevant physical and in-service properties that can endure the aggressive environmental conditions into which the girder may be placed. These properties are of primary importance in relation to the durability of the FRP composite shell and hence of the HCB as a whole.

Infrastructure systems are exposed to different weathering conditions during their life cycle, including: freeze-thaw cycles, high temperature, high relative humidity, aqueous solution exposure (such as salt water results from using deicing salts), chemical agents, UV irradiation and combinations of previously mentioned conditions. Consequently, the performance of the commercial E-glass fiber/vinylester used to encase the HCB elements under these natural weathering needs to be tested. Another effect that needs to be investigated regarding the long-term behavior of the FRP composite is the creep rupture. Since, polymers are viscoelastic materials, they exhibit creep and stress relaxation to a great extent (DA., 1991). As a result, FRP composites are more susceptible to creep than traditional construction materials, especially under the influence of moisture and temperature (Franke & Meyer, 1992).

In the current study, four different aging regimes were used to test the durability of the GFRP shell, and subsequently the durability of the HCB as whole. The exposure regimes were selected to match the actual service environment of HCB bridges in Missouri. In the first conditioning regime, GFRP specimens were subjected to continuous salt fog exposure for 3072 hr. (128 days). The second exposure regime consisted of 350 different thermal cycles in conjunction with sustained stresses. The thermal cycles started with 50 freeze-thaw cycles and followed by alternating high temperature and high relative humidity (RH) cycles (150 cycles each). The sustained stresses were applied using two different weights applied to the longitudinal and transverse directions of the specimens. The sustained stress levels ranged from 2.3% to 7.4% of the ultimate tensile strength of the specimens. The third and fourth aging regimes are still under implementation. The third one consists of UV-irradiation

exposure for 3072 hr., followed by 6000 hr. of salt fog exposure (for a total of 378 days). The last regime includes applying the same levels of sustained stresses used in the second regime, however, for longer period (225 days). The sustained stresses are applied along with indoor ambient controlled weathering, and outdoor natural weathering.

7.2. EXPERIMENTAL PROGRAM

7.2.1. Specimen Details

Four GFRP panels, which are similar to the shell webs used in B0439 HCBs, were provided by Harbor Technologies Inc. The panels consisted of the following layers (listed from the outside surface) : a layer of surface veil, a layer of continuous flow media (CFM), a layer of off-axis knit fabric with +/- 45 degree plies (with commercial name; E-BXXS 2410), and a layer of quad knit fabric with 0, 90 and +/-45 degree plies (with commercial name; E-QX 10200). The veil and CFM layers facilitate the resin transfer and provide a resin rich layer on the outside perimeter of the beam shell. These layers were not factored into the design calculations. The E-BXXS 2410 layer is 0.03" thick and weights 34.6 oz/yd^2. The fiber content, by weight, in this layer is 70%, oriented equally by +/- 45º angles. While the E-QX 10200 layer is 0.08-in. thick and weights 101 oz/yd^2. The fiber content, by weight, in the E-QX 10200 is 68%. 50% of these rovings are oriented in the warp direction (0º), in the current work this direction is referred to as longitudinal direction. 14% are oriented in the fill (crosswise) direction (90º), in the current work this direction is referred to as transverse direction. The remaining fibers are equally oriented by +/- 45º angles.

Three types of resins (CCP Stypol 040-8086, CCP Stypol 040-8084, and Arpol RTM 80545-45) are generally used to infuse HCBs in different projects. The matrix used to infuse the glass fabrics of B0439 was CCP Stypol 040-8086. CCP Stypol 040-8086 is a Bisphenol-A, epoxy vinylester resin that is generally combined with styrene to lower the viscosity for infusion. The resin contained a pigment that included inhibitors for ultraviolet (UV) irradiation. Moreover, the veil and CFM layers provided an extra layer for UV protection. Panels, number 3 and 4, were painted by post-applied gel coat comprised of a UV inhibiting paint. This paint has been roller applied to the exterior surfaces of the fascia HCBs of B0439 (Hillman, 2012).

The four panels were cut into 96 coupon specimens in the longitudinal and transverse directions using the water jetting technology. It was not clear if the four panels were identical or had slight differences such as the infusion with different types of resin. Consequently, six specimens (3 in the longitudinal direction and 3 in the transverse direction) from each panel

were used as control specimens, with a total of 24 control specimens. 36 specimens were subjected to the first two aging regimes, and 36 specimens are currently exposed to the third and fourth regimes.

Although the standard test method D3039/D3039M (ASTM, 2008) for identifying the tensile properties of FRP composites recommends using rectangle-shaped specimens, dumbbell-shaped specimens were used in the current work. The selection of the dumbbell shape aimed to force the failure to take place within the narrow region and avoid the failure within the grip region as experienced in similar tests performed by the corresponding author. Before cutting the 96 specimens, four specimens were cut with the dimensions shown in Figure 7-1. The four specimens were then subjected to tensile stress up to failure. The failure was found to take place in the narrow region of the four specimens. Subsequently, all the coupons were cut with the same shape and dimensions as the four specimens. To prevent gripping damage, aluminum tabs were adhered to the coupon ends as graphically demonstrated by Figure 7-1. The 60 specimens were always found to fail in the narrow region. A sample of the failure locations in different specimens is illustrated in Figure 7-2.

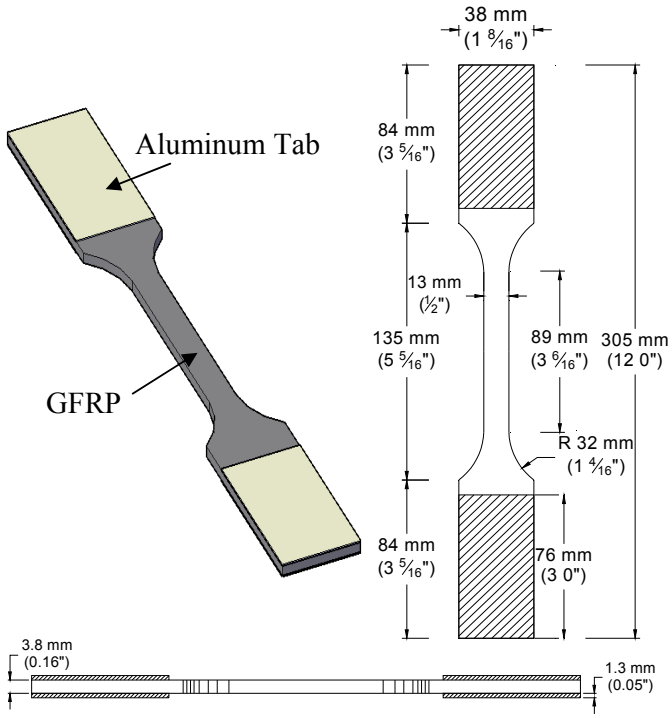

Figure 7-1 Dimension of FRP Specimens

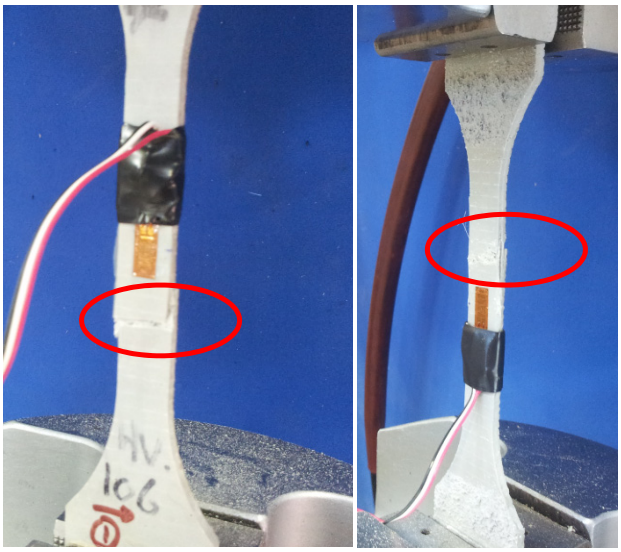

Figure 7-2 Failure Locations in Dumbbell-Shaped GFRP

7.2.2. Aging Regimes

7.2.2.1 Salt Fog Exposure

Twelve specimens were exposed to continuous salt fog cycles for 3072 hours (128 days) following ASTM B117 in the apparatus shown in Figure 7-3. The twelve specimens were taken from panels 2 and 4 (3 in the longitudinal direction and 3 in the transverse direction from each panel). In each cycle, the salt solution is atomized into fine mist as follow: compressed air streams through a tube, which is partially full of hot deionized water, creating hot-humid air. A salt solution contains 5% Sodium Chloride (Nacl) moves from holding tank to a nozzle. When the hot-humid air and salt solution mix at the nozzle, the later is atomized into corrosive fog. The temperature of the chamber was kept during the test at 95 °F via chamber heaters.

Figure 7-3 Slat Fog Apparatus (Left image)
GFRP Specimen Exposed to Salt Fog (Right image)

7.2.2.2 Thermal Cycling and Sustained Stress Regime

Twenty-four specimens were subjected to sustained stresses, for 75 days, in conjunction with a series of thermal cycles in a computer-controlled chamber to simulate seasonal effects in the mid-west United States. The specimens were taken from panels 1 and 3 (6 in the longitudinal direction and 6 in the transverse direction from each panel). The thermal and RH cycles are graphically illustrated by Figure 7-4.

The specimens in the environmental chamber were subjected first to 50 freeze-thaw cycles. The temperature went from -4ºF to 50ºF during these cycles to simulate the winter season effects. Then, the summer season effects were simulated by three identical groups of 50 high temperature cycles alternated with three different groups of 50 high relative humidity (RH) cycles for a total of 300 cycles. The temperature during the high temperature cycles changed from 68ºF to 122ºF. In the first 50 RH cycles, the RH varied between 60% and 95% at a constant temperature of 68ºF to simulate the humidity and rain during nighttime. The second group of RH cycles simulated the humidity and rain during daytime. During this group, the RH varied between 60% and 95% at a constant temperature of 77ºF. The third group of RH cycles, simulated the heat that may emit from the bridge deck during raining causing the nearby air temperature to actually rise to a higher level, so RH varied from 60% to 95% at a constant temperature of 104ºF. Table 7-1details the temperature and humidity information for each conditioning cycle along with the total number of cycles to which the specimens were exposed.

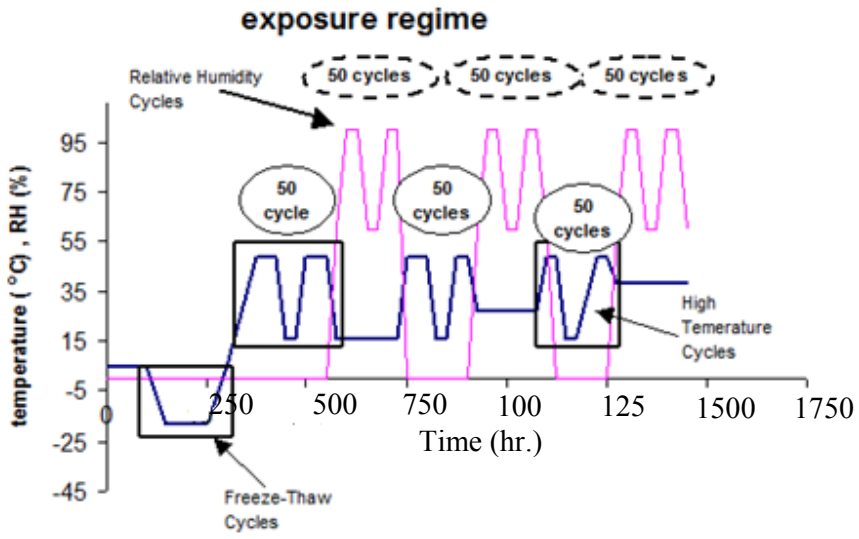

Figure 7-4 The Environmental Chamber Exposure Regime

Table 7-1 Environmental Chamber Conditioning Cycles

Conditioning Cycles	Conditioning Extreme Limits	Number of Cycles
(Freeze- Thaw) cycles	-4ºF to 50ºF	50
(High temperature) cycles	68ºF to 122ºF	150
(Relative Humidity) cycles	60% RH to 95% RH at 68ºF	50
(Relative Humidity) cycles	60% RH to 95% RH at 77ºF	50
(Relative Humidity) cycles	60% RH to 95% RH at 104ºF	50

In each cycle, the conditioning was kept for 2 hours at the upper limit, followed by 30 minutes ramp to the lower condition limit. Then, 2 hours hold at the condition lower limit was executed and followed by 30 minutes ramp to the upper limit for a total of 5 hours for each cycle.

In order to apply sustained stresses to the FRP specimens, two holes were drilled at the top and bottom of the FRP coupons. Then, each specimen was hung to dwidag bar from its top and concrete block was attached to the bottom of the specimen. The concrete blocks had two different weights: heavy weight blocks with average weight equaled 106 lb and lightweight blocks that had an average weight of 55 lb. The heavy weight blocks achieved a stress level of about 4.4% of the ultimate tensile strength of the longitudinal specimens and about 7.4% of the ultimate strength of the transverse specimens. While the lightweight blocks presented stress levels of about 2.3% and 3.9% of the ultimate strength of the longitudinal and transverse specimens respectively. Figure 7-5 displays a sample of the FRP specimens subjected to sustained stresses in conjunction with environmental conditioning in the environmental chamber.

Figure 7-5 FRP Specimens Subjected to Sustained Stress
and Thermal Cycles in the Environmental Chamber

7.2.3. Tensile Strength Test

The tensile strength tests were performed using MTS880 test machine shown in Figure 7-6. The apparatus is a (50 kips) servo-hydraulic universal testing machine. The load was applied at a constant cross-head speed of 0.02 in/min. This head speed allowed all the specimens to break within 3 to 6 minutes. One vertical strain gauge was installed on each specimen in the direction of the applied load. During the tests, the load, displacement of the head, and strain were recorded simultaneously at 50 ms intervals using a data acquisition system. Figure 7-7 illustrates a sample of stress-strain curve for a GFRP specimen.

Figure 7-6 Tensile Coupon Test for FRP Specimen
via MTS880 Universal Testing Machine

Figure 7-7 shows slight nonlinearity in the stress-strain curve of the GFRP specimen. It is common that the woven composites exhibit nonlinear behavior under tension due to matrix microcracking. Due to this nonlinearity, the Young's modulus was taken, for all the specimens, as the slope of the stress-strain curve in the strain range from 1000 to 3000 $\mu\varepsilon$ (micro strain) as recommended by D3039/D3039M (ASTM, 2008).

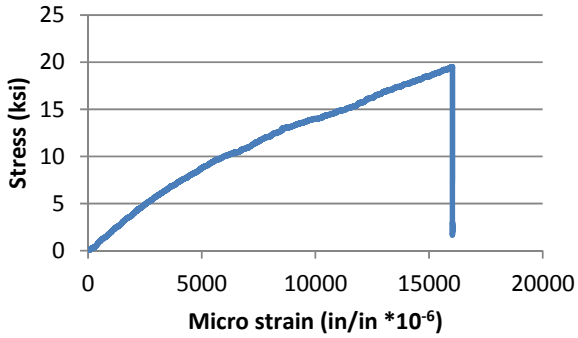

Figure 7-7 A Sample for Stress-Strain Curve of a GFRP Coupon

The figure also clarifies that the first ply failure (FPF) immediately caused the ultimate laminate failure (ULF) or the final failure for the specimen. It should be noted that, in some cases the ULF occurred at higher loads than those of the FPF. In this study, the durability of the GFRP composite was evaluated in terms of the reduction in the ultimate tensile strength (i.e. ULF) of the control specimens. While the change in the FPF stress due to the aging regimes was not studied.

7.3. DAMAGE MECHANISMS

The damage mechanisms that may result from the different environmental conditions, included in this study, are briefly discussed in the following sections.

7.3.1. Moisture and Salt Effects

The primary effect of moisture is on the resin itself. Moisture permeates into all organic polymers, leading to reversible and irreversible changes in the polymer structure due to setting up mechanisms such as plasticization, saponification, or hydrolysis (Karbhari et al., 2003, Hollaway, 2010). The rate of the moisture uptake and the total amount absorbed of water are controlled by several factors such as the chemical structure of the polymer, the

cross-linking agent, the temperature, and the relative humidity (Wright, 1981). The absorption of water results in dimensional changes, generates internal stresses, and may reduce the glass transition temperature, T_g. Consequently, the absorption of water causes changes in the mechanical, chemical, and physical properties of the polymers.

Moisture has also shown to cause degradation to glass fibers. Though glass fibers are relatively impervious to water, the degradation mechanism is initiated by moisture-extracting ions from fiber; that way, changing the polymer structure. In some cases, the moisture may cause deleterious effects to the matrix-fiber interface. Previous studies showed that the vinyl ester resins has the less water absorption in comparison to epoxies and polyesters (Balázs & Borosnyói, 2001, Waldron et al., 2001).

Generally, the diffusion of water into the composite decreases when electrolytes (such as sodium and chloride ions from salt) exist in the water. However, the glass fibers high surface area to weight ratio make them more prone to the chemical attack. The chloride ions attack and dissolve the E-glass fibers and subsequently reduce the tensile strength of the GFRP.

7.3.2. Freeze-Thaw Cycles Effect

At low temperature, the polymeric matrix becomes stiffer. Subsequently, the composite behavior that is matrix dominated, such as the torsional stiffness, will improve. However, the polymeric resin coefficient of thermal expansion is generally an order of magnitude higher than that of the fiber. This significant mismatch can induce, at low temperatures, stresses in the matrix high enough to initiate the formation of microscopic cracks. When these cracks develop to a certain density and size, they will tend to coalesce to form macroscopic matrix cracks which diffuse in the resin or stroll around the matrix-fiber interface (Wang, 1986).

Hahn (1976) deduced a formula to estimate the longitudinal residual stresses in the matrix, σ_{mL}, of the unidirectional composite due to the thermal changes as follows:

$$\sigma_{mL} = \left(V_f E_f E_m\right)\left(\alpha_f - \alpha_m\right)\left(T - T_0\right)\Big/\left(V_f E_f + V_m E_m\right) \tag{6.1}$$

where V is the volume fraction, E is the elastic modulus, α is the coefficient of thermal expansion, T is the temperature, T_0 is the stress-free temperature, which is usually assumed

the curing temperature of the composite, and the subscripts m and f refer to the matrix and fiber respectively.

The equation proposed by Hahn illustrates that as the composite cools, higher tensile stress induces in the matrix of the unidirectional composite. Dutta and Hui (1996) clarified that at very low temperatures the induced stresses may approach the ultimate matrix tensile strength. They also suggested that the resin type and the curing process control the thermal cycle response. Studies showed that the low temperature cycles accentuate the residual stress effects. As the number of thermal cycling increases, the number and severity of polymer cracks in the composite increase (Dutta, 1988).

7.3.3. High Temperature Cycles Effect

The influence of temperature change on the polymeric matrix can be divided into short-term (temporary) effects and long-term (permanent) effects. The temporary effects are usually physical and reversible when the temperature returned to its original state. The permanent effects generally result from irreversible chemical reactions and are referred to as aging (Hollaway, 2010).

High temperatures that are close to the polymer glass transition temperature, T_g, may free volumes, which can be filled by other molecules as the matrix tries to reach equilibrium stage. Subsequently mechanical properties of the composite may change at these temperatures (Silva & Biscaia, 2008). Vitrification of the polymer may also take place at high temperatures. This phenomenon is an early form of decomposition of the matrix where the material become amorphous (Caceres et al., 2002). Another phenomenon that may occur at higher temperatures is hydrolysis decomposition of the molecular structure of the polymer, which is harsh form of plasticization.

It is worth mentioning that the thermal exposure does not always harm the FRP elements, especially as long as the temperature is significantly below the T_g of the matrix. It is common for the manufactured resin not to be fully cured. In some cases, the high temperature results in beneficial post cure of the resin. This post cure increases the cross-linking of the polymer and thus increases the strength of the polymeric molecular structure.

7.3.4. Sustained Stress Effect

When, sustained stress is applied to FRP composite, the composite strength decreases with time. After certain time of the exposure to the sustained stress, it can fail suddenly. This

failure, which results from the degeneration of the material mechanical properties with time, is referred to as creep-rupture. While, the duration of time up to failure is referred to as the endurance time (ACI 440.2R-08).

As the ratio of the sustained tensile stress to the short-term strength of the FRP laminate increases, endurance time decreases. It is also well established that the different environmental conditions such as freeze-thaw cycles, high temperature, wet and dry, UV radiation exposure, or high alkalinity can accentuate the creep effect and decrease the endurance time (ACI 440.2R-08).

7.4. RESULTS AND DISCUSSION

Table 7-2 compares between the average ultimate tensile strength of the control specimens and the specimens subjected to salt fog cycles. The table also lists the standard deviation (σ) and the percentage change of the ultimate strength.

Table 7-2 Tensile Strength of Control and Salt Fog Specimens

Panel	Control		Salt Fog		
	Tensile Strength ksi	σ (ksi)	Tensile Strength ksi	σ ksi	Change %
2 L	43.15	2.33	43.42	1.83	+ 0.6
2 T	24.73	2.80	23.66	0.51	-4.3
4 L	41.88	2.65	39.66	2.19	-5.3
4 T	24.71	2.12	23.83	1.19	-3.6

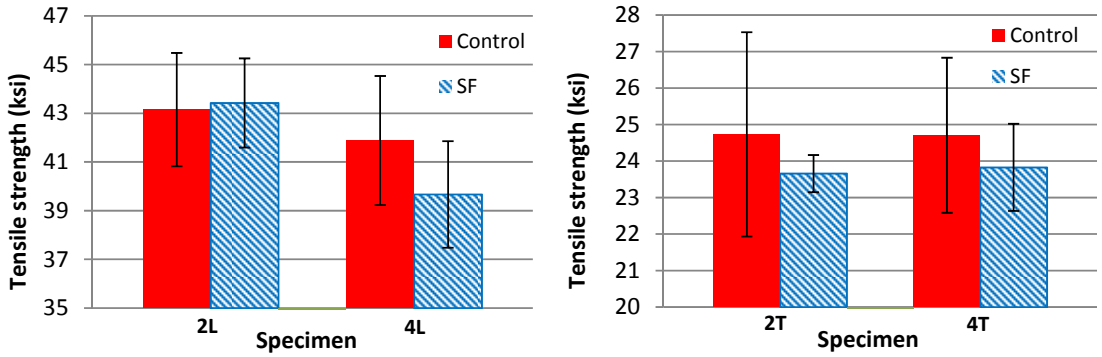

(a) (b)

Figure 7-8 Tensile Strength of Control and Salt Fog

The comparison is also graphically demonstrated by Figure 7-8. Figure 7-8-a illustrates the results of the specimens taken from panels 2 and 4 in the longitudinal direction, while Figure 7-8-b illustrates the results of the specimens taken from the same panels in the transverse direction. In these figures, the black bar presents the standard deviation of the strength. Variability of the test results can be attributed to the quality of laminate manufacture, such as, percentage of voids and resin-rich areas. The macroscopic photos presented in Figure 7-9, illustrate the different percentage of voids in three control specimens taken from panel 2.

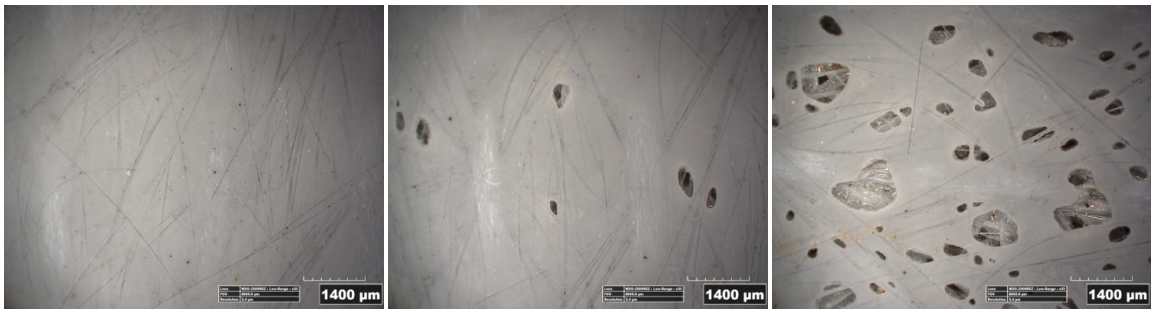

Figure 7-9 Different Percentage of Voids in Control Specimens

The results clarify that the maximum degradation in the laminate strength due to 3072 of continuous salt fog exposure was 5.3%. This reduction took place in specimens 4L (the highest percentage of fibers were in the load direction). The strength reductions of the longitudinal and transverse specimens were found close to each other. This result suggests that fiber degradation happened due to the salt fog exposure, because if only matrix degradation took place, the transverse specimens would be expected to suffer higher strength reductions. Figure 7-10 clarifies the attack of the sodium chloride (salt) particles to the fibers through the existing voids.

Only specimens 2L did not suffer strength reduction due to the salt fog exposure. This can be attributed to the high degree of cross-linking of the polymer, low percentage of voids, in these specimens relative to the other exposed ones. The low percentage of voids of 2L specimens relative to 2T specimens was observed by naked eyes. It is expected that, the high density of cross-linkages decreased the permeability and subsequently the diffusion of the light atomic weight free ions into the composite. This result also suggests that the quality control during manufacture process not only largely controls the strength property of composites, but also may affect their endurance to the environmental effects. It is also not rolled out that the temperature during the salt fog exposure resulted in polymer post cure that decreased the effect of the salt fog on the exposed specimens.

Panel 2 specimens were found to achieve an average weight increase by 6.3% due to the water absorption, while panel 4 specimens were found to gain additional weight equals 6% of the original weight. It is expected that this moisture uptake was reduced by the large ions in the salt as it is shown in Figure 7-10 and was concluded by d'Almeida (1991). The results also showed that the coated and uncoated specimens (panels 4 and 2 respectively) suffered the same levels of strength change due to the salt fog exposure. This was expected, since the post-applied gel mainly aims to reduce the UV irradiation effects.

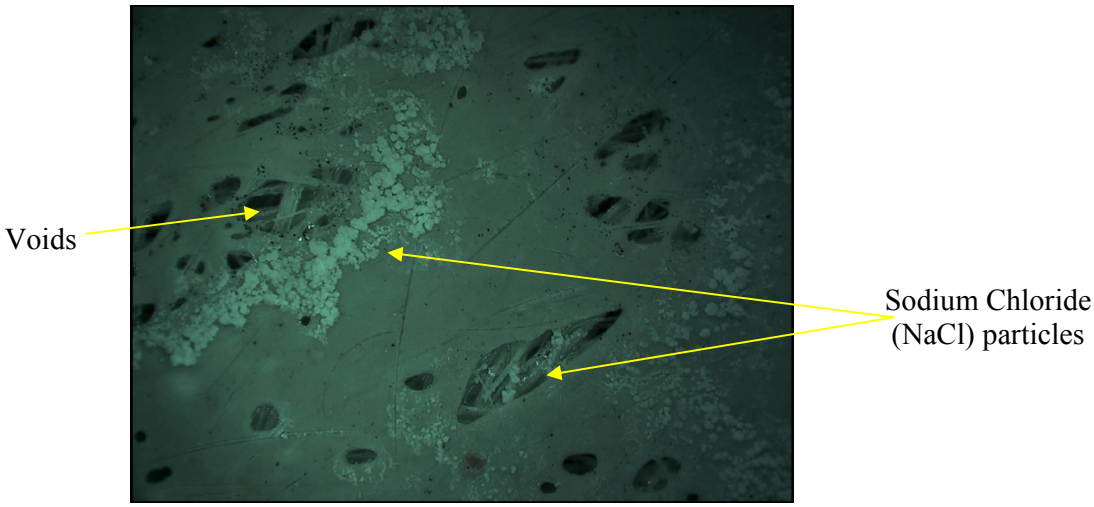

Figure 7-10 Microscopic Photo for Specimen Subjected to Salt Fog

Table 7-3 compares between the average tensile elastic modulus (E^{+}) of the control specimens and salt fog specimens. The maximum reduction in the Young's modulus was found 13%, which is significantly larger than the reduction in the tensile strength. The results also demonstrate that there is no correlation between the change in the specimens' tensile strength and stiffness due to this period of salt fog exposure. In some cases when the stiffness increased, the strength decreased and vice versa, such as 2L and 4T specimens.

In general, the results obtained after 3072 hr. of salt fog exposure, indicate that the commercial GFRP used in the HCB bridges constructed in Missouri, has good resistance to the salt fog effects. The reductions of the tensile strength and stiffness due to this period of exposure were small and almost within the normal scatter of the data. Consequently no decisive conclusions regarding the damage mechanism can be drawn.

Table 7-3 Young's Modulus of Control and Salt Fog Specimens

Panel	Control		Slat Fog		
	Young's Modulus (E^+) (ksi)	σ (ksi)	Young's Modulus (E^+) (ksi)	σ (ksi)	Change %
2 L	4411.8	320.1	3839.7	28.2	-13.0
2 T	2043.3	204.6	1989.1	141.7	-2.7
4 L	4219.0	19.8	4048.0	381.5	-4.1
4 T	2075.6	110.3	2172.9	260.9	+4.7

Table 7-4 and Figure 7-11illustrate the ultimate tensile strength and the standard deviation of the control specimens of panels 1 and 3, and the specimens subjected to the environmental conditioning cycles along with sustained stresses in the environmental chamber. In both of them, the abbreviation EC refers to the environmental chamber, and HW and LW refer to heavy weight blocks and lightweight blocks respectively.

Table 7-4 Tensile Strength of Control and Environmental Chamber Specimens

Panel	Control		EC-HW			EC-LW		
	Ten.Str. (ksi)	σ (ksi)	Ten.Str. (ksi)	σ (ksi)	Change %	Ten.Str. (ksi)	σ (ksi)	Change %
1 L	47.45	1.30	47.59	0.41	+0.3	47.86	1.54	+0.9
1 T	24.71	1.01	23.17	1.33	-6.2	23.62	1.94	-4.4
3 L	43.16	4.43	44.03	0.74	+2.0	47.45	1.38	+10.0
3 T	27.67	0.50	26.50	1.05	-4.3	26.61	0.67	-3.8

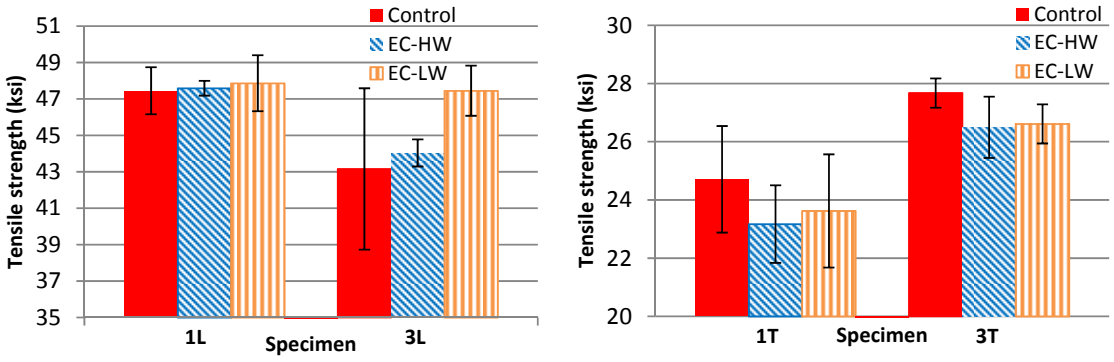

Figure 7-11 Tensile Strength of Control and EC Specimens

The results show that the specimens subjected to sustained stress via the heavy weight blocks always had lower tensile strengths than those of the specimens subjected to sustained

stress by the lightweight blocks. Even when an increase of the strength of the exposed specimens occurred, the same behavior was noticed. This indicates that, in spite of the relatively short period and the low levels of the sustained stress, its effect on the tensile strength was present.

The results also clarify that, the longitudinal specimens gained extra strength due to the thermal cycling along with the sustained stress exposure, with a maximum tensile strength increase equals 10% of the original strength. While the transverse specimens, suffered strength loss with maximum decrease equals 6.2% of the original strength. These results possibly point to several competing mechanisms resulted from the exposure regime. As it is mentioned earlier, it is common that the manufactured polymer be less than 100% cured. In this case, the high temperature cycles may achieve residual cross-linking and enhance the resin properties. On the other hand, the more under-cured the resin, the more vulnerable it is to the moisture damage and the greater degree of plasticization. The desirable high temperature can also increase the moisture absorption. Moreover, the under-cured resin is more susceptible to creep and stress relaxation effects, while the post-cure enhances the creep susceptibility. Therefore, it is possible that the polymer was post cured and plasticized simultaneously leading to complications in the creep effects and the strength degradation behavior. It is also well established that the creep effects are dominated by the matrix dependent properties rather than the fiber or interfacial properties (Karbhari et al., 2003). Consequently, it is possible that the sustained stresses had significant effect on reducing the tensile strength of the transverse specimens due to the low percentage of fibers oriented in the direction of the sustained load. While the creep effect on the longitudinal specimens was insignificant.

Table 7-5 compares the average tensile elastic modulus (E^{+}) of the control specimens and environmental chamber specimens. In all cases except (1T-EC-LW) the young's modulus was increased with a maximum increase equals 15.9%. Likewise, the results obtained due to the salt fog exposure, the results of the chamber exposure, demonstrate that there is no correlation between the change in the specimens' tensile strength and stiffness due to this period of the environmental conditioning exposure.

Table 7-5 Young's Modulus of Control and Environmental Chamber Specimens

Panel	Control		EC-HW			EC-LW		
	E^+ (ksi)	σ (ksi)	E^+ (ksi)	σ (ksi)	Change %	E^+ (ksi)	σ (ksi)	Change %
1 L	4040.1	317.4	4433.7	289.2	+9.7	4357.07	294.11	+7.8
1 T	2013.0	92.1	2332.1	232.5	+15.9	1905.80	133.19	-5.3
3 L	4169.3	264.3	4282.1	124.9	+2.7	4246.70	83.68	+1.9
3 T	2280.7	133. 5	2389.0	68.6	+4.8	2306.13	233.82	+1.1

The results also suggests that the commercial E-glass fiber/vinylester tested in this study has good endurance to the seasonal weather in Missouri along with levels of sustained stresses ranged from 2.3% to 7.4% of the ultimate tensile strength of the composite.

7.5. SUMMARY AND CONCLUSIONS

During this chapter, the durability of the outer composite shell that encapsulates the HCB elements was examined. The laminated shell is comprised of two plies of woven E-glass reinforcing fabric infused with a vinylester resin matrix. The durability of the commercial GFRP laminate was examined via two aging regimes. In the first regime, the GFRP specimens were subjected to continuous salt fog exposure for 3072 hr. In the second regime, the specimens were subjected to sustained stress in conjunction with 350 thermal cycles in a computer-controlled environmental chamber. The thermal cycles included 50 freeze-thaw cycles, 150 high temperature cycles, and 150 high relative humidity cycles. The 350 cycles simulated the natural seasonal weathering in mid-west United States. Tensile coupon test was applied to the control and tested specimens in the warp (longitudinal) direction and the fill (transverse) direction of the laminated shell. The following conclusions were obtained:

- The maximum reduction in the ultimate tensile strength of the GFRP shell in both directions (the warp and fill) due to the salt fog exposure was 5.3%. While the maximum strength degradation, due to the thermal cycles along with the creep effect, was 6.4%. These results clarify that the GFRP shell, and subsequently the HCB as a whole, has excellent durability in relation to the expected weathering exposures in Missouri.
- The results of the salt fog exposure indicated that the strength reduction occurred due to fiber degradation. While the environmental chamber regime results pointed to

several competing mechanism such as residual cross-linking along with resin plasticization. However, the reductions in the tensile strength that resulted from the two aging regimes were insignificant and can be attributed to the experimental errors or the manufacture quality control. Consequently, the conclusions about the damage mechanism are not definite.

- In both exposure regimes, there was no correlation between the change in the specimens' tensile strength and elastic modulus.
- The post-applied gel did not provide any advantage to the coated specimens in the cope with the salt fog exposure. This was expected, because the function of this coating layer is to reduce the UV radiation effects. In the second exposure regime, the specimens were prone to the thermal cycles effects from both sides. Consequently, the effect of the applied gel in resisting this conditioning regime cannot be evaluated. However, it is expected that the gel will not increase the endurance to these thermal cycles.

8. SUMMARY, CONCLUSIONS AND RECOMMENDATIONS

8.1. SUMMARY

A new type of the HCBs was recently used to construct three bridges (B0439, B0410, and B0478) in MO, USA. The HCB consists of a self-consolidating concrete (SCC) arch that is tied at the ends using high-strength galvanized steel strands. The concrete and steel, which represent the compression and tension reinforcement respectively, are encased inside a durable fiberglass composite shell. Due to this unique configuration, the fiberglass box protects the steel and concrete from the environmental effects and serves as the formwork for the concrete arch, while the strength and stiffness are provided by an efficient use of the steel in purely axial tension, and the concrete in purely axial compression. In addition to the optimization of load carrying behavior offered by this configuration, it results in a lightweight member that can be transported easily and erected rapidly making this technology well suited to Accelerated Bridge Construction (ABC).

Because of the novelty of the HCB and its vague structural behavior, the Missouri Department of Transportation (MoDOT) entrusted an exploratory program to Missouri University of Science and Technology (MS&T) in cooperation with University of Missouri-Columbia (UMC) to evaluate the in-service beam behavior. The program consisted of four main phases. The first phase that included QC/QA tests was executed by research teamwork from MS&T and research teamwork from UMC. While the other phases (finite element modeling of HCB bridge superstructure, investigation of the HCB's flexural behavior, and assessment of HCB durability performance), were accomplished by MS&T researchers.

The first phase included QC/QA testing program. The program started with constructing a mock-up beam that simulated B0439 HCBs. The mock-up beam included see-through Plexiglas in place of one of the shell webs. This allowed the visual monitoring of the flow of the SCC through the constricted arch cavity. During the construction of the three bridges, standard compressive strength and j-ring tests were performed on the SCC that was used to form the HCBs arches. The maturity of the SCC was verified by recording the thermal changes of the concrete after the pour of B0439 and B0410 arches. The program incorporated also a review of the potential damage modes for the HCB members, and an assessment of the available inspection technologies. Methods for implementing thermal images to address the potential for voids in the concrete arch were developed, tested and verified during the course of the testing. This technology successfully detected voids in the

arch section during the casting of the arch for bridge B0410. The approach developed was innovative and capitalized on the heat of hydration generated during the curing of the concrete. As such, IR imaging is an ideal solution for QC/QA of the concrete arch concrete placement.

To achieve the second and third phases' goals, a series of load tests was performed on the three bridges after their construction. The elements of one of B0410 HCBs have been instrumented with different sensors. Mathematical calculations were performed along with FEA to estimate the deflections along the HCBs and the strains in their different elements. During the second phase, the first FEA for a HCB bridge superstructure was accomplished. Two FEMs were constructed for B0439 superstructure via ANSYS V13.0 and SAP2000 V14.0. This FEA provided better understanding for the HCB behavior and highlighted the areas that need more examination. In the third phase, A FEM was developed for B0410 superstructure using ANSYS V14.0. The current flexural design methodology was examined. The flexural behavior of the HCB was analyzed in detail and a modified design methodology was proposed.

The last phase studied the durability of the HCB. During this phase, GFRP specimens were subjected to four environmental conditioning regimes. Two of the exposure regimes were completed, while the other two are still under completion. The first aging regime included exposure to salt fog cycles. In the second regime, the GFRP specimens were subjected to sustained stress in conjunction with thermal cycles that simulated the seasonal effects in mid-west United States. The third conditioning regime includes the exposure to UV radiation that will be followed by salt fog cycles. In the fourth exposure regime, specimens will be subjected to sustained stress for longer period together with outdoor natural weathering environment effects and controlled indoor environment.

8.2. CONCLUSIONS

The results of the laboratory and field investigations accompanied by the mathematical analyses for the HCB bridges led to the following conclusions:

- Without the proper concrete rheology, the concrete arch is susceptible to voids formation during the concrete pour. The proposed Infrared thermal imaging technique presented herein is an ideal solution for detecting such voids and for QC/QA of the arch concrete placement. This technology can also be applied as a QC/QA tool to assess the workmanship of the composite construction.

- The HCB owns abundant nominal bending and shear strength to withstand the expected loads during its lifetime.
- The unique configuration of the HCB optimizes the load carrying behavior and maintains the gross section properties under the service loads.
- The FEMs of B0439 suggest that the single-web HCB may suffer lateral and rotational deformations under vertical loads, indicating that the single-web girder may have weak lateral and torsional rigidity.
- The shell webs are the most critical elements in shell. Attentiveness needs to be paid to their elastic buckling and shear stresses during the design process.
- The polyisocyanurate foam and the cross-ties contribute to the lateral stability of the FRP webs. However, the shell webs of B0410 HCBs suffered outward deformation during placement of the arch concrete. This indicates that the cross-ties might be overstressed similar to what was observed in a previous study (Snape & Lindyberg, 2009).
- The linear FEA is accurate in predicting the static behavior of HCB under the service loads.
- The existing flexural design methodology overestimates the stresses in the FRP shell and strands, and is unable to predict the maximum compressive stress in the concrete arch.
- The polyiso foam works as flexible shear connection and achieves partial composite action between the different elements of the HCB resulting in differential displacement between them. Consequently, the different components at the same level have different strains.
- The results of this work suggest that the HCB does not yield traditional flexural beam behavior. The tied arch and the relative movements between its elements affect its behavior.
- The proposed flexural methodology presented in this study achieve significant enhancement in estimating the normal strains in the HCB elements under the service loads. The methodology suggests that it may be acceptable to assume strain compatibility between the girder elements during the design process.
- The durability testing results clarify that the GFRP shell, and subsequently the HCB as a whole, has excellent durability in relation to the expected weathering

exposures in Missouri. Longer exposure regimes are under implementation to assure these results.

8.3. RECOMMENDATIONS FOR FUTURE RESEARCH

This section highlights the issues that are recommended to be addressed by future research to expedite the HCB as a commonly implemented technology. These issues can be summarized as follows:

- The accuracy of nonlinear FEA to predict the HCB behavior under ultimate loading needs to be tested.
- The ability of the proposed flexural design methodology to estimate the nominal bending capacity of HCB needs to be verified experimentally.
- The experimental investigation of the lateral deformation of HCB, especially the fascia girders, under vertical as well as lateral loads is recommended. The investigation of the rotational deformation under torsional moments is also advisable.
- In future experimental studies, strain gauges should to be placed throughout the composite HCB cross-section with gauges in the arch and on the shell at the same locations. This is essential for a better evaluation to the partial composite action effects especially under the ultimate loads.
- Neither this work nor the literature examined the existing shear design methodology, though the methodology seems superficial in depth. Testing the methodology, and probably developing more rigorous procedure, seems substantial.
- A sophisticated analysis methodology for the shell web-wrinkling needs to be developed.
- Due to the very thin shell layer that protects the prestressing strands form fire effects, the fire resistance of HCB is a logical concern and an issue that needs to be addressed.
- The effect of the lateral impact, which may result from an over-height truck, on HCB bridge stability needs to be studied.
- Progress on the development of practical tools for conducting MFL should be monitored, and this tool should be considered for long-term monitoring of corrosion damage for the prestressing strand within the HCB members.

BIBLIOGRAPHY

AASHTO-LRFD (2012). "Aashto lrfd bridge design specifications", American Association of State Highway and Transportation Officials Washington, DC.

AASHTO, LRFD (1996). "Standard specifications for highway bridges", American Association of State Highway and Transportation Officials Washington, DC.

AASHTO, LRFD (2012). "Aashto lrfd bridge design specifications", American Association of State Highway and Transportation Officials, Washington, DC.

ACI440.2R-08,(2008). "Guide for the design and construction of externally bonded frp systems for strengthening concrete structures." *American Concrete Institute, Farmington Hills, USA*,Vol. No.

ACI (2011). "Building code requirements for structural concrete (aci 318-11) and commentary", American Concrete Institute.

ACI, Committee 363 (1992). "State-of-the-art report on high-strength concrete". *ACI 363R-92*. Detroit, American Concrete Institute.

Ahsan, Shainur.(2012). "Evaluation of hybrid-composite beam for use in tide mill bridge", Virginia Polytechnic Institute and State University

Aref, Amjad J, et al.,(2005). "Analysis of hybrid frp-concrete multi-cell bridge superstructure." *Composite structures*,Vol. **69**, No. 3, pp. 346-359.

ASTM (2007). "Standard test method for detecting delaminations in bridge decks using infrared thermography. Standard astm d4788 - 03(2007)". West Conshohocken, PA, United States, ASTM International.

ASTM, D,(2008). "3039/d 3039m-07." *Standard test method for tensile properties of polymer matrix composite materials*,Vol. No.

Avdelidis, N. P. and Moropoulou, A.,(2003). "Emissivity considerations in building thermography." *Energy & Buildings*,Vol. **35**, No. 7, pp. 663-667.

Balázs, György L and Borosnyói, Adorján (2001). "Long-term behavior of frp". *Composites in Construction@ sA Reality*, ASCE.

Bangalore, G. S.(2002). "Nondestructive evaluation of frp composite members using infrared thermography", West Virginia University

Bank, Lawrence C (2006). "Composites for construction: Structural design with frp materials", John Wiley & Sons.

Caceres, Arsenio, et al. (2002). "Salt-fog accelerated testing of glass fiber reinforced polymer composites", DTIC Document.

Ciolko, A. T., Tabatabai, H. (1999). "Nondestructive methods for condition evaluation of prestressing steel strands in concrete bridges". *NCHRP Web Document*. Washington, D.C., Transportation Research Board

Clemena, G. G., Lozev, M. G., Duke, J. C., Sison, M. F. (1995). "Interim report: Acoustic emission monitoring of steel bridge members". Richmond, VA, Virginia Department of Transportation**:** 68.

Committee, ACI, et al. (2008). "Building code requirements for structural concrete (aci 318-08) and commentary", American Concrete Institute.

d'Almeida, JRM,(1991). "Effects of distilled water and saline solution on the interlaminar shear strength of an aramid/epoxy composite." *Composites*,Vol. **22**, No. 6, pp. 448-450.

DA., Dillard (1991). "Viscoelastic behavior of laminated composite materials. In: Reifsnider kl, editor. Fatigue of composite materials.". *Amsterdam*, Elsevier.

Deskovic, Nikola, et al.,(1995). "Innovative design of frp combined with concrete: Short-term behavior." *Journal of Structural Engineering*,Vol. **121**, No. 7, pp. 1069-1078.

Domone, PL,(2007). "A review of the hardened mechanical properties of self-compacting concrete." *Cement and Concrete Composites*,Vol. **29**, No. 1, pp. 1-12.

Dutta, Piyush K,(1988). "Structural fiber composite materials for cold regions." *Journal of Cold Regions Engineering*,Vol. **2**, No. 3, pp. 124-134.

Dutta, Piyush K and Hui, David,(1996). "Low-temperature and freeze-thaw durability of thick composites." *Composites Part B: Engineering*,Vol. **27**, No. 3, pp. 371-379.

Earley, Renee C., et al. (2013). "Early-age behavior and construction sequencing of hybrid composite beam (hc beam) bridges in missouri, USA". *FRPRCS-11 – 11th International Symposium on Fiber Reinforced Polymer for Reinforced Concrete Structures*, Guimarães, Portugal.

ElBatanouny, M. K., et al.,(2014). "Identification of cracking mechanisms in scaled frp reinforced concrete beams using acoustic emission." *Experimental Mechanics*,Vol. **54**, No. 1, pp. 69-82.

Franke, L and Meyer, H-J,(1992). "Predicting the tensile strength and creep-rupture behaviour of pultruded glass-reinforced polymer rods." *Journal of materials science*,Vol. **27**, No. 18, pp. 4899-4908.

Friis, EA, et al.,(1988). "Negative poisson's ratio polymeric and metallic foams." *Journal of Materials Science*,Vol. **23**, No. 12, pp. 4406-4414.

Gaydecki, P., et al.,(2007). "Inductive and magnetic field inspection systems for rebar visualization and corrosion estimation in reinforced and pre-stressed concrete." *Nondestructive Testing & Evaluation*,Vol. **22**, No. 4, pp. 255-298.

Ghorbanpoor, A. (1998). "Magnetic based nde of steel in prestressed and post-tensioned concrete bridges". *Structural Materials Technology III: An NDT Conference*. R. Medlock, Chase, S. San Antonio, TX, SPIE. **3400:** 343-347.

Ghorbanpoor, A., Borchelt, R., Edwards, M., and Abdel Salam, E. (2000). "Magentic-based nde of prestressed and post-tensioned concrete members - the mfl system". U.S.D.O.T. Washington, D.C., F.H.W.A.**:** 99.

Gibson, Ronald F (2011). "Principles of composite material mechanics", CRC Press.

Hahn, H Thomas,(1976). "Residual stresses in polymer matrix composite laminates." *Journal of Composite Materials*,Vol. **10**, No. 4, pp. 266-278.

Hayes, Michael David.(2003). "Structural analysis of a pultruded composite beam: Shear stiffness determination and strength and fatigue life predictions". Doctor of Philosophy in Engineering mechanics *Dissertation*, Virginia Polytechnic Institute and State University

Hillman, J.R. (2012). "Hybrid-composite beam (hcb®) design and maintenance manual", The Missouri Department of Transportation.

Hillman, John R,(2003). "Investigation of a hybrid-composite beam system." *High Speed Rail IDEA Program", Transportation Reserch Board of National Acadamies, Chicago*,Vol. No.

Hillman, John R (2008). "Product application of a hybrid-composite beam system".

Hillman, John R. (2012). "Hybrid-composite beam (hcb®) design and maintenance manual", The Missouri Department of Transportation.

Hognestad, Eivind,(1951). "Study of combined bending and axial load in reinforced concrete members."Vol. No.

Hollaway, LC,(2010). "A review of the present and future utilisation of frp composites in the civil infrastructure with reference to their important in-service properties." *Construction and Building Materials*,Vol. **24**, No. 12, pp. 2419-2445.

Hutton, P. H., Skorpik, J. R. (1978). "Acoustic emission methods for flaw detection in steel highway bridges". Washington, D.C., Federal Highway Administration**:** 58.

John R. Hillman, PE, SE (2012). "Hybrid-composite beam (hcb) design and maintenance manual". HCB, Inc. **Bridge No. B0439 - MO 76 over Beaver Creek Jackson Mill, MO:** 37.

Kachlakev, Damian, et al. (2001). "Finite element modeling of reinforced concrete structures strengthened with frp laminates". *Final Report SPR*. **316:** 2001.

Karbhari, V.M.,(2001). "Materials considerations in frp rehabilitation of concrete structures." *Journal of Materials in Civil Engineering*,Vol. No., pp. 90-97.

Karbhari, V.M., Chin, J.W., Hunston, D., Benmokrane, B., Justka, T., Morgan, R., Lesko, J.J., Sorathia, U., Reynaud, D.,(2003). "Durability gap analysis for fiber-reinforced polymer composites in civil infrastructure." *Journal of Composites for Construction*,Vol. No., pp. 238-247.

Karbhari, VM, et al.,(2003). "Durability gap analysis for fiber-reinforced polymer composites in civil infrastructure." *Journal of Composites for Construction*,Vol. **7**, No. 3, pp. 238-247.

Keller, Thomas,(2002). "Overview of fibre-reinforced polymers in bridge construction." *Structural engineering international*,Vol. **12**, No. 2, pp. 66-70.

Khayat, KH,(1999). "Workability, testing, and performance of self-consolidating concrete." *ACI Materials Journal*,Vol. **96**, No., pp. 346-353.

Kosnik, D. E., Hopwood, T., Corr, D.J. (2010). "Acoustic emission monitoring for assessment of steel bridge details". *Review of Progress in Quantitative Non-Destructive Evaluation*, San Diego, CA, American Institute of Physics.

Krause, H. J., et al.,(2002). "Squid array for magnetic inspection of prestressed concrete bridges." *Physica C: Superconductivity*,Vol. **368**, No. 1-4, pp. 91-95.

Lachemi, Mohamed, et al.,(1997). "Early-age temperature developments in a high-performance concrete viaduct." *ACI Special Publication*,Vol. **167**, No.

Lienhard, John H. (2011). "A heat transfer textbook". *Mineola, N.Y.*, Dover Publications.

Lubarda, Vlado A and Chen, Michelle C,(2008). "On the elastic moduli and compliances of transversely isotropic and orthotropic materials." *Journal of Mechanics of Materials and Structures*,Vol. **3**, No. 1, pp. 153-171.

Makar, J. and Desnoyers, R.,(2001). "Magnetic field techniques for the inspection of steel under concrete cover." *NDT & e International*,Vol. **34**, No. 7, pp. 445-456.

Manning, D. G, and Holt, F.B. (1980). "Detecting delaminations in concrete bridge decks". *Concrete International***:** 34, 41.

Manning, D. G. and Masliwec, T.,(1990). "Application of radar and thermograpby to bridge deck condition surveys." *Bridge Management: Inspection, Maintenance, Assessment and Repair Papers Presented at the Second International Conference on Bridge Management, Held at the University of Surrey, Guildford, UK April 18-21, 1993*,Vol. No.

Mascaro, Margaret Grace and Moen, Cristopher D. (2012). "Out-of-plane web deformation and relative arch movement of hybrid-composite beams based on photogrammetry", Virginia Polytechnic Institute and State University.

Maser, K. R. and Roddis, W. M. K.,(1990). "Principles of thermography and radar for bridge deck assessment." *Journal of Transportation Engineering*,Vol. **116**, No. 5, pp. 583-601.

Mazumdar, Sanjay (2001). "Composites manufacturing: Materials, product, and process engineering", CrC press.

Merkle, Wesley John.(2004). "Load distribution and response of bridges retrofitted with various frp systems", University of Missouri--Rolla

Mindess, Sidney and Young, J Francis,(1981). "Concrete, prentice hall." *Englewood Cliffs, NJ*,Vol. No., pp. 481.

Mirmiran, A (2001). "Innovative combinations of frp and traditional materials". *FRP Composites in Civil Engineering. Proceedings of the International Conference on FRP Composites in Civil Engineering.*

Myers, John J, et al. (2008). "Preservation of missouri transportation infrastructures: Validation of frp composite technology through field testing–in-situ load testing of bridges p-962, t-530, x-495, x-596 and y-298".

Nair, Archana and Cai, C. S.,(2010). "Acoustic emission monitoring of bridges: Review and case studies." *Engineering Structures*,Vol. **32**, No. 6, pp. 1704-1714.

Nosdall, Stephen Van.(2013). "Experiments on a hybrid composite beam for bridge applications". Master of Science, faculty of the Virginia Polytechnic Institute and State University

Prine, D. W., Marron, D.R. (1997). "Acoustic emission and strain gage monitoring of prototype retrofit for caltrans structure b-22-26 r/l, i-80 sacramento river (bryte bend), sacremento, ca". Evanston, IL, Infrastructure Technology Institute, Northwestern University.

Radolli, M and Green, R,(1975). "Thermal stresses in concrete bridge superstructures under summer conditions." *Transportation Research Record*,Vol. No. 547.

Scheel, H., Hillemeier, B.,(2003). "Location of prestressing steel fractures in concrete." *Materials in Civil Engineering*,Vol. **15**, No. 3, pp. 7.

Scott, I. (1991). "Basic acoustic emission". *New York*, Gordon and Breach Science Publishers.

Silva, Manuel AG and Biscaia, Hugo,(2008). "Degradation of bond between frp and rc beams." *Composite structures*,Vol. **85**, No. 2, pp. 164-174.

Snape, Thomas and Lindyberg, Robert,(2009). "Test results: Hc beam for the knickerbocker bridge." *AEWC Report*,Vol. No., pp. 10-16.

Snape, Thomas and Lindyberg, Robert (2009). "Test results: Hc beam for the knickerbocker bridge", Advanced Structures & Composites Center conducts, University of Maine.

Thorenfeldt, El, et al. (1987). "Mechanical properties of high-strength concrete and application in design". *Proceedings of the Symposium "Utilization of High Strength Concrete*.

Todeschini, Claudio E, et al. (1964). "Behavior of concrete columns reinforced with high strength steels". *ACI Journal Proceedings*, ACI.

Van Erp, G, et al. (2002). "An australian approach to fibre composite bridges". *Proceedings of the International Composites Conference ACUN4, Composite Systems: Macro Composites, Micro Composites, Nano Composites, UNSW Sydney*.

Vannoy, D. W., Asmi, M., Liu, J. (1987). "Acoustic emission monitoring of the woodrow wilson bridge". Baltimore, MD, Maryland Department of Transportatoin**:** 113.

Waldron, Peter, et al. (2001). "Durability of frp in concrete: A state of the art". *Proceedings of the International Workshop on: Composites in Construction*.

Wang, A.S.D. (1986). "On fracture mechanics of matrix cracking in composite laminates". *Proc. Int. Symp. on Composite Materials and Structures*. Beijing**:** 576-584.

Washer, G., Allempalli, S. (2013). Nde methods for composite materials. International handbook of frp composites in civil engineering. M. Zoughi. New York, NY, Taylor and Francis. **1**.

Washer, Glenn A. (2009). "Application of infrared thermography (ir) for detecting defects in concrete", American Society for Nondestructive Testing.

Wight, James K and MacGregor, James Grierson (2012). "Reinforced concrete: Mechanics and design", Pearson Education Inc., Upper Saddle River, NJ.

Wright, WW,(1981). "The effect of diffusion of water into epoxy resins and their carbon-fibre reinforced composites." *Composites*,Vol. **12**, No. 3, pp. 201-205.

Yazdani, Nur, et al.,(2000). "Effect of bearing pads on precast prestressed concrete bridges." *Journal of Bridge Engineering*,Vol. **5**, No. 3, pp. 224-232.